Hokkaido University

Division of Mechanical and Space Engineering

Mean-Field Kinetic Theory Based Study of Boundary Condition at Vapor–Liquid Interface

Misaki Kon

February 3, 2017

Acknowledgements

This thesis is the summary that I have studied in the Laboratory of Fluid Dynamics in Hokkaido University since 2012. A lot of people have supported me. I would like to thank everybody.

I would first like to thank my supervisor Professor Masao Watanabe of Hokkaido University who gave me an opportunity to study in the fully equipped laboratory. His comments and suggestions have inspired me until now.

I would like to thank Associate Professor Kazumichi Kobayashi of Hokkaido University who always steers me in the right direction. I might not have completed this thesis without his passionate and permanent guidance.

I would also like to thank my thesis committee members for all of their guidance. I especially thank Professor Nobuyuki Oshima of Hokkaido University, Professor Takeru Yano of Osaka University, Professor Yuichi Murai of Hokkaido University, Professor Satoshi Tomioka of Hokkaido University, Associate Professor Shusaku Harada of Hokkaido University, and Associate Professor Yuji Tasaka of Hokkaido University who gave me valuable comments not only at the thesis defense but also at meetings and conferences.

I am deeply grateful to Assistant Professor Hiroyuki Fujii of Hokkaido University, Assistant Professor Masashi Inaba of Osaka University, and Dr. Yoshinori Jinbo who always gave me insightful comments.

I have had the support and encouragement from laboratory members. I especially thank research colleagues and coauthors Mr. Rintaro Yoshinaka, Mr. Kotaro Ohashi, Mr. Takato Yahagi, Mr. Kazumasa Hori, Mr. Kiyofumi Sasaki, and Mr. Takahiro Nagayama.

This study is partly supported by The Clark Memorial Foundation in Hokkaido University and the Grant-in-Aid for JSPS Research Fellow. I thank their financial support.

Finally, my deepest appreciation goes to my family. I cannot express how grateful I am.

February 3, 2017

今 美沙紀

Contents

Chapter

1

Introduction

The target of this thesis is heat and mass transfer in vapor–liquid two-phase systems composed of vapor and its condensed phase. Not only can this transport phenomena be widely observed in the natural world, but these are also applied to engineering. Hence, this transport phenomenon in the vapor–liquid two-phase system has been investigated from various theoretical frameworks, such as fluid dynamics, thermodynamics, and physical chemistry. In this thesis, we especially examine heat and mass transfer associated with a mass flux in the normal direction passing through the vapor–liquid interface. The mass flux at the vapor–liquid interface arises due to the molecular motions near the vapor–liquid interface. In general, the influence of the microscopic phenomenon is confined to a sufficiently small region, and it does not affect the macroscopic phenomenon. On the other hand, it is known that the mass flux in the normal direction passing through the vapor–interface affects the vapor flow beyond the region in the vicinity of the interface. Naturally, such a mass flux should be predicted based on the microscopic theory. However, simplified models that ignore the microscopic phenomenon near the vapor–liquid interface are widely used as the boundary condition in the macroscopic theory, namely, fluid dynamics. The objective of this thesis is to propose a proper boundary condition at the vapor–liquid interface from the microscopic theories, namely, the mean-field kinetic theory and molecular gas dynamics. To achieve this objective, we investigate the boundary condition in molecular gas dynamics by utilizing the molecular simulation based on the mean-field kinetic theory. This investigation is the main content of this thesis. With the use of this boundary condition obtained by the molecular simulation, we can derive the boundary condition in fluid dynamics by the molecular gas dynamics analysis.

1.1 Vapor–liquid two-phase flows

1.1.1 Importance of mass flux at vapor–liquid interface

In this section, we detail our target, which is heat and mass transfer in vapor–liquid two-phase systems composed of single-component vapor and its condensed phase. Fundamentally, liquid and vapor are composed of molecules and are essentially discrete. However, when the molecular collisions sufficiently take place in the domain under consideration, liquid and vapor can be assumed as the continuum mediums in which liquid and vapor are in local or global equilibrium. This assumption is the basis of continuum mechanics, namely, fluid dynamics. On the other hand, the presence of the interface between liquid and vapor often interrupts the application of continuum mechanics because the macroscopic variables change drastically. Thus, we have to impose the rule regarding the mass, momentum, and energy passing through the vapor–liquid interface.

A fundamental rule is the conservation law of fluxes. The conservation laws of the mass flux $\mathcal{M}$, the momentum flux $\mathcal{P}_i$, and the energy flux $\mathcal{E}$ are described as follows:

$$\mathcal{M} \equiv \rho_{\mathrm{L}}(v_{\mathrm{L}j} - v_{\mathrm{w}j})n_j = \rho_{\mathrm{V}}(v_{\mathrm{V}j} - v_{\mathrm{w}j})n_j, \tag{1.1}$$

$$\mathcal{P}_i \equiv [\rho_{\mathrm{L}} v_{\mathrm{L}i}(v_{\mathrm{L}j} - v_{\mathrm{w}j}) + p_{\mathrm{L}ij}]n_j = [\rho_{\mathrm{V}} v_{\mathrm{V}i}(v_{\mathrm{V}j} - v_{\mathrm{w}j}) + p_{\mathrm{V}ij}]n_j, \tag{1.2}$$

$$\begin{aligned}\mathcal{E} &\equiv [\rho_{\mathrm{L}}(e_{\mathrm{L}} + \frac{1}{2}v_{\mathrm{L}i}^2)(v_{\mathrm{L}j} - v_{\mathrm{w}j}) + p_{\mathrm{L}ij}v_{\mathrm{L}i} + q_{\mathrm{L}j}]n_j \\ &= [\rho_{\mathrm{V}}(e_{\mathrm{V}} + \frac{1}{2}v_{\mathrm{V}i}^2)(v_{\mathrm{V}j} - v_{\mathrm{w}j}) + p_{\mathrm{V}ij}v_{\mathrm{V}i} + q_{\mathrm{V}j}]n_j,\end{aligned} \tag{1.3}$$

where the subscripts L and V represent the variables in liquid and vapor, respectively, n_i is the unit vector in the direction normal to the vapor–liquid interface pointing toward vapor, ρ is the density, v_i is the flow velocity vector, $v_{\mathrm{w}i}$ is the velocity vector of the motion of the interface (advection and deformation), p_{ij} is the stress tensor, e is the internal energy, and q_i is the heat flux vector.

When $\mathcal{M} = 0$, given the condition as to whether $v_{\mathrm{L}i}$ and $v_{\mathrm{V}i}$ follow $v_{\mathrm{w}i}$ (the slip or non-slip boundary condition), we can readily obtain the expressions of the stress tensor and the heat flux vector in the direction normal to the vapor–liquid interface. In contrast, when $\mathcal{M} \neq 0$, we have to specify a certain $\mathcal{M}$ to obtain these expressions because the terms related to $\mathcal{M}$ are included in $\mathcal{P}_i$ and $\mathcal{E}$. Therefore, a proper specification of the mass flux at the vapor–liquid interface is necessary to predict heat and mass transfer in the vapor–liquid two-phase system.

In this thesis, we mainly discuss the case of $\mathcal{M} \neq 0$, especially the nonequilibrium case which cannot be handled as thermodynamic equilibrium. In such nonequilibrium cases, the state that the mass flux leaving from liquid to vapor ($(v_i - v_{\mathrm{w}i})n_i > 0$) is referred to as *net evaporation*, and the mass flux in the direction opposite to net evaporation ($(v_i - v_{\mathrm{w}i})n_i < 0$) is referred to as *net condensation*. It is known that the influence of net evaporation/condensation is dominant in some vapor–liquid two-phase flow problems, namely, dynamics of bubbles and droplets [1–6].

A typical example is the vapor bubble collapse problem. Fujikawa and Akamatsu [1] derived the equation of motion for single spherical bubble accompanied with net evaporation/condensation for the first time. The result of the numerical simulation of this equation of motion implied that a purely vaporous bubble produce a strong pressure wave in liquid at the instant the rebound process begins. This equation of motion is commonly used in the numerical simulation of a bubble accompanied with net evaporation/condensation. Akhatov *et al.* [2] proposed the numerical simulation of the single spherical bubble collapse and rebound processes accompanied with net evaporation/condensation by the Euler equation and showed that the temporal evolution of a bubble radius agrees with that obtained by the experiment for a laser induced bubble. Jinbo *et al.* [3] investigated the influence of net evaporation/condensation on the single nonspherical bubble collapse processes by the Euler equation and indicated that the temperature and pressure fields in a bubble vary locally according to net evaporation/condensation. These results im-

plied that net evaporation/condensation affects the temperature and pressure fields in the inside and the outside of a bubble. Furthermore, on the basis of these results, we can naturally predict that net evaporation/condensation affects the shock wave propagation and the liquid jet formulation attributed to the bubble collapse process.

In these studies, well-known boundary conditions at the vapor–liquid interface, namely, the Hertz-Knudsen-Langmuir model and the Hertz-Knudsen-Schrage model, are utilized to estimate the mass flux induced by net evaporation/condensation. Some studies, however, threw doubt on the accuracy of these models [7]. We detail these models in the next section.

Moreover, from an application point of view, several studies [8, 9] proposed the basis of therapeutic applications by using the shock wave and the liquid jet attributed to the bubble collapse process. For example, Ohl *et al.* [9] tried to apply the liquid jet to deliver noninvasively large-sized molecules into cells, and Kobayashi *et al.* [8] estimated the interaction between the shock wave and the bubble for the extracorporeal shock-wave lithotripsy. However, in these therapeutic applications, we have to take into account the influence of net evaporation/condensation in addition to the effect of the complex bubble interaction and the noncondensable gas. At least, if we can treat the influence of net evaporation/condensation with the accurate model, it will be helpful for developing the basis of these therapeutic applications.

1.1.2 Boundary condition at vapor–liquid interface

As was mentioned above, a proper specification of the mass flux at the vapor–liquid interface is necessary to predict heat and mass transfer in the vapor–liquid two-phase system. The well-known boundary conditions to estimate the mass flux induced by net evaporation/condensation are the Hertz-Knudsen-Langmuir (HKL) model and the Hertz-Knudsen-Schrage (HKS) model [10]. The previous studies introduced in the above section [1–3] utilized the HKL and HLS models. Even in studies other than those introduced, these models are very commonly used. The recent researches

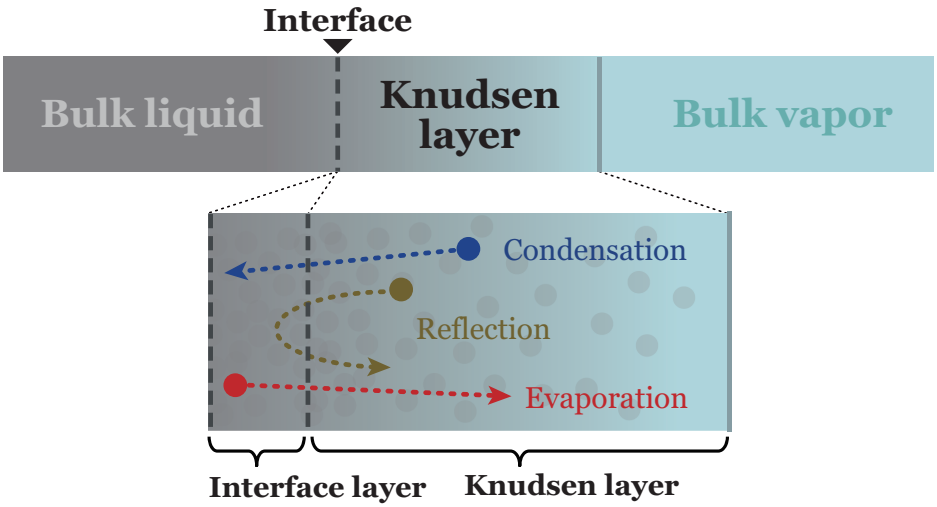

Figure 1.1: Physical picture of the vapor–liquid two-phase system.

regarding these models are reviewed by Persad *et al.* [11]. However, the accuracy of these models are questionable [7].

Here, we state the critical issue of the HKL and HKS models and the objective of this thesis. The mass flux at the vapor–liquid interface obtained by the HKL and HLS models are as follows:

$$\mathcal{M}_{\mathrm{HKL}} = \frac{\alpha}{\sqrt{2\pi R}} \left(\frac{p^*}{\sqrt{T_{\mathrm{L}}}} - \frac{p}{\sqrt{T}} \right), \tag{1.4}$$

$$\mathcal{M}_{\mathrm{HKS}} = \frac{2\alpha}{(2-\alpha)\sqrt{2\pi R}} \left(\frac{p^*}{\sqrt{T_{\mathrm{L}}}} - \frac{p}{\sqrt{T}} \right), \tag{1.5}$$

where α is an unknown dimensionless parameter, R is the gas constant, T_{L} is the liquid temperature, p^* is the saturated vapor pressure at the liquid temperature, p and T are the pressure and the temperature, respectively. The critical issue of Eqs. (1.4) and (1.5) lies in the determination of p and T.

To detail the critical issue of the HKL and HKS models, we explain the physical picture of the vapor–liquid two-phase system as shown in Fig. 1.1. As illustrated in Fig. 1.1, there is a transition layer between bulk liquid and bulk vapor. This transition layer in which the characteristic length scale is the mean free path is called the *Knudsen layer* [12]. The lower part of Fig. 1.1 is the enlarged view of the

vapor–liquid interface and the Knudsen layer. In the macroscopic point of view, the vapor–liquid interface is the discontinuity surface, while in the microscopic point of view, the macroscopic variables transit smoothly between bulk liquid and bulk vapor. As illustrated in Fig. 1.1, the region in contact with the vapor–liquid interface in which the characteristic length scale is the molecular diameter is referred to as the *interface layer* in this thesis. The interface layer is equivalent to the vapor–liquid interface with zero thickness in the macroscopic point of view. With this microscopic point of view, we can capture the essence that net evaporation/condensation occurs as a consequence of the unbalance (nonequilibrium) of the number of molecules in the interface layer. Such nonequilibrium of molecules accommodates to local equilibrium through the molecular interactions in the Knudsen layer. We postulate, throughout this thesis, the physical picture of the vapor–liquid two-phase system shown in Fig. 1.1.

Let us now go back to the HKL and HKS models (Eqs. (1.4) and (1.5)). The critical issue of the HKL and HKS models is that these models ignore the molecular interactions in the Knudsen layer. In other words, p and T in these models can be specified independently of the molecular interactions in the Knudsen layer. Since the outside of the Knudsen layer reaches local equilibrium as a consequence of the molecular interactions in the Knudsen layer, there is no basis that a proper mass flux can be predicted from the HKL and HKS models by specifying p and T that ignore such molecular interactions. It would be advantageous that the HKL and HKS models can omit the complex analysis in the Knudsen layer, but the molecular interactions there play a major role in the mass flux induced by net evaporation/condensation. The aim of this thesis is to propose a physically proper boundary condition at the vapor–liquid interface that takes into account such microscopic phenomenon.

We then describe the strategy of this thesis. In this thesis, we postulate a phenomenological model of the molecular motions to discuss the microscopic phenomenon near the vapor–liquid interface. The key processes according to this model

are *evaporation*, *reflection*, and *condensation*. As illustrated in Fig. 1.1, the process from the interface layer into the Knudsen layer is called evaporation, that from the Knudsen layer into the interface layer is called condensation, and that accompanied by the change in the direction in the interface layer is referred to as reflection. When the number of the evaporation molecules is greater than that of the condensation molecules, net evaporation occurs at the vapor–liquid interface, while when the number of condensation molecules is greater than that of the evaporation molecules, net condensation occurs at the vapor–liquid interface.

To examine these molecular processes, we have to carry out the molecular simulation for the vapor–liquid two-phase system including the interface layer and the Knudsen layer. We refer to the simulation that tracks the temporal evolution of the positions and the velocities of molecules under a certain intermolecular potential as the molecular simulation. With the development of high-performance computing from the 1990s, the molecular simulations for the vapor–liquid two-phase system have been performed to examine the molecular processes, such as evaporation, reflection, and condensation [13–20]. However, the results of the molecular simulation cannot be directly applied as the boundary condition in the macroscopic theory, namely, fluid dynamics.

The most accurate way to derive the boundary condition in fluid dynamics by replacing the microscopic information obtained from the molecular simulation with relevant macroscopic variables is the molecular gas dynamics analysis [12]. In a sense, molecular gas dynamics bridges between the microscopic theory and the macroscopic theory. In the molecular gas dynamics analysis, the microscopic phenomenon in the interface layer is taken into the boundary condition (the kinetic boundary condition). However, the conventional kinetic boundary condition that has been used in the molecular gas dynamics analysis is mere mathematical model. The main content of this thesis is to investigate the kinetic boundary condition at the vapor–liquid interface by utilizing the molecular simulation in the vapor–liquid two-phase system

including the interface layer and the Knudsen layer.

1.2 Molecular gas dynamics

Here, we briefly explain the theoretical framework of molecular gas dynamics, the conventional kinetic boundary condition, and the derivation method of the boundary condition in fluid dynamics. The contents of this section are based on the literature [7, 12].

1.2.1 Velocity distribution function

In the following, we consider gas or vapor consisting of single-component monatomic molecules with the influence range of the intermolecular force a. The motion of these molecules is governed by Newton's equation of motion. A sufficient number of molecules are present in the system under consideration; there is also many molecules in the volume elements taken in the system in which the number density is n. In the limit when $n \to \infty$ and $a \to 0$, we assume that $na^3 \to 0$ holds. This condition means that the total volume where the intermolecular forces are effective is negligibly small compared with the volume of gas or vapor, that is, the ideal gas condition. Also, the limiting that $n \to \infty$ and $a \to 0$ with fixed na^2 is called the Grad-Boltzmann limit. The inverse of na^2 is the order of the mean free path, which is the distance of molecules traveling before the subsequent collision.

Under the limiting that $m \to 0$ and $n \to \infty$ with keeping mn is fixed at a finite value, we can define the velocity distribution function f, which is a function representing the statistical properties of molecules in the volume element, as follows:

$$m\mathrm{d}N = f(\boldsymbol{x}, \boldsymbol{\xi}, t)\mathrm{d}\boldsymbol{x}\mathrm{d}\boldsymbol{\xi}, \tag{1.6}$$

where $\mathrm{d}\boldsymbol{x}$ is the volume element in the physical space ($\mathrm{d}\boldsymbol{x} = \mathrm{d}x\mathrm{d}y\mathrm{d}z$), $\mathrm{d}\boldsymbol{\xi}$ is the volume element in the molecular velocity space ($\mathrm{d}\boldsymbol{\xi} = \mathrm{d}\xi_x\mathrm{d}\xi_y\mathrm{d}\xi_z$), and m is the mass

of a molecule. In Eq. (1.6), $\mathrm{d}N$ is the number of molecules in $\mathrm{d}\boldsymbol{x}\mathrm{d}\boldsymbol{\xi}$ at time t, the position $x_i = (x, y, z)$, and molecular velocity $\xi_i = (\xi_x, \xi_y, \xi_z)$ in the 6-dimensional phase space. This f defined in Eq. (1.6) is the only unknown variable in molecular gas dynamics. Note that we use vector notation and tensor notation without notice, such as $x_i = \boldsymbol{x}$ and $\xi_i = \boldsymbol{\xi}$, if necessary.

Once the velocity distribution function f is obtained, the macroscopic variables at position x_i and time t are defined by the moments of f:

- Density ρ

$$\rho = \int f(\boldsymbol{x}, \boldsymbol{\xi}, t)\mathrm{d}\boldsymbol{\xi}. \tag{1.7}$$

- Velocity v_i

$$v_i = \frac{1}{\rho}\int \xi_i f(\boldsymbol{x}, \boldsymbol{\xi}, t)\mathrm{d}\boldsymbol{\xi}. \tag{1.8}$$

- Temperature T

$$T = \frac{1}{3R\rho}\int (\xi_i - v_i)^2 f(\boldsymbol{x}, \boldsymbol{\xi}, t)\mathrm{d}\boldsymbol{\xi}. \tag{1.9}$$

- Pressure p

$$p = \frac{1}{3}\int (\xi_i - v_i)^2 f(\boldsymbol{x}, \boldsymbol{\xi}, t)\mathrm{d}\boldsymbol{\xi} = R\rho T. \tag{1.10}$$

- Specific internal energy e

$$e = \frac{1}{\rho}\int \frac{1}{2}(\xi_i - v_i)^2 f(\boldsymbol{x}, \boldsymbol{\xi}, t)\mathrm{d}\boldsymbol{\xi} = \frac{3}{2}RT. \tag{1.11}$$

- Stress tensor p_{ij}

$$p_{ij} = \int (\xi_i - v_i)(\xi_j - v_j) f(\boldsymbol{x}, \boldsymbol{\xi}, t) \mathrm{d}\boldsymbol{\xi}. \tag{1.12}$$

- Heat flux vector q_i

$$q_i = \int \frac{1}{2}(\xi_i - v_i)(\xi_j - v_j)^2 f(\boldsymbol{x}, \boldsymbol{\xi}, t) \mathrm{d}\boldsymbol{\xi}. \tag{1.13}$$

Similarly, the mass, momentum, and energy fluxes passing through an arbitrary surface are obtained from f:

- Mass flux $\mathcal{M}$

$$\begin{aligned} \mathcal{M} &= \int (\xi_j - v_{\mathrm{w}j}) n_j f(\boldsymbol{x}, \boldsymbol{\xi}, t) \mathrm{d}\boldsymbol{\xi} \\ &= n_j \rho (v_j - v_{\mathrm{w}j}). \end{aligned} \tag{1.14}$$

- Momentum flux vector $\mathcal{P}_i$

$$\begin{aligned} \mathcal{P}_i &= \int \xi_i (\xi_j - v_{\mathrm{w}j}) n_j f(\boldsymbol{x}, \boldsymbol{\xi}, t) \mathrm{d}\boldsymbol{\xi} \\ &= n_j [p_{ij} + \rho v_i (v_j - v_{\mathrm{w}j})]. \end{aligned} \tag{1.15}$$

- Energy flux $\mathcal{E}$

$$\begin{aligned} \mathcal{E} &= \int \frac{1}{2}\xi_i^2 (\xi_j - v_{\mathrm{w}j}) n_j f(\boldsymbol{x}, \boldsymbol{\xi}, t) \mathrm{d}\boldsymbol{\xi} \\ &= n_j [q_j + p_{ij} v_i + \rho (e + \frac{1}{2} v_i^2)(v_j - v_{\mathrm{w}j})]. \end{aligned} \tag{1.16}$$

In Eqs. (1.7)–(1.16), the three-dimensional integration with respect to ξ_i is carried out over the whole space of ξ_i. In the framework of molecular gas dynamics, we can examine f itself and all variables defined by f, such as Eqs. (1.7)–(1.16), regardless

of equilibrium or nonequilibrium. For this reason, fluid dynamics is sometimes expressed as to be the part of molecular gas dynamics.

1.2.2 Boltzmann equation

As mentioned above, we deal with numerous molecules whose motion is governed by Newton's equation of motion. Here, we regard the gas or vapor as an ensemble of particles and examine the motion of this ensemble, which is governed by the Liouville equation. Although the Liouville equation is exact, it is often too detailed to describe the motion of gas or vapor, and it is too complex to be solved. A more convenient starting point to describe the N-particle system is the Bogolyubov-Born-Green-Kirkwood-Yvon (BBGKY) hierarchy equation. The BBGKY hierarchy equation connects the evolution of an N-particle distribution function to an $N+1$ particle distribution function; this equation is not closed generally because both distribution functions are unknown.

In fact, to obtain the macroscopic variables and the fluxes that we are interested in, we only require the lowest order distribution function defined in Eq. (1.6). However, the two-particle distribution function is required to solve the BBGKY hierarchy equation for the one-particle distribution function, and this equation is not closed after all. We introduce the following correlation function to close the BBGKY hierarchy equation.

$$f_2(\boldsymbol{x}_1, \boldsymbol{x}_2, \boldsymbol{\xi}_1, \boldsymbol{\xi}_2, t) = Y f_1(\boldsymbol{x}_1, \boldsymbol{\xi}_1, t) f_1(\boldsymbol{x}_2, \boldsymbol{\xi}_2, t), \tag{1.17}$$

where f_1 indicates the one-particle distribution function, which is equivalent to f defined in Eq. (1.6), f_2 indicates the two-particle distribution function, $\boldsymbol{x}_1$ and $\boldsymbol{x}_2$ indicate the positions of two molecules, $\boldsymbol{\xi}_1$ and $\boldsymbol{\xi}_2$ indicate the velocities of two molecules, and Y is a pair correlation. In the Grad-Boltzmann limit, Y can be set to unity, which is called the molecular chaos assumption, and thereby f_2 is

transferred to the product of f_1. Also, the intermolecular collisions are events that occur at one point in time and space. Since the collision frequency of the triple or more multiple collisions is sufficiently small in the Grad-Boltzmann limit, we can only consider the binary event.

By the above procedure, the Boltzmann equation which is an equation governing the evolution of the one-particle distribution function in the system without the external force is derived as follows [21]:

$$\frac{\partial f}{\partial t} + \xi_i \frac{\partial f}{\partial x_i} = C_{\mathrm{B}}, \tag{1.18}$$

where the left-hand side of Eq. (1.18) represents the effect of the evolution of f along the path of free molecular motion, and the right-hand side of Eq. (1.18) represents the effect of the intermolecular collision and is called *collision integral* or *Boltzmann collision term*,

$$C_{\mathrm{B}} = \frac{1}{m} \int_{\text{all } K_i,\ \text{all } \xi_{1i}} [f(\boldsymbol{x}, \boldsymbol{\xi}_1', t) f(\boldsymbol{x}, \boldsymbol{\xi}', t) - f(\boldsymbol{x}, \boldsymbol{\xi}_1, t) f(\boldsymbol{x}, \boldsymbol{\xi}, t)] B \mathrm{d}\Omega(\boldsymbol{K}) \mathrm{d}\boldsymbol{\xi}_1, \tag{1.19}$$

where ξ_i indicates the velocity of a molecule under consideration, ξ_{1i} indicates the velocity of a molecule colliding with the molecule having the velocity ξ_i, K_i is a unit vector along the direction of the molecular velocity before and after the collision, $\mathrm{d}\Omega(\boldsymbol{K})$ is a solid angle element in the K_i direction, and B is a nonnegative function determined by the intermolecular force model and $B = a^2 |K_j(\xi_{1j} - \xi_j)|/2$ for hard-sphere molecules having a diameter a. In Eq. (1.19), ξ_i' and ξ_{1i}' indicate the molecular velocities after the collision and are determined by considering the elastic collision,

$$\xi_i' = \xi_i + K_i K_j (\xi_{1j} - \xi_j), \qquad \xi_{1i}' = \xi_{1i} + K_i K_j (\xi_{1j} - \xi_j). \tag{1.20}$$

The details of the derivation of Eqs. (1.18) and (1.19) are given in the literature

[12, 21].

H-theorem

We hereafter give further explanations on the Boltzmann equation. Although these are very important to analyzing the Boltzmann equation, since it is not the main topic of this thesis, we do not give the derivation or proof here. The H-theorem explains the irreversibility of entropy, that is, the second law of thermodynamics, in a molecular theory. This theorem prescribes the relation of the H function,

$$H = \int_{\text{all } \xi_i} f \ln(f/c) \mathrm{d}\boldsymbol{\xi}, \tag{1.21}$$

or a function, $\mathcal{H}$, obtained by integrating the H function with respect to the domain $\mathcal{D}$,

$$\mathcal{H} = \int_{\mathcal{D}} H \mathrm{d}\boldsymbol{x}. \tag{1.22}$$

where c is an appropriate constant with the same dimension as f. According to the following inequality, H or $\mathcal{H}$ never increases.

$$\frac{\mathrm{d}\mathcal{H}}{\mathrm{d}t} - \int_{\partial\mathcal{D}} H_i n_i \mathrm{d}S = \int_{\mathcal{D}} \left(\int_{\text{all } \xi_i} [1 + \ln(f/c)] C_{\mathrm{B}} \mathrm{d}\boldsymbol{\xi} \right) \mathrm{d}\boldsymbol{x} \leq 0, \tag{1.23}$$

$$\text{when } H_i n_i = 0 \text{ on } \partial\mathcal{D},$$

where

$$H_j = \int_{\text{all } \xi_i} \xi_j f \ln(f/c) \mathrm{d}\boldsymbol{\xi}. \tag{1.24}$$

In this inequality, the equal sign is valid only when f is an equilibrium solution of the Boltzmann equation. The equilibrium solution of the Boltzmann equation is shown in the next section. This inequality represents that if there is no transport

of H_i through the boundary $\partial\mathcal{D}$ and the system is isolated from the outside, the macroscopic quantity $\mathcal{H}$ never increases, that is, the irreversibility of the temporal evolution of the Boltzmann equation. From this reason, the models of the Boltzmann equation should also hold the H-theorem.

Equilibrium solution of Boltzmann equation

The steady and spatially uniform solution of the Boltzmann equation is called the equilibrium solution, which is the velocity distribution function of the system in thermodynamic equilibrium and is expressed as

$$f^* = \frac{\rho}{\sqrt{2\pi RT}^3} \exp\left(-\frac{(\xi_i - v_i)^2}{2RT}\right), \tag{1.25}$$

where ρ is the density, T is the temperature, v_i is the flow velocity vector, and R is the gas constant. Equation (1.25) is called the Maxwellian distribution. The steady and spatially uniform f holds $C_\mathrm{B} = 0$. Also, when ρ, v, and T are replaced with the function of t and x_i, Eq. (1.25) is called the local equilibrium distribution or the local Maxwellian distribution. Although the local equilibrium distribution holds $C_\mathrm{B} = 0$, this distribution is not always the solution of the Boltzmann equation. Grad [22] clarified the general form of the local equilibrium distribution to be the solution of the Boltzmann equation.

Mean free path

The *mean free path*, ℓ, which is the distance of molecules traveling before the subsequent collision, is the characteristic length for the Boltzmann equation and defined as

$$\ell = \frac{\bar{\xi}}{\bar{\mu}}, \tag{1.26}$$

where $\bar{\xi}$ is the average molecular speed,

$$\bar{\xi} = \sqrt{\frac{8RT}{\pi}}, \tag{1.27}$$

and $\bar{\mu}$ is the mean collision frequency,

$$\bar{\mu} = \frac{1}{\rho m} \int_{\text{all } K_i,\ \text{all } \xi_i \text{ and } \xi_{1i}} f(\boldsymbol{\xi}) f(\boldsymbol{\xi}_1) B \mathrm{d}\Omega(\boldsymbol{K}) \mathrm{d}\boldsymbol{\xi} \mathrm{d}\boldsymbol{\xi}_1. \tag{1.28}$$

When f is the Maxwellian distribution with constant ρ, T, and v_i (Eq. (1.25)), $\bar{\mu}$ becomes

$$\bar{\mu} = 4na^2\sqrt{\pi RT}, \tag{1.29}$$

where n is the number density. Note that the inverse of the mean collision frequency $\bar{\mu}^{-1}$ is called the mean free time. The substitution of Eqs. (1.27) and (1.29) into Eq. (1.26) leads to

$$\ell = \frac{1}{\sqrt{2}\pi n a^2}. \tag{1.30}$$

1.2.3 Kinetic boundary condition

The Boltzmann equation regulates the evolution of the velocity distribution function along the path in ($\boldsymbol{x}$, t) space of the molecules having the velocity ξ_i. If f in the domain under consideration at the initial time is given and how the molecules are scattered at the boundary at the arbitrary time is determined, we can determine the behavior of f by the Boltzmann equation. In other words, the boundary condition for the Boltzmann equation is an outgoing velocity distribution function to gas or vapor, f_{out}, as a consequence of molecules colliding and scattering at the boundary. The boundary condition for the Boltzmann equation is called the kinetic boundary condition (KBC). Similar to other boundary conditions, we cannot derive the KBC

from the framework of molecular gas dynamics. Although we have to investigate the molecular interaction with the boundary in order to impose the KBC, in the molecular gas dynamics analysis, mathematical models have often been utilized as the KBC [12, 23–25].

We hereafter consider the KBC in the system composed of monatomic vapor and its condensed phase (liquid) with the planar vapor–liquid interface. The conventional KBC, which is widely used in the molecular gas dynamics analysis [12, 23–25], is shown as follows:

$$f_{\mathrm{out}} = [\alpha\rho^* + (1-\alpha)\sigma]\hat{f}^*, \qquad (\xi_i - v_{\mathrm{w}i})n_i > 0, \tag{1.31}$$

where n_i is the unit vector in the direction normal to the vapor–liquid interface pointing vapor, ρ^* is the saturated vapor density at the liquid temperature T_{L}, $\hat{f}^*$ is the normalized velocity distribution function of the KBC and is assumed the normalized Maxwellian distribution at T_{L},

$$\hat{f}^* = \frac{1}{\sqrt{2\pi R T_{\mathrm{L}}}^3} \exp\left(-\frac{(\xi_i - v_{\mathrm{w}i})^2}{2RT_{\mathrm{L}}}\right), \tag{1.32}$$

σ is a parameter having the dimension of the density, and its definition is related to the velocity distribution function of molecules colliding with the vapor–liquid interface from vapor, f_{coll},

$$\sigma\sqrt{\frac{RT_{\mathrm{L}}}{2\pi}} = -\int_{(\xi_i - v_{\mathrm{w}i})n_i<0} (\xi_j - v_{\mathrm{w}j})n_j f_{\mathrm{coll}} \mathrm{d}\boldsymbol{\xi}, \tag{1.33}$$

where $\int_{(\xi_i - v_{\mathrm{w}i})n_i<0} \mathrm{d}\boldsymbol{\xi}$ indicates that the domain of the integration is $-\infty$ to zero for the molecular velocity in the direction normal to the vapor–liquid interface and $-\infty$ to ∞ for that in the tangential direction. Equation (1.31) is a mere mathematical model; α is a parameter and is often set to unity for simplicity, and the functional form of $\hat{f}^*$ is an assumption.

The conditions that Eq. (1.31) should satisfy as the KBC are shown below. The KBC is expressed by a scattering kernel, K_{I}, as

$$f_{\mathrm{out}}(\boldsymbol{x},\boldsymbol{\xi},t) = g_{\mathrm{I}}(\boldsymbol{x},\boldsymbol{\xi},t) + \int_{(\tilde{\xi}_i - v_{\mathrm{w}i})n_i<0} K_{\mathrm{I}}(\boldsymbol{\xi},\tilde{\boldsymbol{\xi}},\boldsymbol{x},t) f_{\mathrm{coll}}(\boldsymbol{x},\tilde{\boldsymbol{\xi}},t)\mathrm{d}\tilde{\boldsymbol{\xi}}, \quad (\xi_i - v_{\mathrm{w}i})n_i > 0, \tag{1.34}$$

where g_{I} is a term to be independent of f_{coll}, $\tilde{\boldsymbol{\xi}}$ indicates the molecular velocity colliding with the boundary. The scattering kernel K_{I} represents how the molecules that collide with the vapor–liquid interface are scattered. We restrict K_{I} to the linear scattering kernel independent of f_{coll}, which satisfy the following conditions:

1. g_{I} should be the non-negative function for $(\xi_i - v_{\mathrm{w}i})n_i > 0$.
2. K_{I} should be the non-negative function for $(\xi_i - v_{\mathrm{w}i})n_i > 0$ and $(\tilde{\xi}_i - v_{\mathrm{w}i})n_i < 0$.
3. K_{I} should satisfy the following relation in vapor–liquid equilibrium:

$$f^*(\boldsymbol{\xi}) = g_{\mathrm{I}}(\boldsymbol{\xi}) + \int_{(\tilde{\xi}_i - v_{\mathrm{w}i})n_i<0} K_{\mathrm{I}}(\boldsymbol{\xi},\tilde{\boldsymbol{\xi}},\boldsymbol{x},t) f^*(\tilde{\boldsymbol{\xi}})\mathrm{d}\tilde{\boldsymbol{\xi}}, \tag{1.35}$$

where

$$f^* = \frac{\rho^*}{(\sqrt{2\pi R T_{\mathrm{L}}})^3} \exp\left(-\frac{(\xi_i - v_{\mathrm{w}i})^2}{2RT_{\mathrm{L}}}\right), \tag{1.36}$$

that is, the equilibrium solution in the vapor–liquid two-phase system. This condition indicates that if the molecules colliding with the vapor–liquid interface have the equilibrium velocity distribution function (Eq. (1.36)), the molecules reflecting at the vapor–liquid interface should also have the same velocity distribution function.

1.2.4 Knudsen layer analysis

Sone *et al.* [12, 23] have systematically investigated the method for deriving the boundary condition in fluid dynamics, which is consistent with the fluid dynamic equations. As stated in the former section, the HKL and HKS models (Eqs. (1.4) and (1.5)) have the problem in determining p and T included in these models. In the method proposed by Sone *et al.* [12, 23], p and T, which take into account the molecular interactions in the Knudsen layer, can be obtained by solving the Boltzmann equation with the KBC. We here introduce the result by utilizing the conventional KBC (Eq. (1.31)).

The procedure to derive the boundary condition for the fluid dynamic equations by solving the Boltzmann equation in the Knudsen layer is called the Knudsen layer analysis [12, 23]. It becomes possible to replace the microscopic information in the Knudsen layer with the relevant macroscopic variables by this analysis. The Knudsen layer analysis is a boundary value problem to obtain the solution of the Boltzmann equation and its existence condition under the KBCs at the vapor–liquid interface and at the end of the Knudsen layer (infinitely far from the vapor–liquid interface). The existence condition of the solution of this boundary value problem means the states of the pressure p, the temperature T, and the velocity v_i at the end of the Knudsen layer,

$$\frac{p - p^*}{p^*} = \left(C_4^* - 2\sqrt{\pi} \frac{1-\alpha}{\alpha} \right) \frac{(v_i - v_{\mathrm{w}i}) n_i}{\sqrt{2RT_{\mathrm{L}}}}, \tag{1.37}$$

$$\frac{T - T_{\mathrm{L}}}{T_{\mathrm{L}}} = d_4^* \frac{(v_i - v_{\mathrm{w}i}) n_i}{\sqrt{2RT_{\mathrm{L}}}}, \tag{1.38}$$

that is, the slip boundary condition [12,23]. In Eqs. (1.37) and (1.38), C_4^* and d_4^* are the slip coefficients, which include the microscopic information in the Knudsen layer and these are obtained by determining the molecular model. The slip coefficients of various molecular models are summarized in the literature [12].

From Eq. (1.37) and the equation of state for the ideal gas, the mass flux at the

end of the Knudsen layer can be found as follows:

$$\mathcal{M}_{\mathrm{MGD}} = \frac{1}{2\sqrt{\pi}\frac{1-\alpha}{\alpha} - C_4^*}\sqrt{\frac{2}{R}}\left(\frac{p^*}{\sqrt{T_{\mathrm{L}}}} - \frac{p}{\sqrt{T_{\mathrm{L}}}}\right), \tag{1.39}$$

where the term $O[((v_i - v_{\mathrm{w}i})n_i/\sqrt{2RT_{\mathrm{L}}})^2]$ is neglected because the slip boundary condition is derived under the condition $|(v_i - v_{\mathrm{w}i})n_i/\sqrt{2RT_{\mathrm{L}}}| \ll 1$. With the use of Eqs. (1.39) and (1.38) or Eqs. (1.37) and (1.38) as the boundary conditions, the fluid dynamic equations can be closed. Equations (1.37), (1.38), and (1.39) are, strictly speaking, the boundary conditions at the end of the Knudsen layer, but we call those the *boundary conditions at the vapor–liquid interface* because we do not have to solve the Knudsen layer in the fluid dynamics analysis.

1.3 Summary

The objective of this thesis is to propose a physically proper boundary condition at the vapor–liquid interface with net evaporation/condensation. After summarizing the topics so far, we then clarify the remaining issue and state the scope of this thesis.

1.3.1 Clarification of remaining issue

To summarize the preceding sections, what we have to do to propose the boundary condition at the vapor–liquid interface are (i) to conduct the molecular simulation to construct the KBC and (ii) to conduct the Knudsen layer analysis to derive the boundary condition for the fluid dynamic equations. As for (ii), it has been systematically investigated by Sone *et al.* [12, 23]; hence, as long as these results are available, the only thing we should study in this thesis is (i).

According to the physical picture shown in Fig. 1.1, the KBC is the outgoing velocity distribution function from the interface layer at the vapor–liquid interface. Numerous studies [26–39] examined this velocity distribution function by the molec-

ular simulation in the vapor–liquid two-phase system including the interface layer and the Knudsen layer.

In some previous studies, α is divided into two different coefficients, namely, the evaporation coefficient α_{e} and the condensation coefficient α_{c}, as a kind of physical properties. These coefficients are defined in relation to the molecular processes illustrated in Fig. 1.1. Some different definitions have been proposed for α_{e} and α_{c}. For instance, Tsuruta *et al.* [31] defined α_{e} and α_{c} by the number of molecules at the vapor–liquid interface and expressed these coefficients as the functions of the liquid temperature and the translational energy in the direction normal to the vapor–liquid interface. Ishiyama *et al.* [33, 34] defined α_{e} and α_{c} by the molecular mass fluxes at the vapor–liquid interface and indicated that these coefficients depend only on the liquid temperature. Naturally, such a different tendency arises from the different definitions of α_{e} and α_{c}. However, it should be emphasized that even if these coefficients are calculated according to the same definitions as Ishiyama *et al.* [33, 34], these coefficients vary with the degree of net evaporation/condensation [27, 37]. These results indicate that neither α_{e} nor α_{c} has been indisputably determined after all.

In addition, some previous studies [34, 38, 40, 41] pointed out that the normalized velocity distribution function of the KBC deviates from the normalized Maxwellian distribution (Eq. (1.32)) when the vapor–liquid interface is in strong net evaporation or condensation. Thus, the construction of the KBC at the vapor–liquid interface is an issue open to question.

To clarify this remaining issue, we consider the following generalized KBC [42].

$$f_{\mathrm{out}} = \mathcal{A}\hat{f}^*, \qquad (\xi_i - v_{\mathrm{w}i})n_i > 0, \tag{1.40}$$

where we assume that $\hat{f}^*$ is to be the normalized Maxwellian distribution (Eq. (1.32)). The conditions of $\mathcal{A}$ is shown as follows: (1) $\mathcal{A}$ is the nonnegative function, (2) $\mathcal{A}$ is allowable to be the function of the liquid temperature T_{L} and/or σ (Eq. (1.33)),

and (3) $\mathcal{A}$ is independent of the molecular velocity. Note that some KBCs proposed by the previous molecular simulations do not satisfy these conditions. We extract the part related to the liquid temperature $\mathcal{A}_0(T_\mathrm{L})$ from $\mathcal{A}$ and rewrite Eq. (1.40) as

$$\mathcal{A} = \mathcal{A}_0(T_\mathrm{L}) + [\mathcal{A} - \mathcal{A}_0(T_\mathrm{L})]. \tag{1.41}$$

When $\mathcal{A} = \alpha_\mathrm{e}\rho^* + (1-\alpha_\mathrm{c})\sigma$, α_e and α_c are defined by

$$\alpha_\mathrm{e} = \frac{\mathcal{A}_0(T_\mathrm{L})}{\rho^*}, \qquad \alpha_\mathrm{c} = 1 - \frac{\mathcal{A} - \mathcal{A}_0(T_\mathrm{L})}{\sigma}. \tag{1.42}$$

In Eq. (1.42), the selection of $\mathcal{A}_0(T_\mathrm{L})$ is arbitrary. In other words, under the assumption that $\hat{f}^*$ is to be the normalized Maxwellian distribution (Eq. (1.32)), there is an infinite number of α_e and α_c pairs corresponding to arbitrary $\mathcal{A}_0(T_\mathrm{L})$. To determine α_e and α_c uniquely, we have to clarify the physical requirement that $\mathcal{A}_0(T_\mathrm{L})$ should satisfy. Also, if α_e and α_c is related to the molecular processes illustrated in Fig. 1.1, the physical requirement that $\mathcal{A}_0(T_\mathrm{L})$ should satisfy is synonymous with the definitions of these molecular processes. That is why α_e and α_c have not been determined so far.

1.3.2 Scope of this thesis

To break through the issue stated in above, we consider α_e and α_c from a more fundamental rule, that is, the conservation law of the mass flux extended to the microscopic point of view. This fundamental rule holds regardless of any condition. The conservation law of the mass flux extended to the microscopic point of view represents the relation between the mass flux in the macroscopic and microscopic

points of view as shown in the following.

$$\begin{aligned}\mathcal{M} &= \rho(v_j - v_{\mathrm{w}j})n_j \\ &= \int_{\text{all } \xi_i} (\xi_j - v_{\mathrm{w}j})n_j f(\boldsymbol{x}, \boldsymbol{\xi}, t)\mathrm{d}\boldsymbol{\xi} \\ &= \int_{(\xi_i - v_{\mathrm{w}i})n_i > 0} (\xi_j - v_{\mathrm{w}j})n_j f_{\mathrm{out}}\mathrm{d}\boldsymbol{\xi} + \int_{(\xi_i - v_{\mathrm{w}i})n_i < 0} (\xi_j - v_{\mathrm{w}j})n_j f_{\mathrm{coll}}\mathrm{d}\boldsymbol{\xi}, \end{aligned} \tag{1.43}$$

where $\int_{(\xi_i - v_{\mathrm{w}i})n_i > 0} \mathrm{d}\boldsymbol{\xi}$ indicates that the domain of the integration is zero to ∞ for the molecular velocity in the direction normal to the vapor–liquid interface and $-\infty$ to ∞ for that in the tangential direction. Equation (1.43) clearly shows that the mass flux induced by net evaporation/condensation is caused by the difference in the mass flux related to the velocity distribution functions f_{out} and f_{coll}. When f_{out} is the generalized KBC (Eq. (1.40)), we get the following expression.

$$\rho(v_i - v_{\mathrm{w}i})n_i = (\mathcal{A} - \sigma)\sqrt{\frac{RT_{\mathrm{L}}}{2\pi}}, \tag{1.44}$$

For example, when $\mathcal{A} = \alpha_{\mathrm{e}}\rho^* + (1 - \alpha_{\mathrm{c}})\sigma$, Eq. (1.44) becomes

$$\rho(v_i - v_{\mathrm{w}i})n_i = (\alpha_{\mathrm{e}}\rho^* - \alpha_{\mathrm{c}}\sigma)\sqrt{\frac{RT_{\mathrm{L}}}{2\pi}}. \tag{1.45}$$

We hereafter call Eq. (1.44) the *mass flux relation* for simplicity. In this thesis, we investigate Eq. (1.44) by the molecular simulation. From this result, we can determine α_{e} and α_{c} without explicitly defining the molecular processes illustrated in Fig. 1.1. Also, after determining α_{e} and α_{c} in this way, we can consider their physical meanings by investigating the relation between these coefficients and the molecular processes.

Let us now detail how to investigate and what to clarify together with the scope of this thesis. In Chapter 2, we first explain the vapor–liquid two-phase system to be considered. The system considered in this thesis is a steady one-dimensional net evaporation/condensation problem in vapor between two liquid slabs with the

different temperature. This problem is often called the two-surface problem. After explaining the one-dimensional problem of net evaporation/condensation, we introduce the features of the two-surface problem from the results of the previous studies. Next, we explain the molecular simulation method. The investigation of Eq. (1.44) requires to exhaustively and precisely obtain $\rho(v_i - v_{\mathrm{w}i})n_i$ under the various cases of net evaporation/condensation. However, the molecular dynamics simulation, which has been utilized as a molecular simulation, requires a high computational cost. Actually, in the previous studies [27, 29, 31, 32, 34–38], only in the several limited cases of net evaporation/condensation have been examined. In contrast, we focus on the novel molecular simulation method based on the mean-field kinetic theory proposed by Frezzotti *et al.* [43]. We can perform the molecular simulation for the one-dimensional net evaporation/condensation problem with less computational cost than the molecular dynamics simulation by utilizing this novel method.

In Chapter 3, we examine the mass flux relation (Eq. (1.44)) to find a pair of α_{e} and α_{c} defined by Eq. (1.42) by the molecular simulation based on the mean-field kinetic theory. We perform the molecular simulation for the two-surface problem in 160 cases of the temperature differences between two liquids. First, we confirm whether the normalized velocity distribution function of the KBC obeys Eq. (1.32) because the results of the previous studies [34, 38, 39, 41] indicated that the normalized velocity distribution function of the KBC deviates from Eq. (1.32) under strong net evaporation/condensation. Next, we formulate the mass flux relation at each liquid temperature by using $\rho(v_i - v_{\mathrm{w}i})n_i$ obtained by the molecular simulation and corresponding σ (Eq. (1.33)), and then we discuss α_{e} and α_{c} defined by Eq. (1.42) by comparing the formulated mass flux relation with Eq. (1.44). In this way, we can find a pair of α_{e} and α_{c} without explicitly defining the molecular processes illustrated in Fig. 1.1.

In Chapter 4, we consider the physical meaning of α_{e} and α_{c} obtained in Chapter 3. To determine α_{e} and α_{c} uniquely, we have to clarify the definitions of the

molecular processes illustrated in Fig. 1.1. Although this definition has not been clarified, if we assume a certain condition, these molecular processes can be distinguished. We here consider a hypothesis of the spontaneous evaporation [33, 44]. According to this hypothesis, α_{e} and α_{c} are defined by the mass fluxes related to the molecular processes. α_{e} and α_{c} according to this hypothesis can be obtained from the virtual vacuum simulation [26, 33] and the net evaporation and condensation simulation [34]. However, the virtual vacuum simulation is inappropriate when the liquid temperature becomes relatively high; hence, we apply a new method, which is called the *two-boundary method*, proposed by Kobayashi *et al.* [30] to estimate α_{e} and α_{c} according to the hypothesis of the spontaneous evaporation. First, we confirm whether the normalized velocity distribution function of the evaporation molecules is to be the normalized Maxwellian distribution (Eq. (1.32)), which is the premise of the hypothesis of the spontaneous evaporation. Next, we discuss the correspondence of the hypothesis of the spontaneous evaporation with α_{e} and α_{c} obtained in Chapter 3 by examining the mass fluxes of evaporation and condensation molecules in both the vapor–liquid equilibrium and net evaporation/condensation cases. In this way, we can find the relation among α_{e}, α_{c} obtained in Chapter 3, and the molecular processes illustrated in Fig. 1.1.

In Chapter 5, we verify the accuracy of α_{e} and α_{c} obtained in Chapter 3 and Chapter 4. We perform the molecular simulation for the different two vapor–liquid two-phase systems, which are distinct from that considered in the preceding chapters. First, in these two systems, we confirm whether the normalized velocity distribution function of the KBC obeys the normalized Maxwellian distribution (Eq. (1.32)). Next, we compare the macroscopic variables in vapor, namely, the velocity and the temperature, in these two systems obtained from the numerical simulation of the Boltzmann equation with the KBC, which is specified by α_{e} and α_{c} obtained in the preceding chapters, and those obtained from the molecular simulation based on the mean-field kinetic theory. Since it has been pointed out that the

KBC significantly affects the macroscopic variables in the numerical simulation of the Boltzmann equation [45–47], the proper specification of the KBC is critical. In other words, the KBC at the vapor–liquid interface with net evaporation/condensation is validated if and only if the macroscopic variables in vapor obtained from these two simulations accurately agree with each other. This simple validation method has often been performed in the molecular dynamics simulation [45, 46]. Finally, we compare the liquid temperature dependence of α_{e} and α_{c} in these two systems with those obtained in Chapter 3. In this way, we can verify whether α_{e} and α_{c} obtained in Chapter 3 and Chapter 4 depend on the simulation systems.

This thesis is based on the results of the previous journal papers and proceedings papers as shown in the following.

[48] M. Kon, K. Kobayashi, M. Watanabe, Physics of Fluids 26 (2014) 072003.

[49] M. Kon, K. Kobayashi, M. Watanabe, AIP Conference Proceedings 1628 (2014) 398–403.

[50] M. Kon, K. Kobayashi, K. Sasaki, M. Watanabe, Japanese Journal of Multiphase Flow (in Japanese) 99 (2015) 493–500.

[51] M. Kon, K. Kobayashi, M. Watanabe, International Journal of Heat and Mass Transfer 29 (2016) 317–326.

[52] M. Kon, K. Kobayashi, M. Watanabe, AIP Conference Proceedings 1786 (2016) 110002.

[53] M. Kon, K. Kobayashi, M. Watanabe, European Journal of Mechanics-B/Fluids (in press).

Chapter

2

Method

In this chapter, we first explain the vapor–liquid two-phase system to be considered. The system considered in this thesis is a steady one-dimensional net evaporation/condensation problem in vapor between two liquid slabs with the different temperature. This problem is often called the two-surface problem. After explaining the one-dimensional problem of net evaporation/condensation, we introduce the features of the two-surface problem from the results of the previous studies. Next, we explain the molecular simulation method. The investigation of Eq. (1.44) requires to exhaustively and precisely obtain $\rho(v_i - v_{\mathrm{w}i})n_i$ under the various cases of net evaporation/condensation. However, the molecular dynamics simulation, which has been utilized as a molecular simulation, requires a high computational cost. Actually, in the previous studies [27, 29, 31, 32, 34–36, 38], only in the several limited cases of net evaporation/condensation have been examined. In contrast, we focus on the novel molecular simulation method based on the mean-field kinetic theory proposed by Frezzotti et al. [43], which is referred to as the EV-DSMC simulation in this thesis. We can perform the molecular simulation for the one-dimensional net evaporation/condensation problem with less computational cost than the molecular dynamics simulation by utilizing the EV-DSMC simulation.

2.1 Problem

2.1.1 One-dimensional net evaporation/condensation

In this thesis, we consider the vapor–liquid two-phase system composed of single-component monatomic vapor and its condensed phase (liquid). As a fundamental

problem, we assume the planar vapor–liquid interface and neglect its advection and deformation ($v_{\mathrm{w}i}n_i = 0$). Under this assumption, we can regard net evaporation/condensation as a spatially one-dimensional problem with only in the direction normal to the vapor–liquid interface ($x_i n_i = z$). This is not an extreme assumption and is often utilized in the molecular gas dynamics analysis. Note that as for the molecular velocity space, we have to consider three-dimensions in this analysis. For example, Sone and his colleagues [12] comprehensively investigate the spatially one-dimensional net evaporation/condensation in the system composed of the plane condensed phase and semi-infinite vapor, that is, the half-space problem, by the Boltzmann equation or its model equation. The Knudsen layer analysis described in Chapter 1 is also a part of these studies.

In such a spatially one-dimensional net evaporation/condensation problem, the generalized KBC (Eq. (1.40)) can be expressed as

$$f_{\mathrm{out}} = \mathcal{A}\hat{f}^*, \qquad \xi_z > 0, \tag{2.1}$$

where

$$\hat{f}^* = \frac{1}{\sqrt{2\pi RT_{\mathrm{L}}}^3} \exp\left(-\frac{\xi_i^2}{2RT_{\mathrm{L}}}\right), \tag{2.2}$$

Also, the mass flux relation (Eq. (1.44)) becomes

$$\rho v_z = (\mathcal{A} - \sigma)\sqrt{\frac{RT_{\mathrm{L}}}{2\pi}}, \tag{2.3}$$

where

$$\sigma\sqrt{\frac{RT_{\mathrm{L}}}{2\pi}} = -\int_{\xi_z<0} \xi_z f_{\mathrm{coll}} \mathrm{d}\boldsymbol{\xi}. \tag{2.4}$$

When $\mathcal{A} = \alpha_{\mathrm{e}}\rho^* + (1 - \alpha_{\mathrm{c}})\sigma$, Eq. (2.3) becomes

$$\rho v_z = (\alpha_{\mathrm{e}}\rho^* - \alpha_{\mathrm{c}}\sigma)\sqrt{\frac{RT_{\mathrm{L}}}{2\pi}}. \tag{2.5}$$

We discuss, throughout this thesis, these spatially one-dimensional KBC and mass flux relation (Eqs. (2.1)–(2.5)).

2.1.2 Two-surface problem

Next, we explain the system mainly considered in this thesis. This system is composed of vapor between two parallel liquid slabs, that is, the *two-surface problem*. If two liquids are kept at the different temperatures, except in the special cases, net evaporation occurs at the vapor–liquid interface on the high-temperature side, while net condensation occurs at the vapor–liquid interface on the low-temperature side. According to the second law of thermodynamics, the heat flow from the high-temperature side to the low-temperature side becomes positive and the temperature gradient becomes negative in vapor. In contrast, Pao [24] reported that the temperature gradient in vapor from the high-temperature side to the low-temperature side becomes positive by the molecular gas dynamics analysis of the two-surface problem. This phenomenon that seems to be contradictory to the second law had been discussed as the *paradox of inverted temperature gradient*.

The inverted temperature gradient itself is not the scope of this thesis. We briefly introduce this phenomenon as a characteristic feature of the two-surface problem. Initially, the inverted temperature gradient had been thought to be an unphysical phenomenon caused by utilizing the uncertain KBC [54, 55]. A few years later, it was shown that this phenomenon does not violate nonequilibrium thermodynamics [56–59]. At present, it is clarified by the molecular gas dynamics analysis that the cause of the inverted temperature gradient is the temperature jump, which is the temperature difference between liquid and vapor in contact with

the vapor–liquid interface, accompanied with net evaporation/condensation [12, 47]. The temperature jump increases according to the vapor velocity induced by net evaporation/condensation, and then the inverted temperature gradient occurs when the temperature jump at each vapor–liquid interface exceeds the mean temperature of two liquids. Furthermore, it is also shown by the molecular dynamics simulation that the inverted temperature gradient certainly occurs in the two-surface problem [45, 46, 60, 61].

As described above, the two-surface problem is addressed by various approaches, such as molecular gas dynamics, nonequilibrium thermodynamics, and molecular dynamics. Although the examination of the inverted temperature gradient is not the scope of this thesis, these results are relevant in discussing the accuracy of the molecular simulation based on the mean-field kinetic theory. Moreover, in this thesis, we have to obtain ρv_z under various cases of net evaporation/condensation to investigate Eq. (2.3). One of the advantages of using this system is that it is easy to change ρv_z by changing the temperature difference between two liquids.

2.2 Mean field kinetic theory

In this thesis, we perform the molecular simulation based on the mean-field kinetic theory. We here describe the mean-field kinetic theory and the Enskog–Vlasov equation derived from this theory. The Enskog–Vlasov equation is an equation that extends the Boltzmann equation for the ideal gas to both vapor and liquid under some approximation and assumption. Although the premise of the Enskog–Vlasov equation is not mathematically clear as compared with that of the Boltzmann equation, describing the vapor–liquid two-phase flow by using the velocity distribution function is useful for the molecular simulation explained in the next section. We preliminarily explain the Enskog theory and the Enskog equation derived from this theory, which is the basis of the mean-field kinetic theory. We also discuss the relation between the Enskog–Vlasov equation and the Boltzmann equation because the

solution of the Enskog–Vlasov equation in vapor should be consistent with that of the Boltzmann equation to examine the KBC for the Boltzmann equation.

2.2.1 Enskog equation

We here explain the Enskog theory and the Enskog equation derived from this theory. Since the Boltzmann equation is derived under the ideal gas condition ($na^3 \to 0$), it cannot be applied to dense fluids. In the Enskog theory, we extend the Boltzmann equation to dense fluids with finite na^3 under some assumption. Ideas proposed in the Enskog theory [62] are listed below:

1. The multiple collisions are completely neglected, and the binary collision is only described.

2. The collision frequency is modified by a factor, which is the function of the number density, and the centers of two molecules are separated by the diameter of a hard-sphere molecule a.

3. The momentum exchanged between the molecules is suddenly transferred from the center of a molecule to that of the other, that is, the *collisional transfer*. As for the quite dense gas, molecules cannot move without the collision, in which case the collisional transfer is dominant for the momentum transfer.

Here, we provide additional explanations regarding these assumptions. Similar to the Boltzmann equation, a conventional starting point to describe N-particle system is the BBGKY hierarchy equation. The Enskog theory is a theory for the hard-sphere fluid having a finite diameter a. Obviously, this fluid does not satisfy the Grad-Boltzmann limit ($n \to \infty$ and $a \to 0$ with fixed na^2), and therefore it has never been mathematically proven that the triple or more multiple collisions can be neglected. However, only the binary collision is considered approximately in the Enskog theory. It is not well understood why these assumptions turn out to be qualitatively correct. That is why the Enskog theory is not mathematically clear as

compared with the derivation of the Boltzmann equation. On the other hand, the Enskog theory provides a very useful *approximation* for the dense fluid because of its simplicity.

Under these approximations and assumptions, the Enskog equation for the one-particle distribution function is derived from the BBGKY hierarchy equation as follows [21, 62]:

$$\frac{\partial f}{\partial t} + \xi_i \frac{\partial f}{\partial x_i} = C_{\mathrm{E}}, \tag{2.6}$$

$$\begin{aligned} C_{\mathrm{E}} = \frac{a^2}{m} \int_{\text{all } K_i,\ \text{all } \xi_{1i}} & [Y f(\boldsymbol{x} + a\boldsymbol{K}, \boldsymbol{\xi}_1', t) f(\boldsymbol{x}, \boldsymbol{\xi}', t) \\ & - Y f(\boldsymbol{x} - a\boldsymbol{K}, \boldsymbol{\xi}_1, t) f(\boldsymbol{x}, \boldsymbol{\xi}, t)] H(\boldsymbol{\xi}_{\mathrm{r}} \cdot \boldsymbol{K})(\boldsymbol{\xi}_{\mathrm{r}} \cdot \boldsymbol{K}) \mathrm{d}\boldsymbol{\xi}_1 \mathrm{d}^2\boldsymbol{K}. \end{aligned} \tag{2.7}$$

where x_i indicates the position of the center of the molecule under consideration, $x_i - aK_i$ indicates that of another molecule, H is the Heaviside function, and $\xi_{\mathrm{r}i} = \xi_{1i} - \xi_i$. The post-collisional velocities ξ_i' and ξ_{1i}' are obtained from Eq. (1.20). In Eq. (2.7), Y is a pair correlation function in Eq. (1.17). Note that in the Enskog theory, the molecular chaos assumption ($Y = 1$), which introduced when we derive the Boltzmann equation from the BBGKY hierarchy equation, does not hold. In the original Enskog theory [62], Y can be identified with the local pair correlation function, which calculated by the density at the contact point of two molecules. In contrast, the revised Enskog theory [63] is proposed to have an H-theorem, where Y is expressed from an approximation that the only correlations in the system are due to the excluded volume between the molecules at any time; in particular, no correlations between velocities are retained.

According to the revised Enskog theory, Y have been proposed in various ways [64, 65]. It, however, is difficult to find the exact pair correlation function based on Eq. (1.17). We here introduce a simpler method using the result of the Chapman–

Enskog approximation. The Chapman–Enskog approximation is a kind of successive approximation, which is a widely used method for solving the Boltzmann equation [66]. In this approximation, the velocity distribution functions f is expanded in an infinite series around the local equilibrium distribution. Substituting this expanded f into the Boltzmann equation, we obtain the equations for each order. These equations are not closed. We first impose a condition to determine the 0th order f uniquely. Since the 0th order f is the local equilibrium distribution, we obtain f of 1st order, 2nd order, 3rd order, and so on successively. From this result, f in each order is known, so that we can obtain the expression of the macroscopic variables. Similar to the Boltzmann equation, this approximation can also be applied to the Enskog equation [65, 67].

We obtain the following expression for the pressure p from the 0th order approximation of the stress tensor by the Chapman–Enskog approximation for the Enskog equation.

$$p = nk_{\mathrm{B}}T\left(1 + \frac{2}{3}\pi na^3 Y\right), \tag{2.8}$$

Solving this equation for Y, we get

$$Y(n) = \frac{1}{nb}\left(\frac{p}{nk_{\mathrm{B}}T} - 1\right), \tag{2.9}$$

where n is the number density, k_{B} is the Boltzmann constant, and $b = (2/3)\pi a^3$. Although Eq. (2.9) does not directly find the pair correlation, Résibois [65] defined Eq. (2.9) as the pair correlation function. We can obtain another expression of the pair correlation function by utilizing other methods [64,68]. In this thesis, we utilize Eq. (2.9) as the pair correlation function according to Frezzotti *et al.* [43, 69]. In Eq. (2.9), if we specify the equation of state of the hard-sphere molecules, $Y(n)$ is entirely defined.

2.2.2 Enskog–Vlasov equation

We describe the mean-field kinetic theory and the Enskog–Vlasov equation derived from this theory. The mean-field kinetic theory is based on the revised Enskog theory. In the mean-field kinetic theory, a kinetic equation is obtained by generalizing to a potential with hard-sphere core plus smooth attractive tail, which is suited to liquid dynamics. The hard-sphere fluid structure serves as a reference structure for the potential tail. When the potential tail is set to zero, the revised Enskog theory is recovered. Similar to the Enskog theory, we ignore the triple or more multiple collisions and consider only the binary collision approximately.

A kinetic equation for the one-particle distribution function including a term related to the potential tail, $\phi_{\rm tail}$, is obtained from the BBGKY hierarchy equation [21, 64].

$$\begin{aligned}\frac{\partial f}{\partial t}+\xi_i\frac{\partial f}{\partial x_i} &= -\frac{\partial}{\partial \xi_i}f(\boldsymbol{x},\boldsymbol{\xi},t)\left[\int_{\text{all }\xi_{1i},\ r>a} K_i\frac{\mathrm{d}\phi_{\rm tail}}{\mathrm{d}r}f(\boldsymbol{x}_1,\boldsymbol{\xi}_1,t)\mathrm{d}\boldsymbol{x}_1\mathrm{d}\boldsymbol{\xi}_1\right]+C_{\rm E},\\ &= -\frac{1}{m}\frac{\partial}{\partial \xi_i}f(\boldsymbol{x},\boldsymbol{\xi},t)\left[\int_{r>a} K_i\frac{\mathrm{d}\phi_{\rm tail}}{\mathrm{d}r}n(\boldsymbol{x}_1,t)\mathrm{d}\boldsymbol{x}_1\right]+C_{\rm E},\end{aligned} \tag{2.10}$$

where a term related to $\phi_{\rm tail}$ is the *mean-field term* that is obtained by a self-consistent field approximation for the potential tail [64], x_i and x_{1i} indicate the positions of the center of molecules, r is the relative distance between the center of molecules ($r = |\boldsymbol{x}_1 - \boldsymbol{x}|$), m is the mass of a molecule, and K_i is the unit vector ($K_i = (\boldsymbol{x}_1 - \boldsymbol{x})/|\boldsymbol{x}_1 - \boldsymbol{x}|$). The post-collisional velocities ξ_i' and ξ_{1i}' are obtained from Eq. (1.20). Note that the pair correlation in the mean-field term is completely neglected ($Y = 1$). It is shown that for most liquids, Y in Eq. (1.17) is approximately unity beyond the distance of the molecular diameter ($r > a$) [70].

By imposing a limit, which is equivalent to set $a = 0$ in the mean-field term integral, a reference structure for the attractive tail appears linearly in the mean-field term. In this thesis, we do not impose this limit in the mean-field term integral and utilize Eq. (2.10) directly for the molecular simulation. Further deformation of

Eq. (2.10) yields

$$\frac{\partial f}{\partial t} + \xi_i \frac{\partial f}{\partial x_i} + \frac{F_i(\boldsymbol{x}, t)}{m} \frac{\partial f}{\partial \xi_i} = C_{\mathrm{E}}, \tag{2.11}$$

where the mean-field term appears as an external force term,

$$F_i(\boldsymbol{x}, t) = \int_{r>a} K_i \frac{\mathrm{d}\phi_{\mathrm{tail}}}{\mathrm{d}r} n(\boldsymbol{x}_1, t) \mathrm{d}\boldsymbol{x}_1. \tag{2.12}$$

Equation (2.11) is called the Enskog–Vlasov equation. To derive Eq. (2.12), we apply the definition of the density (Eq. (1.7)). In the mean-field kinetic theory, the density, the velocity, the temperature, and the mass flux are defined by only f (Eqs.(1.7)–(1.9) and (1.14)). In contrast, other macroscopic variables and fluxes, namely, the pressure, the specific internal energy, the stress tensor, the heat flux, the momentum flux vector, and the energy flux, cannot be defined by only f because the collisional transfer and/or the potential contribution should be taken into account. We can identify these macroscopic variables and fluxes only in local equilibrium by specifying the collision term, the intermolecular potential, and the equation of state [43,67,71]. However, when the effect of the collisional transfer and the potential contribution is sufficiently small, these macroscopic variables and fluxes can be obtained from Eqs. (1.10)–(1.13), (1.15), and (1.16).

H-theorem

We hereafter give further explanations on the Enskog–Vlasov equation through the comparison with the Boltzmann equation. Several studies [64, 72] have reported the H-theorem in the Enskog–Vlasov equation. The H-theorem is a feature of the Boltzmann equation and is also important to guarantee the availability of its model equations. We here briefly introduce the results for the H-theorem in the Enskog–Vlasov equation which Sobrino investigated in the simplified case of $Y = 1/(1-bn)$.

Sobrino [64] defined the following H function which depends on Y,

$$H = \int_{\text{all } \xi_i} f \ln(Yf/c) \mathrm{d}\boldsymbol{\xi}, \tag{2.13}$$

and a function, $\mathcal{H}$, obtained by integrating the H function with respect to the domain $\mathcal{D}$,

$$\mathcal{H} = \int_{\mathcal{D}} H \mathrm{d}\boldsymbol{x}. \tag{2.14}$$

Sobrino [64] showed that H and $\mathcal{H}$ never increases because the following inequality holds, similar to the Boltzmann equation.

$$\begin{aligned} &\frac{\mathrm{d}\mathcal{H}}{\mathrm{d}t} - (\ln Y + bYn) \int_{\partial\mathcal{D}} H_i n_i \mathrm{d}S \\ &= \int_{\mathcal{D}} \left(\int_{\text{all } \xi_i} [1 + \ln(f/c)] C_{\mathrm{E}} \mathrm{d}\boldsymbol{\xi} - \frac{1}{m} \frac{\partial f}{\partial \xi_i} \int_{r>a} \frac{\mathrm{d}\phi_{\text{tail}}}{\mathrm{d}r} n(\boldsymbol{x}_1, t) \mathrm{d}\boldsymbol{x}_1 \right) \mathrm{d}\boldsymbol{x} \leq 0, \end{aligned} \tag{2.15}$$

where

$$H_j = \int_{\text{all } \xi_i} \xi_j f \ln(f/c) \mathrm{d}\boldsymbol{\xi}. \tag{2.16}$$

In this inequality, the equal sign valid only when f is the local equilibrium distribution. Sobrino [64] derived the term related to the potential contribution in the above inequality by defining the functional form of the potential tail ϕ_{tail}, but we omit its derivation here.

Equilibrium solution of Enskog–Vlasov equation

It was shown from the H-theorem proved by Sobrino [64] that the equilibrium solution of the Enskog–Vlasov equation must be sought among the local, time-

independent, Maxwellian distribution,

$$f^* = \frac{\rho(\boldsymbol{x})}{\sqrt{2\pi RT(\boldsymbol{x})}^3} \exp\left(-\frac{(\xi_i - v_i(\boldsymbol{x}))^2}{2RT(\boldsymbol{x})}\right). \tag{2.17}$$

We restrict ourselves to the case $v_i(\boldsymbol{x}) = 0$ for simplicity. When the space-independent temperature is lower than the critical temperature obtained from the Van der Waals equation of state, the Enskog–Vlasov equation has two types of the equilibrium solutions [64, 73]: (i) space-independent solutions corresponding to state with a single-phase, which are not entirely stable but identified with metastable states if the compressibility is positive and (ii) space-dependent solutions which are identified with the vapor–liquid equilibrium state. Since the objective of this thesis is the vapor–liquid two-phase system below the critical temperature, the equilibrium solution of the Enskog–Vlasov equation is as follows:

$$f^* = \frac{\rho(\boldsymbol{x})}{\sqrt{2\pi RT}^3} \exp\left(-\frac{\xi_i^2}{2RT}\right). \tag{2.18}$$

When $\rho(\boldsymbol{x})$ in vapor equals to the saturated vapor density ρ^* at the liquid temperature T_L, Eq. (2.18) becomes the equilibrium solution of the Boltzmann equation in vapor,

$$f^* = \frac{\rho^*}{\sqrt{2\pi RT_\mathrm{L}}^3} \exp\left(-\frac{\xi_i^2}{2RT_\mathrm{L}}\right). \tag{2.19}$$

Mean free path

We describe the mean free path based on the Enskog theory. In the Enskog theory, we modify the collision frequency of the Boltzmann equation by Y. On the basis of Eq. (2.7), the mean collision frequency according to the Enskog theory is

$$\bar{\mu} = Y 4na^2\sqrt{\pi RT}. \tag{2.20}$$

The substitution of Eq. (1.29) and the average molecular speed (Eq. (1.27)) into the definition of the mean free path (Eq. (1.26)) yields

$$\ell = \frac{1}{Y\sqrt{2}\pi n a^2}, \tag{2.21}$$

that is, the mean free path in the Enskog theory. Naturally, the mean free path of the Enskog equation corresponds with that of the Boltzmann equation for $Y = 1$.

Transport properties

Here, we describe the expressions of the transport properties, namely, the viscosity coefficient and the thermal conductivity, as the characteristics of the fluid based on the Enskog theory. We derive these expressions by the Chapman–Enskog approximation for the Enskog equation. This procedure is often used for obtaining these transport properties of the Boltzmann equation [66].

In the 1st approximation, the expressions of the viscosity coefficient, κ_{B}, and the thermal conductivity, λ_{B}, for the Boltzmann equation with the hard-sphere model are given by

$$\kappa_{\mathrm{B}} = \frac{5}{16a^2}\sqrt{\frac{mk_{\mathrm{B}}T}{\pi}}, \qquad \lambda_{\mathrm{B}} = \frac{75}{64a^2}\sqrt{\frac{k_{\mathrm{B}}^3 T}{\pi m}}. \tag{2.22}$$

Note that to obtain these expressions from the results of the Chapman–Enskog approximation, we utilized several mathematical methods (for details, see the literature [65]).

Also, as described in the former section, we can apply the Chapman–Enskog approximation for the Enskog equation. In the 1st approximation, the expressions of the viscosity coefficient, κ_{E}, and the thermal conductivity, λ_{E}, for the Enskog

equation are given below.

$$\frac{\kappa_{\mathrm{E}}}{\kappa_{\mathrm{B}}} = \frac{1}{Y(n)}\left[1 + \frac{4}{5}(nbY(n)) + \left(\frac{4}{45} + \frac{48}{25\pi}\right)(nbY(n))^2\right], \tag{2.23}$$

$$\frac{\lambda_{\mathrm{E}}}{\lambda_{\mathrm{B}}} = \frac{1}{Y(n)}\left[1 + \frac{5}{6}(nbY(n)) + \left(\frac{9}{25} + \frac{32}{25\pi}\right)(nbY(n))^2\right]. \tag{2.24}$$

These transport properties of the Enskog equation corresponds with that of the Boltzmann equation when $na^3 \to 0$ and $Y = 1$.

We introduce the previous studies which calculated the transport properties from Eqs. (2.23) and (2.24). Dymond and Alder [74] calculated these transport properties for extremely dense gas from Eqs. (2.23) and (2.24) and compared these with the results of the experiment. As a result, it was shown that the transport properties calculated from Eqs. (2.23) and (2.24) agree with the experimental data, even at the high temperatures. The difference between these results is approximately 10%. Karkheck and Stell [71] compared these transport properties with the experimental data to investigate whether the expressions of these transport properties (Eqs. (2.23) and (2.24)) can be applied to liquid. As a result, it was shown that the temperature characteristics of the transport properties calculated from Eqs. (2.23) and (2.24) agree with the experimental data even in liquid.

2.3 Numerical method

So far, we have shown the general framework of the mean-field kinetic theory. We demonstrate the numerical method based on this theory from here.

2.3.1 Intermolecular potential and equation of state

Sutherland potential

Here, we specify the intermolecular potential. In this thesis, we utilize the following intermolecular potential named the Sutherland potential, which is an ideal potential

having a hard-sphere core plus smooth attractive tail.

$$\phi(r) = \begin{cases} +\infty & (r < a) \\ -\phi_a \left(\frac{r}{a}\right)^{-\gamma} & (r \geq a), \end{cases} \tag{2.25}$$

where ϕ_{a} and γ are constants which are related to the depth of the potential well at $r = a$ and the range of the attractive tail, respectively; γ is set to six to follow the attractive tail of the 12–6 Lennard-Jones intermolecular potential in this simulation.

Equation of state for hard-sphere with attractive tail

Next, we describe the equation of state. In this thesis, we consider the following expression.

$$p = p_{\mathrm{hs}} + p_{\mathrm{tail}}, \tag{2.26}$$

where, p_{hs} indicates the hard-sphere contribution to the total pressure, and p_{tail} indicates the potential contribution to the total pressure. We utilize the following Carnahan and Starling approximation [75] for p_{hs}.

$$p_{\mathrm{hs}} = n k_{\mathrm{B}} T \frac{1 + \eta + \eta^2 - \eta^3}{(1 - \eta)^3}, \tag{2.27}$$

where $\eta = (1/6)\pi a^3 n$. It is shown that this expression of p_{hs} gives a prediction that is closer to the real molecules than the Van der Waals equation of state [75].

As for p_{tail}, we consider the modified term due to the attractive intermolecular force that is proportional to n^2 ($p_{\mathrm{tail}} = \mathscr{P} n^2$), similar to the Van der Waals equation of state. Since we already specify the functional form of the intermolecular potential (Eq. (2.25)), $\mathscr{P}$ can be obtained from the virial [76] as

$$\mathscr{P} = -\frac{2}{3}\pi \int_a^\infty r^2 \phi'_{\mathrm{tail}}(r) \mathrm{d}r, \qquad \phi'_{\mathrm{tail}}(r) = r \frac{\mathrm{d}\phi_{\mathrm{tail}}(r)}{\mathrm{d}r}. \tag{2.28}$$

From the attractive tail of the Sutherland potential (Eq. (2.25)), we get $\mathscr{P} = -(2/3)\pi a^3 \phi_a \gamma(\gamma-3)^{-1}$ when $\gamma > 3$. Using the above results, the equation of state considered in this thesis is obtained as follows:

$$p = nk_{\mathrm{B}}T\frac{1+\eta+\eta^2-\eta^3}{(1-\eta)^3} - \frac{2}{3}\pi a^3\phi_a\frac{\gamma}{\gamma-3}n^2. \tag{2.29}$$

This equation of state is the same as that utilized by Frezzotti *et al.* [43].

Now we specify the equation of state and therefore we can determine the pair correlation function $Y(n)$ from Eq. (2.9). We consider only $Y(n)$ for the hard-sphere contribution because $Y(n)$ is set to unity on the mean-field term in Eq. (2.11). Such $Y(n)$ is given by Eq. (2.27) as

$$Y(n) = \frac{1}{nb}\left(\frac{p_{\mathrm{hs}}}{nk_{\mathrm{B}}T} - 1\right) = \frac{1}{2}\frac{2-\eta}{(1-\eta)^3}. \tag{2.30}$$

Critical point

In the molecular simulation of this thesis, we use the macroscopic variables at the critical point as the reference values for the nondimensionalization. We here show the expressions of the critical number density, n_{c}, and the critical temperature, T_{c}, derived from the equation of state (Eq. (2.29)). We apply the condition of the critical point in the Van der Waals equation of state,

$$\left(\frac{\partial p(T,n)}{\partial n}\right)_T = 0, \qquad \left(\frac{\partial^2 p(T,n)}{\partial n^2}\right)_T = 0, \tag{2.31}$$

to Eq. (2.29), where $()_T$ indicates the partial differentiation with T as a constant. By solving these simultaneous equations, n_{c} and T_{c} can be obtained as

$$\frac{1}{6}\pi a^3 n_{\mathrm{c}} = 0.130443, \qquad T_{\mathrm{c}} = 0.094329\frac{4\gamma}{\gamma-3}\frac{\phi_a}{k_{\mathrm{B}}}. \tag{2.32}$$

It should be noted that these macroscopic variables at the critical point are derived from the equation of state; hence, these results do not guarantee that the Enskog–Vlasov equation has the solution at the critical point. In contrast, we can define the local Maxwellian distribution using the macroscopic variables at the critical point obtained from the equation of state, and that can be a solution of the Enskog–Vlasov equation.

2.3.2 Direct simulation Monte Carlo

Let us explain the numerical method for the Enskog–Vlasov equation (Eq. (2.11)). In this thesis, instead of solving the Enskog–Vlasov equation by the finite difference method, we adopt a method of replacing it with the equivalent molecular simulation. This method is based on the direct simulation Monte Carlo (DSMC) known as the stochastic simulation of the Boltzmann equation. Several studies [67, 69] tried to apply the DSMC simulation to the Enskog equation. In particular, Frezzotti [69] proposed the DSMC simulation for the Enskog equation which can exactly conserve the momentum and the energy. Moreover, Frezzotti *et al.* [43] extended this simulation method to the Enskog–Vlasov equation and proposed it as one of the molecular simulation methods that can simulate the vapor–liquid two-phase flow. In this thesis, we utilize this molecular simulation method proposed by Frezzotti *et al.* [43]. We hereafter call this molecular simulation the EV-DSMC simulation.

The EV-DSMC simulation is similar to the molecular dynamics simulation for the monatomic molecules, which tracks the temporal evolution of the positions and the velocities of molecules under a certain intermolecular potential. The difference between these two molecular simulations is that the molecular dynamics simulation handles the intermolecular collision process as deterministic, while the EV-DSMC simulation handles that as stochastic. Also, molecular dynamics requires the spatially three-dimensional simulation, while the EV-DSMC simulation can perform the spatially one-dimensional simulation. Therefore, we can reduce

the computational cost as compared with the molecular dynamics simulation for the monatomic molecules in a similar system by utilizing the EV-DSMC simulation. Reducing the computational cost is a significant advantage in this thesis because we have to perform the molecular simulation in the cases of various net evaporation/condensation. Barbante [77] showed that the EV-DSMC simulation for the spatially one-dimensional flow runs about 50–60 times faster than an equivalent molecular dynamics simulation with the same number of molecules. Furthermore, several studies confirmed that the macroscopic variables in the vapor–liquid two-phase system obtained from the EV-DSMC simulation show similar tendencies with those obtained from the molecular dynamics simulations for the monatomic molecules [39, 43, 48, 50, 51, 78].

In the EV-DSMC simulation, we discretize the finite time and space as Δt and $\Delta \boldsymbol{x}$, respectively. The EV-DSMC simulation handles both liquid and vapor of the different scales. It is necessary to select Δt and $\Delta \boldsymbol{x}$ based on the characteristic time and volume in liquid because these scales in liquid are smaller than those in vapor. The conditions of Δt and $\Delta \boldsymbol{x}$ are shown as follows:

$$\Delta t \ll \min(\bar{\mu}_{\mathrm{L}}^{-1}), \qquad \Delta \boldsymbol{x} \ll \min(a^3), \tag{2.33}$$

where $\bar{\mu}_{\mathrm{L}}^{-1}$ is the inverse of the mean collision frequency (Eq. (2.20)) in liquid, that is, the mean free time in liquid.

Principle of uncoupling

We hereafter explain the concept and the procedure of the EV-DSMC simulation. We can separate the advection and collision processes of molecules by taking sufficiently small Δt (Eq. (2.33)), that is, the *principle of uncoupling* [79, 80]. Applying the principle of uncoupling to the Enskog–Vlasov equation, we get the following

conceptual expression.

$$\frac{\partial f}{\partial t} + \xi_i \frac{\partial f}{\partial x_i} + \frac{F_i(\boldsymbol{x}, t)}{m} \frac{\partial f}{\partial \xi_i} = 0, \tag{2.34}$$

$$\frac{\partial f}{\partial t} = C_{\mathrm{E}}. \tag{2.35}$$

Equations (2.34) and (2.35) express the advection and collision processes, respectively.

More detailed derivation of the principle of uncoupling is shown below. We rewrite the Enskog–Vlasov equation (Eq. (2.11)) as follows:

$$\frac{\partial f}{\partial t} = -\mathscr{D}_1[f] - \mathscr{D}_2[f] + \mathscr{D}_3[f], \tag{2.36}$$

where $\mathscr{D}_1$, $\mathscr{D}_2$, and $\mathscr{D}_3$ are the operators,

$$\mathscr{D}_1[f] = \xi_i \frac{\partial f}{\partial x_i}, \quad \mathscr{D}_2[f] = \frac{F_i(\boldsymbol{x}, t)}{m} \frac{\partial f}{\partial \xi_i}, \quad \mathscr{D}_3[f] = C_{\mathrm{E}}. \tag{2.37}$$

The EV-DSMC method is a technique to obtain the solution at an arbitrary time $t = \Delta t$ from the solution at $t = 0$ (initial condition). For sufficiently small Δt, we have

$$f(\boldsymbol{x}, \boldsymbol{\xi}, \Delta t) = f(\boldsymbol{x}, \boldsymbol{\xi}, 0) + \left(\frac{\partial f(\boldsymbol{x}, \boldsymbol{\xi}, t)}{\partial t} \right)_{t=0} \Delta t. \tag{2.38}$$

With the use of Eq. (2.36), it becomes

$$\begin{aligned} f(\boldsymbol{x}, \boldsymbol{\xi}, \Delta t) &= f(\boldsymbol{x}, \boldsymbol{\xi}, 0) + (-\mathscr{D}_1[f] - \mathscr{D}_2[f] + \mathscr{D}_3[f])_{t=0} \Delta t, \\ &= (1 - \mathscr{D}_1 \Delta t - \mathscr{D}_2 \Delta t + \mathscr{D}_3 \Delta t) f(\boldsymbol{x}, \boldsymbol{\xi}, 0), \end{aligned} \tag{2.39}$$

and this equation can be rewritten as

$$f(\boldsymbol{x}, \boldsymbol{\xi}, \Delta t) = (1 - \mathscr{D}_1 \Delta t - \mathscr{D}_2 \Delta t)(1 + \mathscr{D}_3 \Delta t) f(\boldsymbol{x}, \boldsymbol{\xi}, 0). \tag{2.40}$$

Disregarding the term smaller than $O[\Delta t^2]$ in Eq. (2.40), we get Eq. (2.39). Equation (2.40) states the principle of uncoupling. The evolution of f during Δt can be divided into the advection and collision processes. In the advection process, f is changed due to the operator $(1 - \mathscr{D}_1 \Delta t - \mathscr{D}_2 \Delta t)$, that is, a collisionless motion of molecules. In the collision process, f is changed due to the operator $(1 + \mathscr{D}_3 \Delta t)$, that is, the collisional relaxation.

Velocity distribution function expressed by delta function

An important point in the EV-DSMC method is to track the molecular motion instead of solving f directly. A method of rewriting f as the sum of delta function (Dirac's delta) is often used as a concept for replacing a kinetic equation governing f with equivalent molecular simulation. For simplicity, we denote f (defined by Eq. (1.6)) divided by the mass of a molecule m as f'. f' expanded by the delta function at an arbitrary point $(\boldsymbol{x}, \boldsymbol{\xi}, t)$ in the system with the number of molecules N_{mol} $(i = 1, 2, ..., N_{\mathrm{mol}})$ is rewritten as

$$f'(\boldsymbol{x}, \boldsymbol{\xi}, t) = \sum_{i}^{N_{\mathrm{mol}}} \delta(\boldsymbol{x} - \boldsymbol{x}_{(i)}) \delta(\boldsymbol{\xi} - \boldsymbol{\xi}_{(i)}), \tag{2.41}$$

where subscripts in the parentheses denote the molecular number; $\boldsymbol{x}_{(i)}$ and $\boldsymbol{\xi}_{(i)}$ indicate the position and velocity of the ith molecules at time t. Each term of the delta function in this expansion corresponds to each molecule, and $\boldsymbol{x}_{(i)}$ and $\boldsymbol{\xi}_{(i)}$ correspond to the position and velocity of the ith molecule. Also, when the number of cells is defined as N_{cell} $(l = 1, 2, ..., N_{\mathrm{cell}})$ and the number of molecules in the lth cell is defined as $N_{\mathrm{mol}}^{(l)}$ $(j = 1, 2, ..., N_{\mathrm{mol}}^{(l)})$, f' in the lth cell whose reference point is

$\boldsymbol{x}$ can be rewritten as

$$f'(\boldsymbol{x}, \boldsymbol{\xi}, t) = \frac{n^{(l)}}{N_{\mathrm{mol}}^{(l)}} \sum_{j}^{N_{\mathrm{mol}}^{(l)}} \delta(\boldsymbol{\xi} - \boldsymbol{\xi}_{(j)}^{(l)}), \tag{2.42}$$

where superscripts in the parentheses denote the cell number; $n^{(l)}$ indicates the number density in the lth cell and $\boldsymbol{\xi}_{(j)}^{(l)}$ indicates the velocity of the jth molecules in the lth cell. From this expanded f', the macroscopic variables defined by f, such as the density, the velocity, and the temperature in the lth cell are obtained as follows:

- Density ρ:

$$\rho = m \frac{N_{\mathrm{mol}}^{(l)}}{\mathrm{d}\boldsymbol{x}}. \tag{2.43}$$

- Velocity v_i

$$v_j = \frac{1}{N_{\mathrm{mol}}^{(l)}} \sum_{j}^{N_{\mathrm{mol}}^{(l)}} \boldsymbol{\xi}_{(j)}^{(l)}. \tag{2.44}$$

- Temperature T

$$T = \frac{1}{N_{\mathrm{mol}}^{(l)}} \sum_{j}^{N_{\mathrm{mol}}^{(l)}} (\boldsymbol{\xi}_{(j)}^{(l)} - \sum_{k}^{N_{\mathrm{mol}}^{(l)}} \boldsymbol{\xi}_{(k)}^{(l)})^2. \tag{2.45}$$

Equations (2.43)–(2.45) ideally can approximate Eqs. (1.7)–(1.9) by taking a sufficient number of terms in the delta function. In the same way, we can also get other macroscopic variables and fluxes defined by f when the effect of the collisional transfer and the potential contribution is sufficiently small.

Advection process

We here show how the advection process (Eq. (2.34)) is dealt in the EV-DSMC simulation. We consider the position and the velocity of the ith molecules after Δt,

which have the velocity $\boldsymbol{\xi}_{(i)}$ and the position $\boldsymbol{x}_{(i)}$ at the time t. The motion of such a molecule follows the following Newton's equation of motion.

$$\frac{\mathrm{d}^2\boldsymbol{x}_{(i)}(t)}{\mathrm{d}t^2} = \frac{F_i(\boldsymbol{x},t)}{m}. \tag{2.46}$$

where $F_i(\boldsymbol{x},t)$ indicates the mean-field term as specified in Eq. (2.12). In the spatially one-dimensional problem, Eq. (2.12) can be simplified as [43].

$$F_z(z,t) = 2\pi\phi_a \left[a^\gamma \int_{|z-z'|>a} \frac{(z'-z)}{|z-z'|^\gamma} n(z',t)\mathrm{d}z' + \int_{|z-z'|\leq a} (z'-z)n(z',t)\mathrm{d}z' \right], \tag{2.47}$$

where z indicates the reference point of the cell under consideration, and z' indicates that of other cells. We obtain the following position and velocity of molecules by solving the z-component of Eq. (2.46) by the leapfrog method.

$$z_{(i)}(t+\Delta t) = z_{(i)}(t) + \xi_{z(i)}(t+\Delta t/2)\Delta t, \tag{2.48}$$

$$\xi_{z(i)}(t+\Delta t/2) = \xi_{z(i)}(t-\Delta t/2) + \frac{F_z(z,t)}{m}\Delta t, \tag{2.49}$$

where the term smaller than $O[\Delta t^2]$ are neglected. Obviously, since F_z affects only in the z direction, $\xi_{x(i)}$ and $\xi_{y(i)}$ are not changed in the advection process.

Collision process

We here show how the collision process (Eq. (2.35)) is dealt in the EV-DSMC simulation. The handling of the collision term is a characteristic feature of the EV-DSMC simulation. In molecular dynamics simulation, the collision processes with all molecules are dealt deterministically with according to the intermolecular force. On the other hand, the DSMC simulation does not deal with the collision processes with all molecules. In the DSMC simulation, the collision pair is statistically selected according to the collision probability, and the velocities of molecules are replaced at

which this event occurred. This concept is the same in the EV-DSMC simulation as well.

We explain how to choose the collision pairs in the EV-DSMC simulation. The contents of this section are based on the literature [43, 69]. As for the Boltzmann equation, the collision integral has a local character; therefore, the collision pairs are selected from the molecules belonging to the same cell in the DSMC method. In contrast, as for the Enskog–Vlasov equation, the collision integral involves the distribution function at the different position; therefore, the molecules in a given cell interact with that located in nearby cells in the EV-DSMC method. Accordingly, to estimate the collision probability, it is necessary to predict the number of collisions in a domain where molecules may interact.

When the domain under consideration is $\mathcal{D}$, the expected number of collision, $N_{\rm coll}$, during Δt in $\mathcal{D}$ can be obtained from Eq. (2.7) as

$$\begin{aligned} N_{\rm coll} =& \frac{1}{2}\int_{\mathcal{D}} \mathrm{d}\boldsymbol{x} \int_{\text{all } \xi_i} \mathrm{d}\boldsymbol{\xi} \int_{\text{all } \xi_{1i}} \mathrm{d}\boldsymbol{\xi}_1 \int_{S(\boldsymbol{x})} a^2 Y[n(\boldsymbol{x}-a\boldsymbol{K}/2,t)] \\ & \times f'(\boldsymbol{x}-a\boldsymbol{K},\boldsymbol{\xi}_1,t) f'(\boldsymbol{x},\boldsymbol{\xi},t) H(\boldsymbol{\xi}_{\rm r}\cdot\boldsymbol{K})(\boldsymbol{\xi}_{\rm r}\cdot\boldsymbol{K})\mathrm{d}^2\boldsymbol{K}, \end{aligned} \tag{2.50}$$

where $S(\boldsymbol{x})$ is the set of $\boldsymbol{K}$ for which a condition $\boldsymbol{x}-a\boldsymbol{K}\in\mathcal{D}$ holds. The substitution of f' expanded by the delta function (Eqs. (2.41) and (2.42)) into Eq. (2.50) yields

$$N_{\rm coll} = \frac{1}{2}\sum_{i}^{N_{\rm mol}} \sum_{m}^{N'_{\rm cell}} \sum_{j}^{N^{(m)}_{\rm mol}} [\mu^{(m)}_{(j)}]_{(i)}, \tag{2.51}$$

$$[\mu^{(m)}_{(j)}]_{(i)} = a^2 \frac{n^{(m)}}{N^{(m)}} \int_{S^{(m)}_{(i)}} Y[n(\boldsymbol{x}_{(i)}-a\boldsymbol{K}/2,t)] H(\boldsymbol{\xi}_{\rm r}\cdot\boldsymbol{K})(\boldsymbol{\xi}_{\rm r}\cdot\boldsymbol{K})\mathrm{d}^2\boldsymbol{K}, \tag{2.52}$$

where $N'_{\rm cell}$ ($m = 1, 2, ..., N'_{\rm cell}$) indicates the number of cells containing a position of the sphere radius a and center $\boldsymbol{x}_{(i)}$, $\boldsymbol{\xi}_{\rm r} = \boldsymbol{\xi}^{(m)}_{(j)} - \boldsymbol{\xi}_{(i)}$, and a term $(1/2)[\mu^{(m)}_{(j)}]_{(i)}$ gives the collision frequency between the jth molecule in the mth cell and the ith molecule to the total number of collisions per unit time. Hence, the probability of collisions

between the jth molecule in the mth cell and the ith molecule, $\bar{P}_{\rm coll}$ becomes

$$\bar{P}_{\rm coll} = \frac{1}{2}\frac{[\mu_{(j)}^{(m)}]_{(i)}}{N_{\rm coll}}, \tag{2.53}$$

Now, the probability of collisions $\bar{P}_{\rm coll}$ can be obtained from Eq. (2.53). However, in the actual algorithm, the estimation of $N_{\rm coll}$ from Eq. (2.52) is not practical because this estimation would require a huge computational cost that is proportional to $N_{\rm mol}^2$. Some stochastic techniques have been proposed [79–81] for calculating $N_{\rm coll}$. In this thesis, we utilize the *majorant frequency method* [81] according to the literature [43, 69].

In the majorant frequency method, we estimate the temporary collision number which is certainly larger than the actual number (Eq. (2.52)) and is easy to be calculated. We preliminarily consider the following inequality that $[\mu_{(j)}^{(m)}]_{(i)}$ in Eq. (2.52) satisfies.

$$[\mu_{(j)}^{(m)}]_{(i)} \leq [\bar{\mu}_{(j)}^{(m)}]_{(i)} = a^2 \frac{A_{(i)}C_{(i)}}{N_{\rm mol}^{(m)}} \int_{S_{(i)}^{(m)}} {\rm d}^2\boldsymbol{K}, \tag{2.54}$$

where $A_{(i)}$ and $C_{(i)}$ are constants which satisfy

$$A_{(i)} \geq n^{(m)} Y[n(\boldsymbol{x}_{(i)} - a\boldsymbol{K}/2, t)], \tag{2.55}$$

for all $\boldsymbol{K} \in S_{(i)}^{(m)}$ and m, and

$$C_{(i)} \geq |\boldsymbol{\xi}_{(j)}^{(m)} - \boldsymbol{\xi}_{(i)}|, \tag{2.56}$$

for all j and m. Here, we define a new quantity with the use of Eq. (2.54),

$$\bar{N}_{\rm coll} = \frac{1}{2}\sum_{i}^{N_{\rm mol}} \sum_{m}^{N'_{\rm cell}} \sum_{j}^{N_{\rm cell}^{(m)}} [\bar{\mu}_{(j)}^{(m)}]_{(i)}, \tag{2.57}$$

which is obtained by increasing $[\mu_{(j)}^{(m)}]_{(i)}$ in accordance with Eq. (2.54); $\bar{N}_{\mathrm{coll}}$ is greater than the actual collision number N_{coll}, but $\bar{N}_{\mathrm{coll}}$ can be easily estimated as shown below.

$$\begin{aligned}\bar{N}_{\mathrm{coll}} &= \frac{1}{2}\sum_{i}^{N_{\mathrm{mol}}}\sum_{m}^{N'_{\mathrm{cell}}} a^2 A_{(i)} C_{(i)} \int_{S_{(i)}^{(m)}} \mathrm{d}^2\boldsymbol{K}, \\ &= \frac{1}{2}\sum_{i}^{N_{\mathrm{mol}}} 4\pi a^2 A_{(i)} C_{(i)}. \end{aligned} \tag{2.58}$$

As stated above, $\bar{N}_{\mathrm{coll}}$ is greater than N_{coll}, but the probability of the actual collision is invariant because excessive candidates are rejected as false collisions. This is the essence of the majorant frequency method.

Let us explain how to determine the collision pair according to the majorant frequency method. The contribution of the ith molecule to $\bar{N}_{\mathrm{coll}}$ is $4\pi a^2 A_{(i)} C_{(i)}$; the actual or false collision are selected according to the following probability.

$$\bar{P}_{(i)} = \frac{2\pi a^2 A_{(i)} C_{(i)}}{\bar{N}_{\mathrm{coll}}}. \tag{2.59}$$

Once a molecule has been selected, the probability that it collides with the other molecules in the mth cell is obtained as

$$\bar{P}_{(i)}^{(m)} = \frac{1}{4\pi}\int_{S_{(i)}^{(m)}} \mathrm{d}^2\boldsymbol{K}. \tag{2.60}$$

The collision pair can be selected by drawing a random vector $\boldsymbol{K}$ on the unit sphere. The probability that the collision between the ith and jth molecules is selected as

the actual collision is determined from the following expression.

$$[\bar{P}_{(j)}^{(m)}]_{(i)} = \frac{[\mu_{(j)}^{(m)}]_{(i)}}{[\bar{\mu}_{(j)}^{(m)}]_{(i)}} = \frac{\displaystyle\int_{S_{(i)}^{(m)}} \varphi(\boldsymbol{K}) \mathrm{d}^2\boldsymbol{K}}{\displaystyle\int_{S_{(i)}^{(m)}} \mathrm{d}^2\boldsymbol{K}}, \tag{2.61}$$

$$\varphi(\boldsymbol{K}) = \frac{n^{(m)} Y[n(\boldsymbol{x}_{(i)} - a\boldsymbol{K}/2, t)] H(\boldsymbol{\xi}_\mathrm{r} \cdot \boldsymbol{K})(\boldsymbol{\xi}_\mathrm{r} \cdot \boldsymbol{K})}{A_{(i)} C_{(i)}}, \tag{2.62}$$

where $\varphi(\boldsymbol{K})$ holds $0 \leq \varphi(\boldsymbol{K}) \leq 1$. Eventually, the actual collision is accepted if the uniform random number r_u $(0 \leq r_\mathrm{u} \leq 1)$ is smaller than $\varphi(\boldsymbol{K})$, where $\boldsymbol{K}$ becomes random vector uniformly distributed on $S_{(i)}^{(m)}$. If a collision between the ith and jth molecules is accepted as the actual collision, the velocities of both molecules are changed according to Eq. (1.20):

$$\boldsymbol{\xi}'_{(i)} = \boldsymbol{\xi}_{(i)} + (\boldsymbol{K} \cdot \boldsymbol{\xi}_\mathrm{r})\boldsymbol{K}, \qquad \boldsymbol{\xi}'^{(m)}_{(j)} = \boldsymbol{\xi}^{(m)}_{(j)} - (\boldsymbol{K} \cdot \boldsymbol{\xi}_\mathrm{r})\boldsymbol{K}. \tag{2.63}$$

So far we have explained the concept of the procedure of the EV-DSMC simulation. To summarize the contents of this section, the flowchart of the EV-DSMC simulation in the steady system is as shown in Fig. 2.1. In the steady system, the macroscopic variables and the fluxes are calculated by the time average. In contrast, it is necessary to take an ensemble average in the unsteady system. The initial condition and the boundary condition are explained for each simulation so that the explanation is omitted here.

2.4 Test simulation for vapor–liquid equilibrium

As a test of the EV-DSMC simulation, we carry out the simulation for the vapor–liquid equilibrium state. Through this test simulation, we examine whether the EV-DSMC simulation is appropriate to investigate KBC, and then we calculate some quantities to be used as reference values in the later simulation.

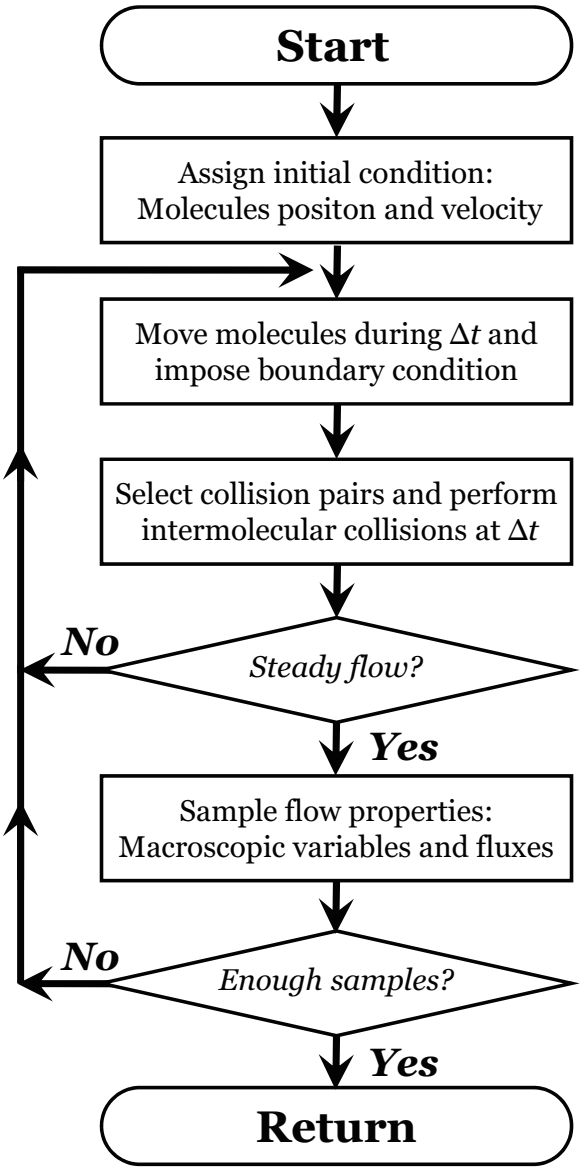

Figure 2.1: Flowchart of the EV-DSMC algorithm.

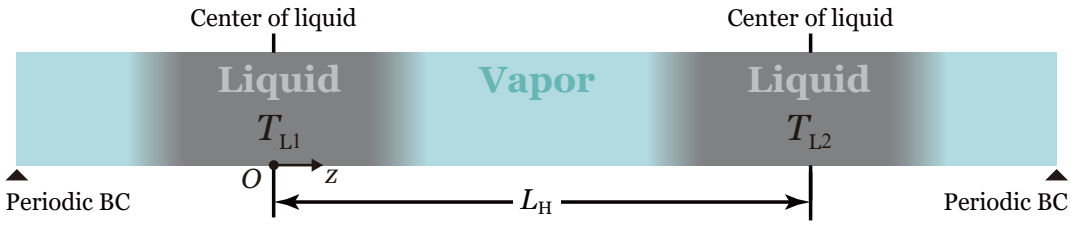

Figure 2.2: Schematic of the simulation system; T_{L1} and T_{L2} indicate the temperatures of two liquids ($T_{L1} = T_{L2} = T$) and L_H indicates the half-length of the simulation system.

2.4.1 Simulation settings

We simulate the system composed of vapor between two parallel liquid slabs (two-surface problem) in the one-dimensional space and the three-dimensional molecular velocity space. The schematic of the simulation system is shown in Fig. 2.2; T_{L1} and T_{L2} indicate the temperatures of two liquids and L_H indicates the half-length of the simulation system. The vapor–liquid equilibrium state is realized by keeping the temperature of two liquids at $T_{L1} = T_{L2} = T$. We simulate such an equilibrium (saturated) state in the range of the temperature, T/T_c, from 0.56 to 0.79 with the increments of 0.01. Note that $T/T_c = 0.56$ represents a temperature near the triple point if we refer to the critical temperature of argon. The cell size Δz is set to $0.2a$, the time step Δt is set to $0.001(\sqrt{2RT_c}/a) \approx 0.2\bar{\mu}_L^{-1}$, and the half-length of the simulation system L_H is set to $40a$. We calculate the macroscopic variables and the fluxes by taking 2,001 samples for each condition and averaging them over time.

Initial condition

In the EV-DSMC simulation, we give the positions and the velocities of molecules as an initial condition. In this simulation, 600,000 molecules (total 1,200,000 molecules) are arranged only around the center of each liquid where the liquid slab is to be formed.

The velocities of molecules are given by the following normalized velocity distri-

bution function.

$$\hat{f}_0 = \frac{1}{\sqrt{2\pi RT_{\mathrm{L}}}^3} \exp\left(-\frac{\xi_i^2}{2RT_{\mathrm{L}}}\right), \tag{2.64}$$

where T_0 is the reference temperature. Since the EV-DSMC simulation does not solve f, we cannot impose Eq. (2.64) directly. We give the velocities of molecules sampled from Eq. (2.64). This method is called the *random sampling*. Equation (2.64) is the normalized velocity distribution function, but from another point of view, it can be regarded as the probability density to find a certain molecular velocity ξ_i in the molecular velocity space $\mathrm{d}\boldsymbol{\xi}$. The probability density naturally satisfied the following relation.

$$\int_{\text{all } \xi_i} \hat{f}_0 \mathrm{d}\boldsymbol{\xi} = 1. \tag{2.65}$$

According to Eq. (2.65), the velocity of the x-component of the ith molecule $\xi_{x(i)}$ is obtained from the following indefinite integral.

$$\frac{1}{\sqrt{2\pi RT_{\mathrm{L}}}} \int_{-\infty}^{\xi_{x(i)}} \exp\left(-\frac{\xi_x^2}{2RT_{\mathrm{L}}}\right) \mathrm{d}\xi_x = r_{\mathrm{u}}, \tag{2.66}$$

where r_{u} is the uniform random number ($0 \leq r_{\mathrm{u}} \leq 1$). The above indefinite integral holds for $\xi_{y(i)}$ and $\xi_{z(i)}$ in the same way. Although we cannot solve this indefinite integral, each component of $\boldsymbol{\xi}_{(i)}$ can be found based on the Box–Muller method [82] as follows:

$$\xi_{z(i)} = \sqrt{-2RT_{\mathrm{L}} \ln r_{\mathrm{u}1}} \cos(2\pi r_{\mathrm{u}2}), \tag{2.67}$$

$$\xi_{x(i)} = \sqrt{-2RT_{\mathrm{L}} \ln r_{\mathrm{u}1}} \sin(2\pi r_{\mathrm{u}2}), \tag{2.68}$$

$$\xi_{y(i)} = \sqrt{-2RT_{\mathrm{L}} \ln r_{\mathrm{u}3}} \sin(2\pi r_{\mathrm{u}4}), \tag{2.69}$$

where $r_{\mathrm{u}1}$, $r_{\mathrm{u}2}$, $r_{\mathrm{u}3}$, and $r_{\mathrm{u}4}$ indicate the different uniform random numbers.

Boundary condition

Next, we describe the boundary condition in this simulation. As illustrated in Fig. 2.2, we impose the periodic boundary condition at both ends of the system; the molecules that flow out from one boundary after advection are inserted from the other boundary. By imposing this boundary condition, the simulation system as shown in Fig. 2.2 can be regarded as symmetric with respect to each center of liquid. In the following, we show the results only in half the simulation system.

Velocity scaling method

In this simulation, we apply the velocity scaling method [76] to keep the constant temperature. The velocity scaling method modifies the velocities of molecules at each time step according to the following equation.

$$\boldsymbol{\xi}(z, t + \frac{1}{2}\mathrm{d}t) = (2\Psi - 1)\boldsymbol{\xi}(z, t + \frac{1}{2}\mathrm{d}t) + \Psi F_z(z, t)\frac{\mathrm{d}t}{m}, \tag{2.70}$$

where Ψ is a temperature modification factor defined by the desired temperature T_d and current temperature T: $\Psi = \sqrt{T_\mathrm{d}/T}$. In this simulation, we calculate Φ in each cell at each time step.

This thermostat by the velocity scaling method is applied only near the center of each liquid. The region where the thermostat is imposed is determined based on the formula of the 10–90 thickness density transition layer,

$$\rho(z) = \frac{\rho_\mathrm{V} + \rho_\mathrm{L}}{2} + \frac{\rho_\mathrm{V} - \rho_\mathrm{L}}{2} \tanh\left(\frac{z - z_\mathrm{m}}{0.455\delta}\right), \tag{2.71}$$

where ρ_V and ρ_L indicate the vapor and liquid densities, respectively, z_m indicates the position of the center of the density transition layer, and δ is the thickness of the density transition layer. Equation (2.71) shows that the density distribution in the transition layer in vapor–liquid equilibrium can be described by the hyperbolic tangent. Applying the nonlinear least square method to the density distribution in

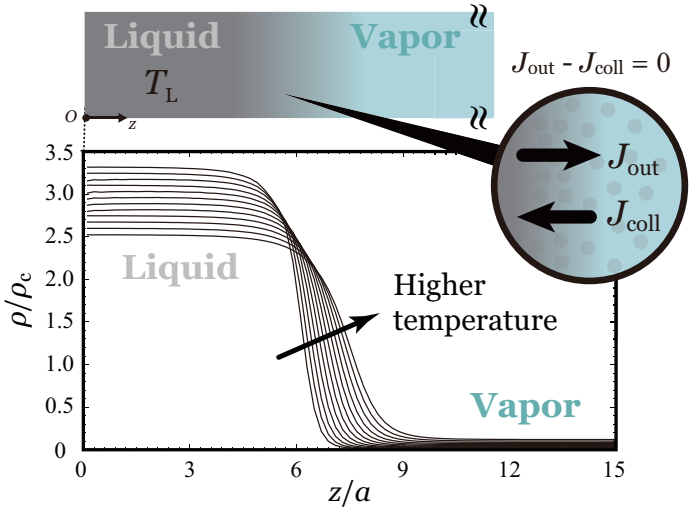

Figure 2.3: Spatial distribution of the density ρ obtained from the EV-DSMC simulation in vapor–liquid equilibrium in the cases of the normalized temperature, T/T_c, from 0.60 to 0.72; the abscissa is normalized by the molecular diameter a, and the ordinate is normalized by the critical density ρ_c.

the vapor-liquid equilibrium by using Eq. (2.71), we can get the values of z_m and δ. The region where the thermostat is imposed is defined as $3.0a$ from each z_m toward each liquid; the length of the thermostat region is approximately $\pm 3.0a$ from the center of liquid. Note that since the position of z_m depends on the temperature, the length of the thermostat region slightly varies with the temperature.

2.4.2 Results

Density

First, we show the results of the density fields to confirm whether the EV-DSMC simulation can qualitatively describe the vapor–liquid two-phase system. Figure 2.3 shows the density fields obtained from the EV-DSMC simulation in the region, z/a, from 0 to 15. In Fig. 2.3, the higher density region is liquid, and lower density region is vapor. The smooth density transition layer is formed between liquid and vapor. As can be seen in Fig. 2.3, when the temperature becomes higher, the liquid density becomes smaller, and the vapor density becomes larger; thus, the thickness of the density transition layer becomes thicker. This tendency corresponds to the results

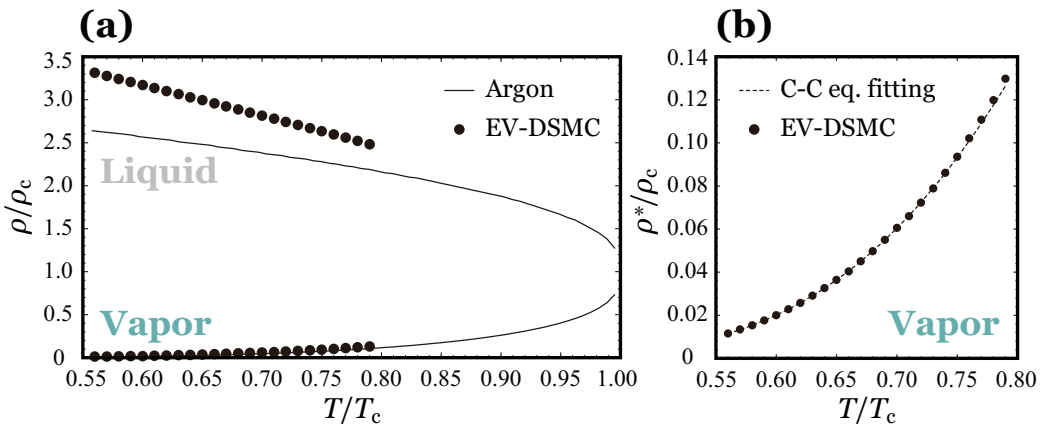

Figure 2.4: Temperature characteristics of the density ρ: (a) the vapor–liquid coexistence curve compared with argon [83]: (b) the Clausius-Clapeyron equation fitting for the vapor density; each abscissa is normalized by the critical temperature T_c, and each ordinate is normalized by the critical density ρ_c.

of the monatomic molecules [33, 83], such as argon and neon.

The enlarged view of Fig. 2.3 illustrates the mass flux relation at the vapor–liquid interface. In Fig. 2.3, $J_{\rm out}$ is the mass flux related to $f_{\rm out}$ ($J_{\rm out} = \int_{\xi_z>0} \xi_z f_{\rm out} {\rm d}\boldsymbol{\xi}$) and $J_{\rm coll}$ is that related to $f_{\rm coll}$ ($J_{\rm coll} = \int_{\xi_z<0} \xi_z f_{\rm coll} {\rm d}\boldsymbol{\xi}$). In vapor–liquid equilibrium, $J_{\rm out}$ should be balanced by $J_{\rm coll}$; hence, the mass flux at the vapor–liquid interface becomes zero.

Figure 2.4(a) shows the temperature characteristics of the density compared with argon summarized in the NIST Chemistry Web Book [83]. In Fig. 2.4(a), the solid lines denote the density of argon, the closed circles denote the density obtained from the EV-DSMC simulation. The vapor density obtained from the EV-DSMC simulation agrees with that of argon, while the liquid density obtained from the EV-DSMC simulation is larger than that of argon near the triple point temperature, where the maximum deviation is almost 20%. However, the temperature characteristics of the liquid and vapor densities are well described by the EV-DSMC simulation.

Clausius–Clapeyron equation

The Boltzmann equation is derived under the ideal gas condition ($na^3 \to 0$). The ideal gas condition is known to be applicable to monatomic molecules at the low temperature even for real molecules. Next, we examine whether the vapor density in vapor–liquid equilibrium obtained by the EV–DSMC simulation satisfies the ideal gas condition.

The relation between the pressure and the temperature of the ideal gas in vapor–liquid equilibrium is given as follows:

$$\frac{\mathrm{d}p}{\mathrm{d}T} = \frac{\Delta h}{RT^2}, \tag{2.72}$$

where Δh is the latent heat, and it can be assumed constant in the case of the ideal gas. Solving this differential equation,

$$\int_{p_0}^{p} \frac{1}{p}\mathrm{d}p = \frac{\Delta h}{R}\int_{T_0}^{T} \frac{1}{T^2}\mathrm{d}T, \tag{2.73}$$

we get

$$\begin{aligned} p &= p_0 \exp\left(\frac{\Delta h}{RT_0}\right)\exp\left(-\frac{\Delta h}{RT_0}\right) \\ &= p_0' \exp\left(-\frac{\Delta h}{RT_0}\right), \end{aligned} \tag{2.74}$$

where T_0, p_0, and p_0' are the constants. Equation (2.74) is called the Clausius–Clapeyron equation. Note that T_0 and p_0 can be regarded as the temperature and the pressure near the triple point because we consider the vapor–liquid coexistence region. Then, we derive the relation between the vapor density and the temperature in vapor–liquid equilibrium. Substituting the equation of state for the ideal gas

($p = \rho RT$) into Eq. (2.74), we get

$$\rho = \frac{p_0'}{RT} \exp\left(-\frac{\Delta h}{RT}\right). \tag{2.75}$$

Equation (2.75) is also called the Clausius–Clapeyron equation. In this study, we call Eq. (2.75) the Clausius–Clapeyron equation. For convenience, we normalize Eq. (2.75) by critical density ρ_c and the critical temperature T_c:

$$\frac{\rho}{\rho_c} = \frac{p_0'}{RT_c}\frac{T_c}{T} \exp\left(-\frac{\Delta h}{RT_c}\frac{T_c}{T}\right). \tag{2.76}$$

Figure 2.4(b) shows the vapor density obtained from the EV-DSMC simulation; the dashed line in Fig. 2.4(b) denotes the Clausius–Clapeyron equation obtained by the nonlinear least square method with the use of Eq. (2.76). Two normalized constants in Eq. (2.76), which are related to the pressure and the latent heat, are obtained from this fitting as $p_0'/RT_c = 79.72$ and $\Delta h/RT_c = 5.279$, respectively. As can be seen in Fig 2.4, the vapor density obtained by the EV-DSMC simulation is well fitted by the Clausius–Clapeyron equation (Eq. (2.76)) in all the temperature cases. Frezzotti *et al.* [43] also showed the similar result from the EV-DSMC simulation that the vapor density is well fitted by the Clausius–Clapeyron equation in the low temperature range ($T/T_c \lesssim 0.80$) with $\Delta h/RT_c = 5.3776$. We now conclude that vapor can be regarded as the ideal gas in the range of the temperature, T/T_c, from 0.56 to 0.79.

Velocity distribution function

To confirm the equilibrium solution of the Enskog–Vlasov equation, we examine the velocity distribution function obtained from the EV-DSMC simulation. Figure 2.5 shows the velocity distribution functions normalized by the density at the positions $z/a = 0.1$ (liquid) and $z/a = 19.9$ (vapor) in the cases of the temperature, T/T_c, 0.56 and 0.79. In Fig. 2.5, the solid lines denote the normalized Maxwellian distribution

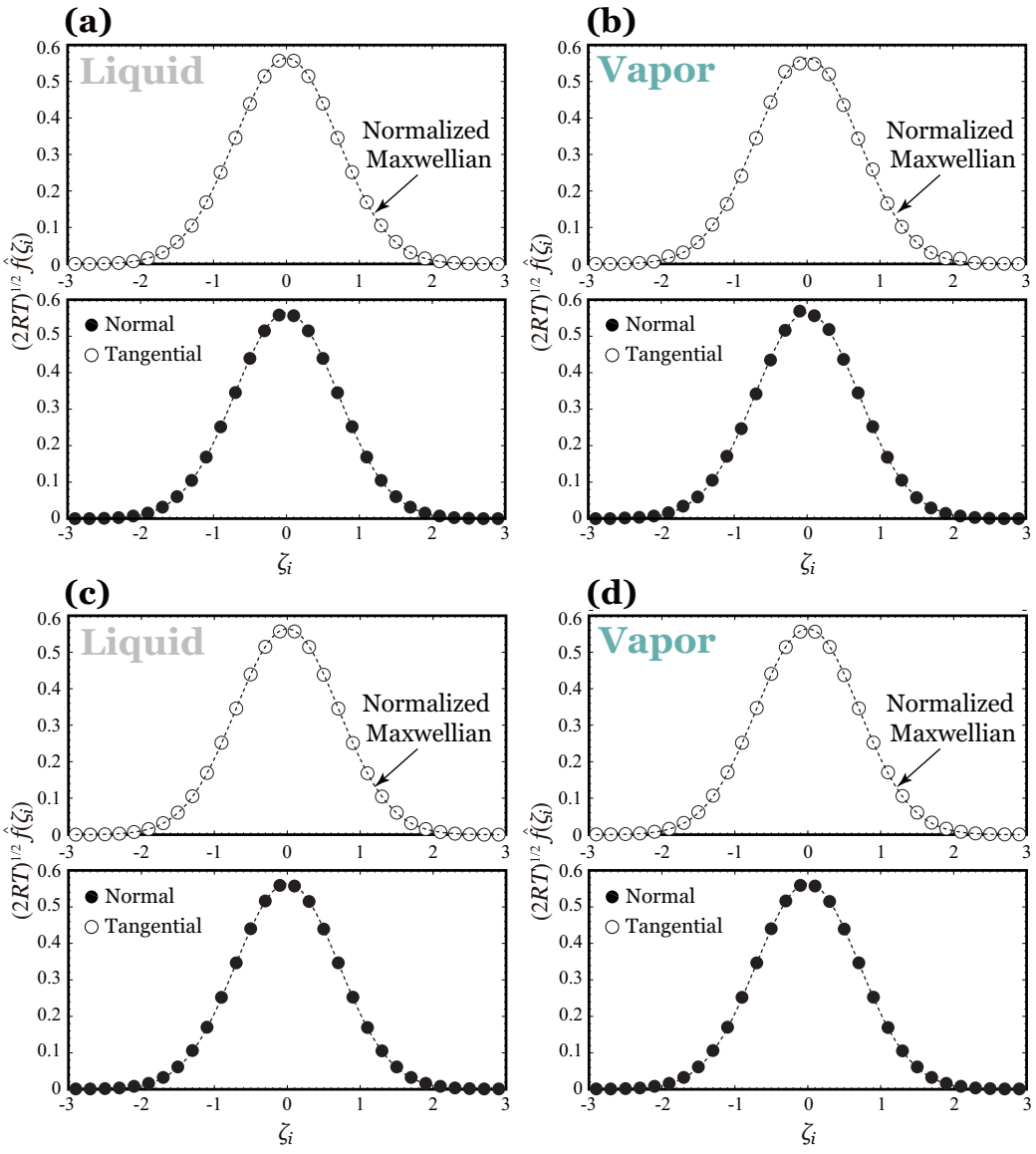

Figure 2.5: Velocity distribution function in the cases of (a) $T/T_c = 0.56$ and $z/a = 0.1a$, (b) $T/T_c = 0.56$ and $z/a = 19.9$, (c) $T/T_c = 0.79$ and $z/a = 0.1$, and (d) $T/c = 0.79$ and $z/a = 19.9$.

modified as

$$\sqrt{2RT}\hat{f}^*(\zeta_i) = \frac{1}{\sqrt{\pi}}\exp(-\zeta_i^2), \tag{2.77}$$

where $\zeta_i = \xi_i/\sqrt{2RT}$. The closed circles are the normalized velocity distribution function obtained from the EV-DSMC simulation. In the EV-DSMC simulation, the normalized velocity distribution function is obtained by the following procedure. We set the upper and lower limits of the velocity space to $\zeta_i = -3$ and $\zeta_i = 3$, respectively, and divide this velocity space into 30 cells. We can calculate the normalized velocity distribution function at each cell of the physical space in the simulation system by determining which cells molecular velocity belongs to and counting the number of molecules.

As can be seen in Fig. 2.5, the normalized velocity distribution function at each point and temperature agrees with the solid lines (Eq. (2.77)). In vapor at the low temperature, the data obtained from the EV-DSMC simulation vary around the normalized Maxwellian distribution because the number of molecules is smaller than that in the high temperature case (see Fig. 2.4(b)). That is why it is hard to obtain enough samples in vapor at the low temperature. It is an important result that the normalized velocity distribution function becomes the normalized Maxwellian distribution and the vapor density obeys the Clausius–Clapeyron equation for the ideal gas; thus, we conclude that the equilibrium solution of the Enskog–Vlasov equation in vapor is the same as that of the Boltzmann equation and it can be obtained from the EV-DSMC simulation.

Mean free path

Hereafter, we calculate two quantities to be used as reference values in the later simulation, namely, the mean free path and the thermal conductivity. Once the density is obtained from the EV-DSMC simulation, we can determine the mean free path ℓ from Eq. (2.21). We preliminarily estimate $Y(n)$ from Eq. (2.30) in the

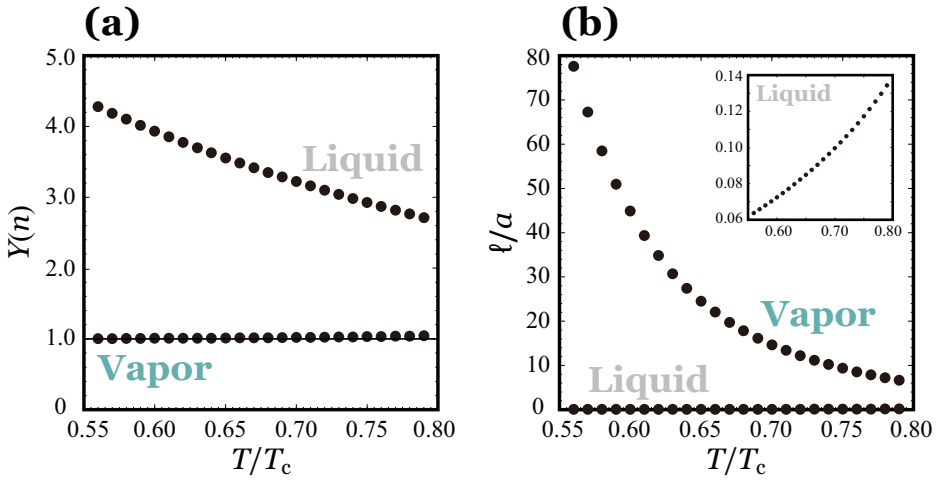

Figure 2.6: Temperature characteristics of (a) the pair correlation function $Y(n)$ and (b) the mean free path ℓ; each abscissa is normalized by the critical temperature T_c, and the ordinate of (b) is normalized by the molecular diameter a.

range of the temperature, T/T_c, from 0.56 to 0.79. Figure 2.6(a) shows the relation between $Y(n)$ obtained from the EV-DSMC simulation and the temperature T. As can be seen, $Y(n)$ in liquid becomes smaller with the increase of the temperature, while $Y(n)$ in vapor is almost constant and is equal to unity. In the case of $Y(n) = 1$ (the solid line in Fig. 2.6(a)), the mean free path of the Enskog–Vlasov equation (Eq. (2.21)) is equivalent to that of the Boltzmann equation (Eq. (1.30)). This result indicates that the mean free path of vapor is to be the same as that of the Boltzmann equation in the range of the temperature, T/T_c, from 0.56 to 0.79.

We then estimate the mean free path ℓ defined in Eq. (2.21). Figure 2.6(b) shows the relation between the mean free path ℓ and the temperature T. The mean free path in vapor is larger than that in liquid and decreases with the increase in the temperature, while that in liquid (see the enlarged view of Fig. 2.6(b)) increases with the increase in the temperature.

Thermal conductivity

We now estimate the thermal conductivity λ_E as one of the characteristic transport properties. As already shown, λ_E is obtained from Eq. (2.24) by using λ_B

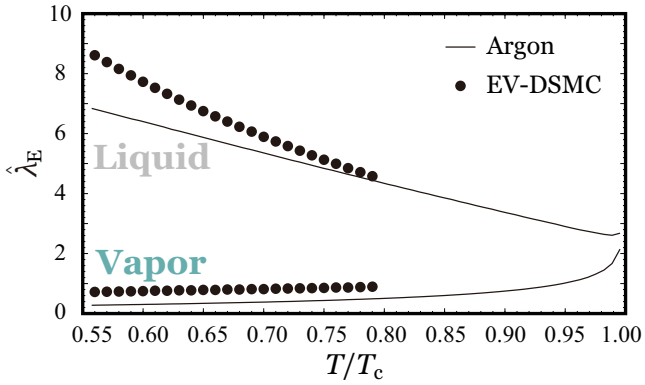

Figure 2.7: Temperature characteristics of the normalized thermal conductivity $\hat{\lambda}_E$ (Eq. (2.78)) compared with argon [83]; the abscissa is normalized by the critical temperature T_c.

(Eq. (2.22)); λ_E normalized by the critical density ρ_c, the critical temperature T_c, and the molecular diameter a is

$$\begin{aligned}\hat{\lambda}_E &= \frac{\lambda_E T_c}{a\rho_c\sqrt{2RT_c^3}} \\ &= \frac{75}{128\sqrt{2\pi}}\frac{1}{Y(n)}\left[1+\frac{5}{6}(nbY(n))+\left(\frac{9}{25}+\frac{32}{25\pi}\right)(nbY(n))^2\right]\frac{\rho}{\rho_c}\sqrt{\frac{T}{T_c}}. \end{aligned} \quad (2.78)$$

Figure 2.7 shows the relation between the normalized thermal conductivity $\hat{\lambda}_E$ and the temperature T. In Fig. 2.7, the closed circles denote $\hat{\lambda}_E$ obtained from the EV-DSMC simulation, and the solid lines denote that of argon summarized in the NIST Chemistry Web Book, which is normalized by the critical values [83] and Lennard-Jones intermolecular potential parameters [72]. As can be seen in Fig. 2.7, although the slope of the thermal conductivity in liquid obtained from the EV-DSMC simulation is larger than that of argon, the temperature characteristics of thermal conductivity obtained from the EV-DSMC simulation in both liquid and vapor show good agreement with those of argon. Also, this result is consistent with that reported by Karkheck and Stell [72].

Chapter

3

Construction of kinetic boundary condition

In this chapter, we examine the mass flux relation (Eq. (2.3)) to find a pair of α_{e} and α_{c} defined by Eq. (1.42) by the EV-DSMC simulation explained in Chapter 2. We perform the EV-DSMC simulation for the two-surface problem in 160 cases of the temperature differences between two liquids. First, we confirm whether the normalized velocity distribution function of the KBC obeys Eq. (2.2) because the results of the previous studies [34, 38, 39, 41] indicated that the normalized velocity distribution function of the KBC deviates from Eq. (2.2) under strong net evaporation/condensation. Next, we formulate the mass flux relation at each liquid temperature by using ρv_z obtained by the molecular simulation and corresponding σ (Eq. (2.4)), and then we discuss α_{e} and α_{c} defined by Eq. (1.42) by comparing the formulated mass flux relation with Eq. (2.3). In this way, we can find a pair of α_{e} and α_{c} without explicitly defining the molecular processes illustrated in Fig. 1.1.

3.1 Simulation settings

As explained in Chapter 2 (Section 2.1.2), we simulate the system composed of vapor between two parallel liquid slabs (two-surface problem) in the one-dimensional space and the three-dimensional molecular velocity space. The schematic of the simulation system is shown in Fig. 3.1; T_{L1} and T_{L2} indicate the temperatures of two liquids ($T_{\mathrm{L1}} > T_{\mathrm{L2}}$), L_{H} indicates the half-length of the simulation system, and L_{V} indicates

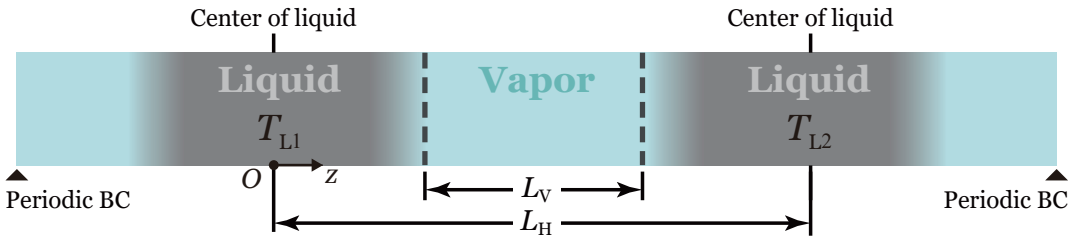

Figure 3.1: Schematic of the simulation system; T_{L1} and T_{L2} indicate the temperatures of two liquids ($T_{L1} > T_{L2}$), L_H indicates the half-length of the simulation system, and L_V indicates the length of the vapor phase.

the length of the vapor phase. As a consequence of the temperature difference between two liquids, net evaporation occurs at the vapor–liquid interface on the high-temperature side, and net condensation occurs at the vapor–liquid interface on the low-temperature side.

We simulate the various cases of net evaporation and condensation by varying the temperature difference between two liquids; one of the liquid temperatures is fixed as a reference, and the other is varied. Seven cases of the reference liquid temperature, T_L/T_c, are set to 0.60, 0.62, 0.64, 0.66, 0.68, 0.70, and 0.72. For example, in the case of $T_L/T_c = 0.60$, T_{L2}/T_c is varied in the range of 0.56 to 0.59 with the increments of 0.01 with T_{L1}/T_c fixed to 0.60 (net evaporation cases), while T_{L1}/T_c is varied in the range of 0.61 to 0.76 with increments 0.01 with T_{L2}/T_c fixed to 0.60 (net condensation cases). In this manner, we perform the simulations under 160 cases of the temperature differences. All cases of the temperature differences are summarized in Tables 3.1–3.7. The cell size Δz is set to $0.2a$, the time step Δt is set to $0.001(\sqrt{2RT_c}/a) \approx 0.2\bar{\mu}_L^{-1}$, and the half-length of the simulation system L_H is set to $40a$. We calculate the macroscopic variables and the fluxes by taking 2,001 samples for each condition and averaging them over time.

3.1.1 Initial condition

We give the initial condition in the same way as in Chapter 2 (Section 2.4.1). In this simulation, 600,000 molecules (total 1,200,000 molecules) are arranged only around

the center of each liquid where the liquid slab is to be formed. The velocities of molecules are determined by using the random sampling as

$$\xi_{z(i)} = \sqrt{-2RT_{\mathrm{L1}} \ln r_{\mathrm{u1}}} \cos(2\pi r_{\mathrm{u2}}), \tag{3.1}$$

$$\xi_{x(i)} = \sqrt{-2RT_{\mathrm{L1}} \ln r_{\mathrm{u1}}} \sin(2\pi r_{\mathrm{u2}}), \tag{3.2}$$

$$\xi_{y(i)} = \sqrt{-2RT_{\mathrm{L1}} \ln r_{\mathrm{u3}}} \sin(2\pi r_{\mathrm{u4}}), \tag{3.3}$$

for the left liquid slab and

$$\xi_{z(i)} = \sqrt{-2RT_{\mathrm{L2}} \ln r_{\mathrm{u5}}} \cos(2\pi r_{\mathrm{u6}}), \tag{3.4}$$

$$\xi_{x(i)} = \sqrt{-2RT_{\mathrm{L2}} \ln r_{\mathrm{u5}}} \sin(2\pi r_{\mathrm{u6}}), \tag{3.5}$$

$$\xi_{y(i)} = \sqrt{-2RT_{\mathrm{L2}} \ln r_{\mathrm{u7}}} \sin(2\pi r_{\mathrm{u8}}), \tag{3.6}$$

for the right liquid slab, where r_{u1}–r_{u8} indicate the different uniform random numbers.

3.1.2 Boundary condition

We give the boundary condition in the same way as in Chapter 2 (Section 2.4.1). As illustrated in Fig. 3.1, we impose the periodic boundary condition at both ends of the system; the molecules that flow out from one boundary after advection are inserted from the other boundary. By imposing this boundary condition, the simulation system as shown in Fig. 3.1 can be regarded as symmetric with respect to each center of liquid. In the following, we show the results only in half the simulation system.

3.1.3 Other settings

Velocity scaling method

We impose the thermostat in the same way as in Chapter 2 (Section 2.4.1). We apply the velocity scaling method [76] to keep the constant temperature. The temperature modification factor Φ in Eq. (2.70) is estimated in each cell at each time step. The region where the thermostat is imposed is defined as $3.0a$ from each z_{m} toward each liquid, where z_{m} indicates the position of the center of the 10–90 thickness density transition layer in vapor–liquid equilibrium (Eq. (2.71)); the length of the thermostat region is approximately $\pm 3.0a$ from the center of liquid. Note that since the position of z_{m} depends on the temperature, the length of the thermostat region slightly varies with the temperature.

Particle shifting method

To obtain the steady net evaporation/condensation system, we apply the particle shifting method [46]. The particle shifting method modifies the positions of molecules in whole simulation system at each time step, fixing the position of each vapor–liquid interface.

In half the simulation system whose length is L_{H} as shown in Fig. 3.1, the number of molecules that move from the left- to right-hand sides becomes larger due to net evaporation and condensation. First, we define the difference between the number of molecules in the right- and left-hand sides of one-quarter of the simulation system as N_{shift}. Next, all molecules are shifted according to a distance $\Delta z_{\mathrm{shift}}$ toward the right-hand side; $\Delta z_{\mathrm{shift}}$ is determined from

$$\frac{N_{\mathrm{shift}}}{2} = n(T_{\mathrm{L1}}) U_{xy} \Delta z_{\mathrm{shift}}, \tag{3.7}$$

where U_{xy} is the unit area of the cross-section and $n(T_{\mathrm{L1}})$ is the number density of liquid at T_{L1}. Finally, molecules that go out of the simulation system by shifting

are inserted on the left-hand side liquid at T_{L1}. The simulation system shown in Fig. 2.2 reaches steady net evaporation/condensation by both the velocity scaling and particle shifting methods.

Positions of vapor–liquid interface

Although in the macroscopic point of view, the vapor–liquid interface can be regarded as zero thickness and its position can be uniquely determined, in the microscopic point of view, it is difficult to determine the position of the vapor–liquid interface uniquely. As illustrated in Fig. 1.1, we refer to the boundary between the interface layer and the Knudsen layer as the vapor–liquid interface in the microscopic point of view. Since this vapor–liquid interface is equivalent to the boundary at which the KBC is imposed in the molecular gas dynamics analysis, it has to satisfy the ideal gas condition, which is a premise of the Boltzmann equation. Note that the position of such a vapor–liquid interface is located on the vapor side compared to that determined by the Gibbs dividing surface.

We determine the ideal gas region where the density of vapor–liquid equilibrium obeys the Clausius–Clapeyron equation and define the end of the ideal gas region as the vapor–liquid interface. In this simulation, the position of the vapor–liquid interface is set to the position distanced 2.5δ from z_{m} to vapor, where δ is determined by the density distribution in vapor–liquid equilibrium. In this simulation, we examine the mass flux and the velocity distribution function at this position of the vapor–liquid interface. Furthermore, L_{V} in Fig. 3.1 indicates the length between the two vapor–liquid interfaces. Since z_{m} and δ depend on the liquid temperature, L_{V} is different in each condition of the liquid temperature difference as summarized in Tables 3.1–3.7.

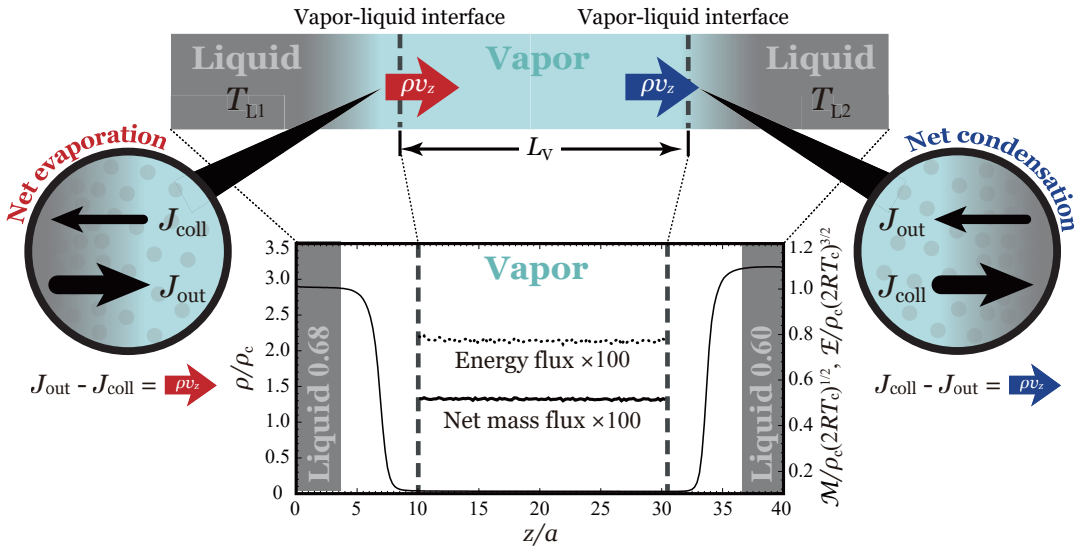

Figure 3.2: (upper part) Schematic of half the simulation system and the mass flux relations at each vapor–liquid interface. (lower part) Spatial distributions of the density ρ, the mass flux $\mathcal{M}$ in vapor, and the energy flux $\mathcal{E}$ in vapor obtained from the EV-DSMC simulation at $T_{L1}/T_c = 0.68$ and $T_{L2}/T_c = 0.60$; the abscissa is normalized by the molecular diameter a, and the ordinates are normalized by the critical values.

3.2 Results and discussion

3.2.1 Macroscopic variables and fluxes

We preliminarily show the results of the macroscopic variables and the fluxes obtained from the EV-DSMC simulation. The upper part of Fig. 3.2 shows the schematic of half the simulation system. Two liquids at T_{L1} and T_{L2} ($T_{L1} > T_{L2}$) are confined to the regions around the left and right edges of half the simulation system, respectively. In Fig. 3.2, the bold dashed lines denote the vapor–liquid interface. As illustrated in the enlarged view of Fig. 3.2, ρv_z is obtained as the difference between J_{out} and J_{coll}. The red and blue arrows in Fig. 3.2 denote the directions of ρv_z; as a consequence of the temperature difference between two liquids, ρv_z at the left interface is induced in the direction outgoing from liquid (net evaporation), and that at the right interface is induced in the direction colliding onto liquid (net condensation).

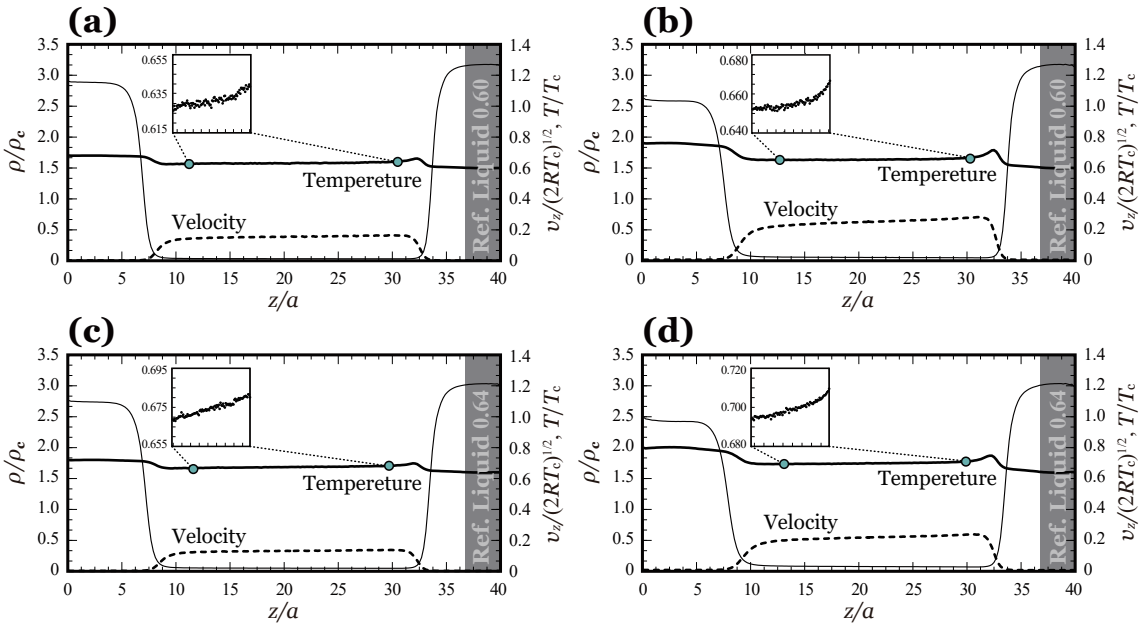

Figure 3.3: Spatial distributions of the density ρ, the velocity v_z, and the temperature T obtained from the EV-DSMC simulation in the cases of (a) $T_{\rm L1}/T_{\rm c} = 0.68$ and $T_{\rm L2}/T_{\rm c} = 0.60$, (b) $T_{\rm L1}/T_{\rm c} = 0.76$ and $T_{\rm L2}/T_{\rm c} = 0.60$, (c) $T_{\rm L1}/T_{\rm c} = 0.72$ and $T_{\rm L1}/T_{\rm c} = 0.64$, and (d) $T_{\rm L1}/T_{\rm c} = 0.80$ and $T_{\rm L2}/T_{\rm c} = 0.64$; the abscissa is normalized by the molecular diameter a, and the ordinates are normalized by the critical values.

The lower part of Fig. 3.2 shows the density field and the mass and energy fluxes in vapor in the case of $T_{\rm L1}/T_{\rm c} = 0.68$ and $T_{\rm L2}/T_{\rm c} = 0.60$ obtained from the EV-DSMC simulation; the thin solid line denotes the density field, the bold solid line denotes the mass flux in vapor, and the dashed line denotes the energy flux in vapor. Note that since we can assume that the effects of the collisional transfer and the potential contribution are negligible in vapor, we calculate the energy flux from Eq. (1.16). As shown in Fig. 3.2, the mass and energy fluxes in vapor take positive values in the z-direction, and the mass flux is uniform and constant in vapor because of steady net evaporation and condensation. We confirmed that this uniform and constant mass flux in vapor is observed in other cases of liquid temperature [48].

Figure 3.3 shows the density, velocity, and temperature fields obtained from the EV-DSMC simulation in the cases of the reference liquid temperature, $T_{\rm L}/T_{\rm c}$, 0.60 and 0.64; the thin solid lines denote the density fields, the bold solid lines denote the temperature fields, and dashed lines denote the velocity fields. Typical examples

of weak net condensation (Figs. 3.3(a) and (c)) with the small liquid temperature difference and strong net condensation (Figs. 3.3(b) and (d)) with the large liquid temperature difference are presented. As can be seen in Fig. 3.3, a positive vapor velocity in the z-direction is induced by net evaporation/condensation, and this vapor velocity increases with the increase in the liquid temperature difference in all cases. In Figs. 3.3(b) and (d), we can see a peak in the temperature near the reference liquid. This peak in temperature is also observed by the molecular dynamics simulation [41] in the case of strong net condensation. Also, we can see that the temperature at the vapor–liquid interface differs from that of liquid, which is called *temperature jump* [20, 27, 29, 34, 36, 84, 85]. The temperature jump increases with the increase in the liquid temperature difference in the both cases of the reference liquid temperature; this increase in the temperature jump is related to the increase in the velocity in the direction normal to the vapor–liquid interface [23].

As already mentioned in Chapter 2 (Section 2.1.2), in the two-surface problem, a well-known characteristic phenomenon the *inverted temperature gradient* [24, 54–56] occurs in vapor as a consequence of the temperature jump. As can be seen in the enlarged views of Fig. 3.3, the temperature gradient at the center of vapor becomes positive in all cases. From this result, we can verify the occurrence of the inverted temperature gradient by the EV-DSMC simulation. Several studies [86–88] have indicated that the inverted temperature gradient also causes the negative mass flow. We, however, could not observe the negative mass flow in this simulation because the occurrence of this phenomenon is highly unlikely indicated by the necessary and sufficient criteria [87, 88].

3.2.2 Normalized velocity distribution function of kinetic boundary condition

In the following, we show the main results of this chapter. First, we confirm whether the normalized velocity distribution function of the KBC obeys the normalized

Maxwellian distribution Eq. (2.2). This assumption is the basis of the definitions of α_{e} and α_{c} (Eq. (1.42)). Several studies [34, 38, 39, 41] have pointed out that the normalized velocity distribution function of the KBC deviates from the normalized Maxwellian distribution at the liquid temperature $\hat{f}^*$ (Eq. (2.2)) in the case of strong net condensation. For example, Ishiyama *et al.* [34, 38] and Kobayashi *et al.* [39] proposed the following expression for the normalized velocity distribution function of the KBC by the molecular simulation:

$$\hat{f} = \frac{1}{\sqrt{2\pi RT_{\mathrm{n}}}(2\pi RT_{\mathrm{t}})} \exp\left(-\frac{\xi_x^2 + \xi_y^2}{2RT_{\mathrm{t}}} - \frac{\xi_z^2}{2RT_{\mathrm{n}}}\right), \tag{3.8}$$

where T_{n} indicates the normal temperature composed of molecules having velocity $\xi_z > 0$ at the vapor–liquid interface ($T_{\mathrm{n}} \approx T_{\mathrm{L}}$), and T_{t} indicate the tangential temperature composed of molecules having the velocity $\xi_z > 0$ at the vapor–liquid interface; according to Ishiyama *et al.* [38], T_{t} is formulated by using the thermal accommodation coefficient. Hereafter, Eq. (3.8) is referred to as the anisotropic Maxwellian distribution.

If the normalized velocity distribution function of the KBC depends on f_{coll}, we cannot express the KBC by utilizing the linear scattering kernel K_{I} (Eq. (1.34)) as explained in Chapter 1 (Section 1.2.3). We can certainly define a nonlinear scattering kernel because we know the functional form of the normalized velocity distribution function of the KBC as in Eq. (3.8), but it is mathematically complex to be analyzed and has never been precisely investigated. For that reason, we assume the normalized Maxwellian distribution for the normalized velocity distribution function of the KBC. However, it is important to examine how the normalized Maxwellian distribution grades into anisotropic and how the anisotropic Maxwellian distribution affects to the solution of the Boltzmann equation.

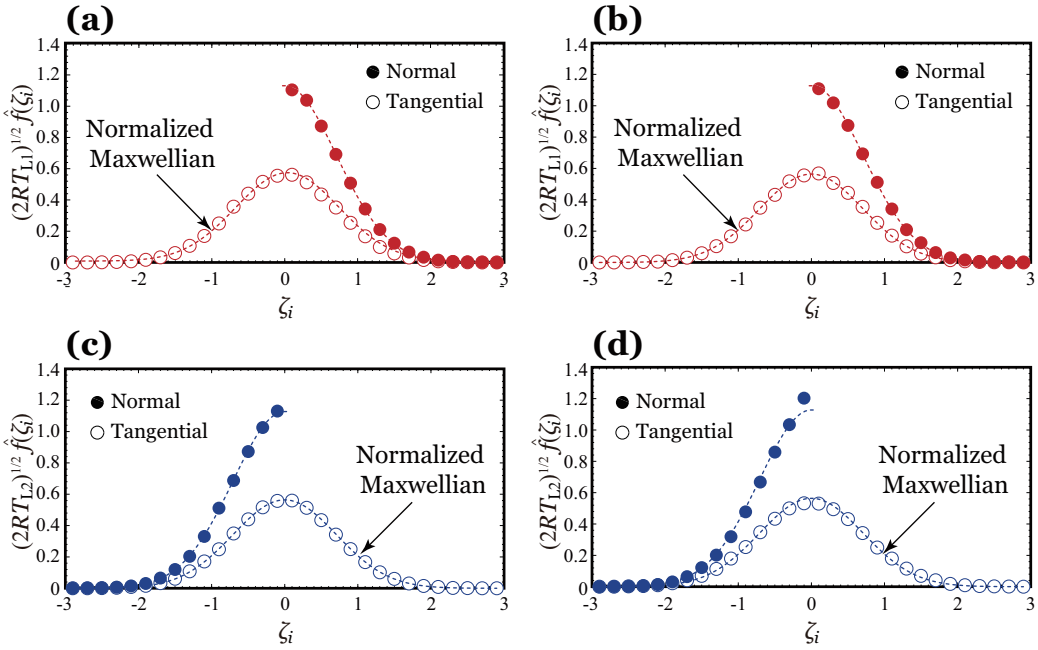

Figure 3.4: Normalized velocity distribution function of the KBC at the vapor–liquid interface of the reference liquid at $T_{\mathrm{L}}/T_{\mathrm{c}} = 0.60$ obtained from the EV-DSMC simulation in the cases of (a) $T_{\mathrm{L1}}/T_{\mathrm{c}} = 0.60$ and $T_{\mathrm{L2}}/T_{\mathrm{c}} = 0.56$ (net evaporation), (b) $T_{\mathrm{L1}}/T_{\mathrm{c}} = 0.60$ and $T_{\mathrm{L2}}/T_{\mathrm{c}} = 0.59$ (net evaporation), (c) $T_{\mathrm{L1}}/T_{\mathrm{c}} = 0.68$ and $T_{\mathrm{L2}}/T_{\mathrm{c}} = 0.60$ (net condensation), and (d) $T_{\mathrm{L1}}/T_{\mathrm{c}} = 0.76$ and $T_{\mathrm{L2}}/T_{\mathrm{c}} = 0.76$ (net condensation).

Estimation of temperature in kinetic boundary condition

Here, we obtain the normalized velocity distribution function at the vapor–liquid interface of the reference liquid composed of the outgoing molecules from there, that is, the normalized velocity distribution function of the KBC. The calculation procedure of the normalized velocity distribution function is the same as in Chapter 2 (Section 2.4.2). We set the upper and lower limits of the velocity space to $\zeta_i = -3$ and $\zeta_i = 3$, respectively, and divide this velocity space into 30 cells, where $\zeta_i = \xi_i/\sqrt{2RT_{\mathrm{L1}}}$ or $\zeta_i = \xi_i/\sqrt{2RT_{\mathrm{L2}}}$. Figure 3.4 shows the normalized velocity distribution function of the KBC at the vapor–liquid interface of the reference liquid at $T_{\mathrm{L}}/T_{\mathrm{c}} = 0.60$. In Fig. 3.4, the closed circles denote the normalized velocity distribution function in the direction normal to the vapor–liquid interface ($i = \mathrm{n}$), the open circles denote that in the tangential direction ($i = \mathrm{t}$), and the dashed

lines denote the normalized Maxwellian distribution function (Eq. (2.77)). In the present system (Fig. 3.1), the normalized velocity distribution function of the KBC is composed of molecules having the velocity $\xi_z > 0$ in the net evaporation cases (Figs. 3.4(a) and (b)), while that is composed of molecules having the velocity $\xi_z < 0$ in the net condensation cases (Figs. 3.4(c) and (d)).

As can be seen in Fig. 3.4, the normalized velocity distribution functions of the KBC agree with the normalized Maxwellian distribution (Eq. (2.77)) in the cases of net evaporation and weak net condensation (Figs. 3.4(a), (b), and (d)). On the other hand, those deviate from the normalized Maxwellian distribution and becomes anisotropic in the case of strong net condensation (Fig. 3.4(d)). Furthermore, in the case of strong net condensation (Fig. 3.4(d)), we can see that the normalized velocity distribution function of the KBC in the direction normal to the vapor–liquid interface deviates prominently in the vicinity of $\zeta_\mathrm{n} = 0$. This functional form differs from the Maxwellian type distribution anymore, but it is referred to as the anisotropic Maxwellian distribution here for convenience. These tendencies are similar to the results of the previous study [41].

To investigate the normalized velocity distribution function of the KBC, we estimate the normal temperature T_n and the tangential temperature T_t. These temperatures in the KBC are defined by

$$T_i = \frac{1}{\rho_\mathrm{out} R} \int_{\xi_z > 0} \xi_i^2 f_\mathrm{out} \mathrm{d}\boldsymbol{\xi}, \tag{3.9}$$

where i indicates the component in the direction normal or tangential to the vapor–liquid interface ($i = \mathrm{n}$ or t) and $\rho_\mathrm{out} = \int_{\xi_z > 0} f_\mathrm{out} \mathrm{d}\boldsymbol{\xi}$. In the present system (Fig. 3.1), the domain of the integration of Eq. (3.9) becomes $\xi_z < 0$ in the case of net condensation because the KBC at the vapor–liquid interface with net condensation is composed of molecules having the velocity $\xi_z < 0$. For example, in the case of strong net condensation (Fig. 3.4(d)), $T_\mathrm{n}/T_\mathrm{c}$ and $T_\mathrm{t}/T_\mathrm{c}$ estimated from Eq. (3.9) become 0.582 and 0.657, respectively, in which case the normalized velocity distri-

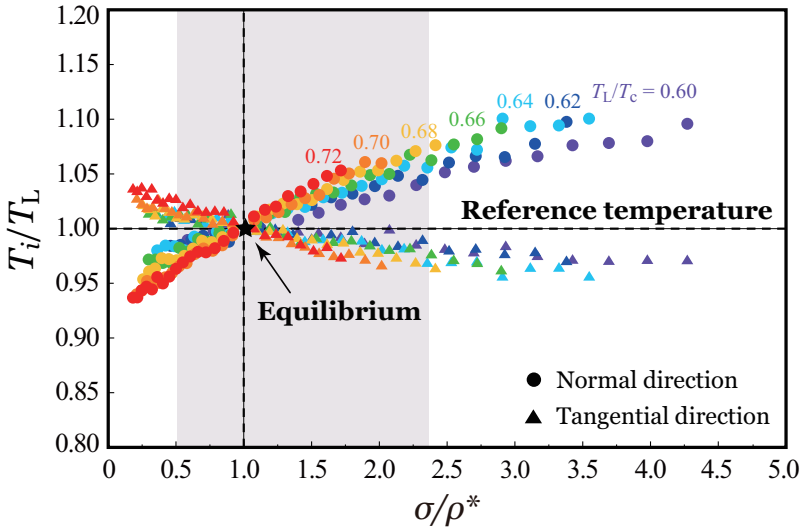

Figure 3.5: Relation between the normal temperature T_n and the tangential temperature T_t in the KBC and the degree of net evaporation/condensation at the vapor–liquid interface in all 160 cases of the liquid temperature differences; the abscissa represents the index of the degree of net evaporation/condensation σ/ρ^*, and the ordinate is normalized by the reference liquid temperature T_L.

bution function of the KBC becomes the anisotropic Maxwellian distribution. This tendency of the temperatures in the KBC is similar to those reported in the previous studies [34, 38, 39, 41].

Figure 3.5 shows the normal temperature T_n and the tangential temperature T_t calculated from Eq. (3.9) in all 160 cases of the liquid temperature differences. In Fig. 3.5, the closed circles denote T_t, and the closed triangles denote T_n; the ordinate represents T_n and T_t normalized by the reference liquid temperature T_L, and the abscissa represents the index of the degree of net evaporation/condensation. In this thesis, we define this index as J_{coll}/J^*_{out}, where J^*_{out} indicates J_{out} in vapor–liquid equilibrium and $J^*_{out} = J^*_{coll} = \rho^*\sqrt{RT_L/2\pi}$. From the definition of σ (Eq. (1.33)),

$$\sigma\sqrt{\frac{RT_L}{2\pi}} = -\int_{\xi_z<0} \xi_z f_{coll} d\boldsymbol{\xi} = J_{coll}, \tag{3.10}$$

J_{coll}/J^*_{out} becomes σ/ρ^*. $\sigma/\rho^* = 1$ represents the vapor–liquid equilibrium state, $\sigma/\rho^* < 1$ and $\sigma/\rho^* > 1$ represent the net evaporation and net condensation states,

respectively. Net evaporation or condensation becomes strong when σ/ρ^* goes away from unity.

As can be seen in Fig. 3.5, T_n increases with strong net evaporation and decreases with strong net condensation. On the other hand, T_t decreases with strong net evaporation and increases with strong net condensation. The previous studies have reported that these temperatures deviate from the liquid temperature only when net evaporation/condensation is strong. In contrast, Fig. 3.5 clearly shows that these temperatures gradually deviate from T_L when σ/ρ^* goes away from unity.

Influence of anisotropic Maxwellian distribution

In the former section, we find that the normal and tangential temperatures in the KBC gradually change with the degree of net evaporation/condensation, and the normalized velocity distribution function of the KBC becomes an anisotropic Maxwellian distribution. Here, we investigate how such an anisotropic Maxwellian distribution affects the macroscopic variables and the fluxes in vapor. The goal here is to determine the range to which the normalized Maxwellian distribution can be applied as the normalized velocity distribution function of the KBC.

To examine the influence of the anisotropic Maxwellian distribution on the macroscopic variables and the fluxes in vapor, we perform the numerical simulation of the Boltzmann equation for the two-surface problem. In this numerical simulation, we utilize the ES-BGK model Boltzmann equation (ES-BGK equation) [89] that is one of the models of the Boltzmann equation. We explain the ES-BGK equation and its numerical simulation method in Chapter 5; only the outline of this numerical simulation is shown here. The reference values for the nondimensionalization are the mean temperature of two liquids $T_0 = (T_{\mathrm{L}1} + T_{\mathrm{L}2})/2$, the mean free path ℓ_0 at T_0, and the mean free time $\bar{\mu}_0^{-1}$ at T_0. We perform the numerical simulation in the one-dimensional physical space and three-dimensional molecular velocity space, but the molecular velocity space is treated as a pseudo-one-dimensional by using a

simulation technique. We discretize the time, the physical space, and the molecular velocity space and solve the ES-BGK equation by the finite difference method. The cell size in the physical space Δz is set to $1.0 \times 10^{-4} \ell_0$, that in the molecular velocity space $\Delta \xi_z$ is set to $1.0 \times 10^{-2} \sqrt{2RT_0}$ near $\xi_z = 0$ and $1.0 \times 10^{-4} \sqrt{2RT_0}$ far from $\xi_z = 0$, and the time step Δt is set to $0.01 \bar{\mu}_0^{-1}$.

In the numerical simulation of the ES-BGK equation, we impose the KBC rewritten in the following procedure. We solve the mass flux relation at the vapor–liquid interface (Eq. (2.3)) for $\mathcal{A}$,

$$\mathcal{A} = \rho v_z \sqrt{\frac{2\pi}{RT_\mathrm{L}}} + \sigma, \tag{3.11}$$

and then we substitute the above expression into the generalized KBC (Eq. (2.1)) to get

$$f_\mathrm{out} = \left(\rho v_z \sqrt{\frac{2\pi}{RT_\mathrm{L}}} + \sigma \right) \hat{f}^*. \tag{3.12}$$

In Eq. (3.12), the normalized Maxwellian distribution is assumed for the normalized velocity distribution function of the KBC. On the other hand, the EV-DSMC simulation does not use the assumption for the vapor–liquid interface; hence, the result of this simulation encloses the influence of the anisotropic Maxwellian distribution. We investigate the influence of the anisotropic Maxwellian distribution by comparing the macroscopic variables and the fluxes in vapor obtained by these two simulations.

Figure 3.6 shows the mass and energy fluxes, the density, the velocity, and the temperature in vapor obtained from the EV-DSMC simulation and the numerical simulation of the ES-BGK equation in the cases of (1) $T_{\mathrm{L}1}/T_\mathrm{c} = 0.76$ and $T_{\mathrm{L}2}/T_\mathrm{c} = 0.60$, (2) $T_{\mathrm{L}1}/T_\mathrm{c} = 0.68$ and $T_{\mathrm{L}2}/T_\mathrm{c} = 0.60$, (3) $T_{\mathrm{L}1}/T_\mathrm{c} = 0.61$ and $T_{\mathrm{L}2}/T_\mathrm{c} = 0.60$, and (4) $T_{\mathrm{L}1}/T_\mathrm{c} = 0.60$ and $T_{\mathrm{L}2}/T_\mathrm{c} = 0.56$. In Fig. 3.6, the solid lines denote the results of the numerical simulation of the ES-BGK equation, the open circles and

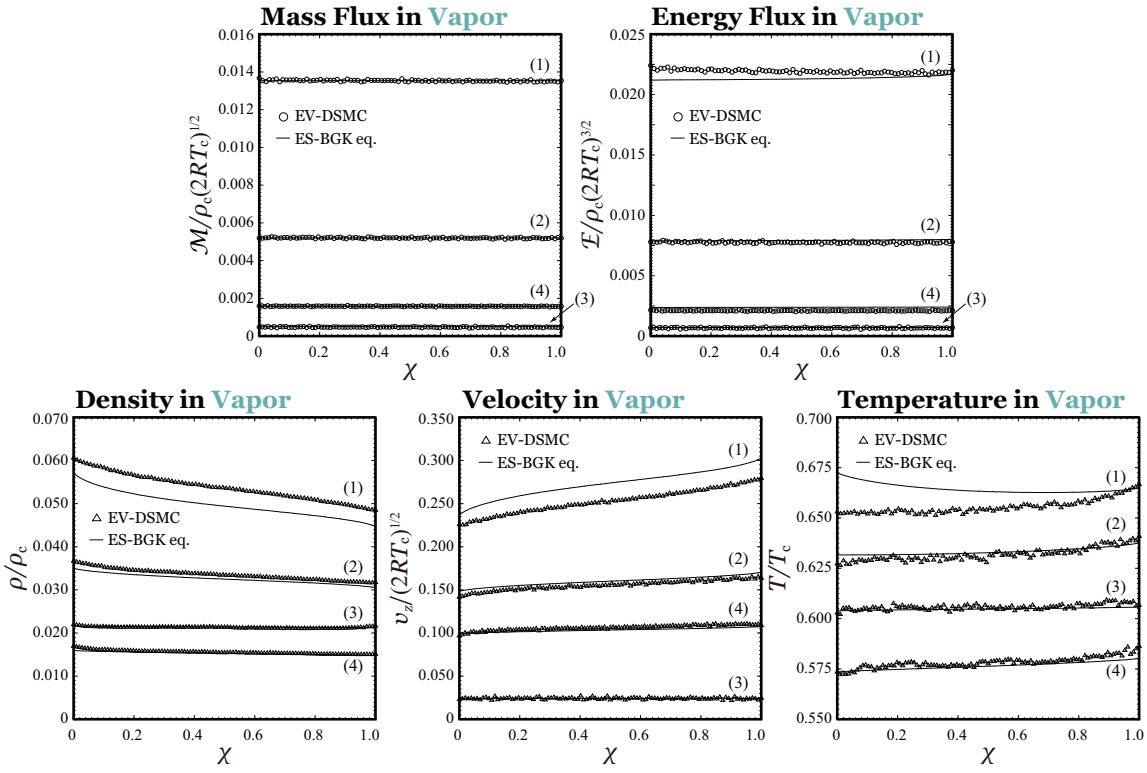

Figure 3.6: Comparison of the mass flux $\mathcal{M}$ and the energy flux $\mathcal{E}$, the density ρ, the velocity v_z, and the temperature T in vapor obtained from the EV-DSMC simulation and the numerical simulation of the ES-BGK equation in the cases of (1) $T_{\mathrm{L}1}/T_{\mathrm{c}} = 0.76$ and $T_{\mathrm{L}2}/T_{\mathrm{c}} = 0.60$, (2) $T_{\mathrm{L}1}/T_{\mathrm{c}} = 0.68$ and $T_{\mathrm{L}2}/T_{\mathrm{c}} = 0.60$, (3) $T_{\mathrm{L}1}/T_{\mathrm{c}} = 0.61$ and $T_{\mathrm{L}2}/T_{\mathrm{c}} = 0.60$, and (4) $T_{\mathrm{L}1}/T_{\mathrm{c}} = 0.60$ and $T_{\mathrm{L}2}/T_{\mathrm{c}} = 0.56$; the abscissa χ is the spatial coordinate in vapor ($\chi = 0$ indicates the left vapor–liquid interface in Fig. 3.2, and $\chi = 1$ indicates that of the right side), and the ordinates are normalized by the critical values.

triangles denote the results of the EV-DSMC simulation.

As can be seen in Fig. 3.6, the mass fluxes in vapor obtained by the two different simulations show excellent agreement even in the strong net evaporation/condensation case induced by the larger temperature difference between two liquids. This is because the change in the normal temperature T_{n} is smaller than that in the tangential temperature T_{t} as shown in Fig. 3.5. When $T_{\mathrm{n}} = T_{\mathrm{L}}$, J_{out} obtained by Eq. (3.12) becomes $\rho v_z + \sigma\sqrt{RT_{\mathrm{L}}/(2\pi)}$, and ρv_z at the vapor–liquid interface in the two simulations are completely identical. In contrast, the deviations of the energy flux, the density, the velocity, and the temperature between these two simulations become larger with strong net evaporation/condensation. In particular,

the slope of the temperature obtained from these two simulations is reversed when net evaporation/condensation is extremely strong (Case (1) in Fig. 3.6).

We here decide the applicable range of the normalized Maxwellian based on the macroscopic variables which have larger deviations between these two simulations than the fluxes. In this simulation, the range to which the difference of the macroscopic variables obtained from these two simulations is within 5% is defined as the applicable range. To determine the applicable range for each reference liquid temperature, we perform such a comparison for all 160 cases of the temperature difference. As a result, we find that the applicable range of the normalized Maxwellian distribution is $0.5 \lesssim \sigma/\rho^* \lesssim 2.3$ for all reference liquid temperatures. The gray region in Fig. 3.5 represents this applicable range. As can be seen in Fig. 3.5, when the normal and tangential temperatures in the KBC deviate by approximately 5–10% from the liquid temperature, the difference of the macroscopic variables obtained by two different simulations reaches 5%. On the basis of this result, we discuss the mass flux relation in the range of this degree of net evaporation/condensation ($0.5 \lesssim \sigma/\rho^* \lesssim 2.3$).

3.2.3 Formulation of mass flux relation

Next, we investigate the mass flux relation at the vapor–liquid interface (Eq. (2.3)):

$$\rho v_z = (\mathcal{A} - \sigma)\sqrt{\frac{RT_\mathrm{L}}{2\pi}}. \tag{2.3}$$

As stated in Chapter 1 (Section 1.3.1), $\mathcal{A}$ satisfies the following conditions: (1) $\mathcal{A}$ is the nonnegative function, (2) $\mathcal{A}$ is allowable to be the function of the liquid temperature T_L and/or σ (Eq. (1.33)), and (3) $\mathcal{A}$ is independent of the molecular velocity. Under this condition, ρv_z is the function of T_L and σ. Here, we obtain ρv_z under the various cases of T_L and σ to investigate Eq. (2.3). In the simulation system shown in Fig. 3.1, ρv_z and corresponding σ vary with the change of the

temperature difference between two liquids. We can calculate σ corresponding to ρv_z from the numerical simulation of the ES-BGK equation with the KBC rewritten with ρv_z (Eq. (3.12)). The values of ρv_z and corresponding σ are summarized in Tables 3.1–3.7.

Figure 3.7 shows the relation between ρv_z and σ, that is, the mass flux relation, at each reference liquid temperature. In Fig. 3.7, we show the results only in the applicable range of the normalized Maxwellian distribution ($0.5 \lesssim \sigma/\rho^* \lesssim 2.3$). In the abscissa, we subtract one from the degree of net evaporation/condensation σ/ρ^* for convenience. Also, the ordinate is normalized by J^*_{out} to match the reference value of the abscissa. When the liquid temperature difference becomes larger, the deviation of $\sigma/\rho^* - 1$ from zero increases and net evaporation and condensation become stronger. Although in the simulation system (Fig. 3.1), ρv_z in both net evaporation and condensation cases have the positive values, we plot Fig. 3.7 with $\rho v_z > 0$ for net evaporation and $\rho v_z < 0$ for net condensation for convenience.

As can be clearly seen in Fig. 3.7, ρv_z is the linear function of σ at each reference liquid temperature. Similar mass flux relations for water and methanol are observed in the shock-tube experiment [90]. In this simulation, we succeed to show the mass flux relation more clearly owing to the small statistical errors. The open square in the enlarged view of Fig. 3.7(a) denotes ρv_z obtained in the system whose length is doubled ($L_{\text{H}} = 80a$) in the case of $T_{\text{L1}}/T_{\text{c}} = 0.68$ and $T_{\text{L2}}/T_{\text{c}} = 0.60$. From this result, we find that even in the system with the doubled length, the linear mass flux relation is maintained.

We formulate the mass flux relation by applying the linear regression analysis to the relation between ρv_z and σ at each reference liquid temperature. The dashed lines in Fig. 3.7 denote the results of applying the linear regression analysis separately for the cases of net evaporation and net condensation. The accuracy of this analysis is very high, in which case the coefficient of the determination R^2 is more than 0.999. The slopes of the linear function obtained from this analysis are referred to as β_{ne}

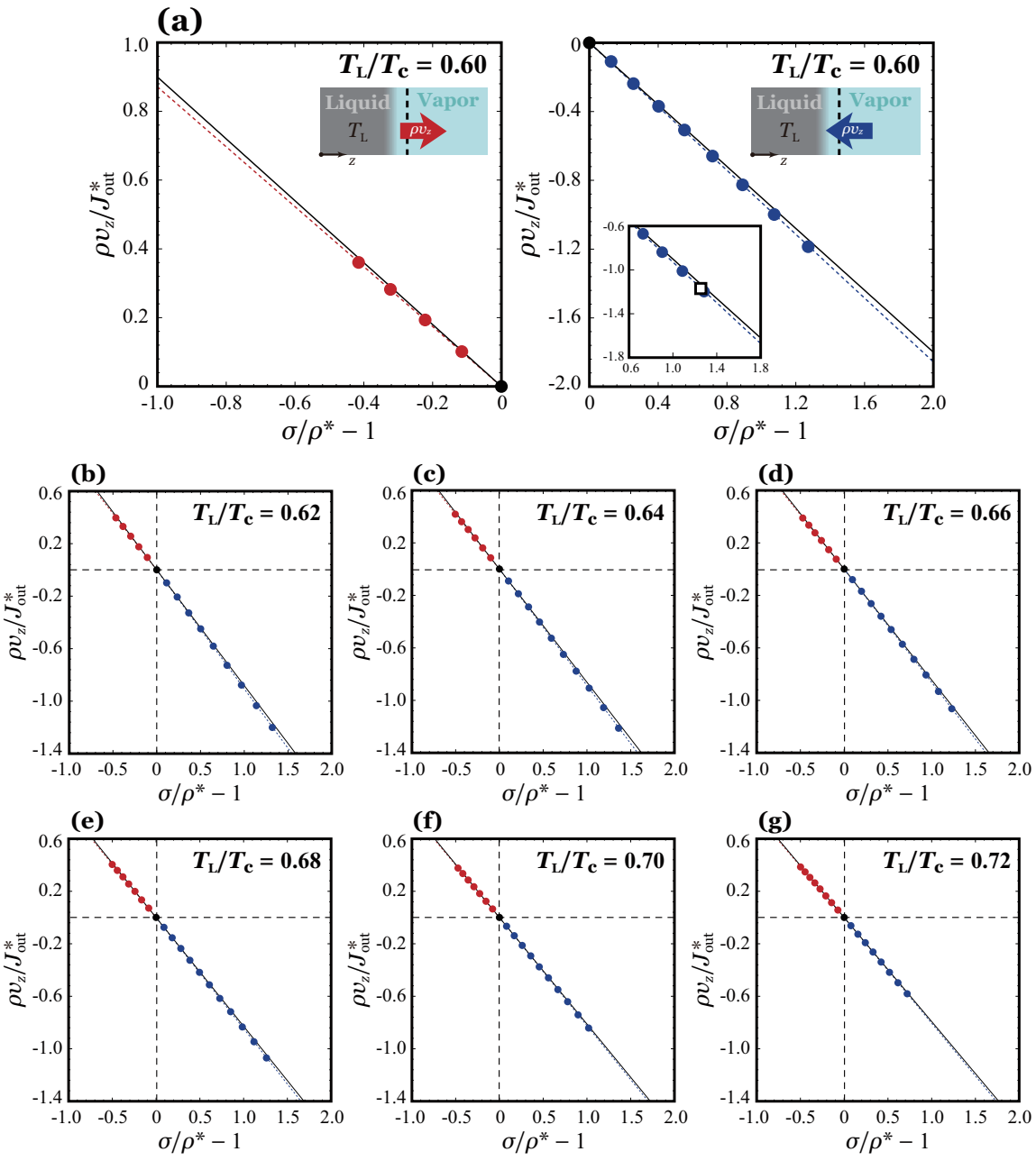

Figure 3.7: Relation between $\rho v_z/J^*_{\mathrm{out}}$ and σ/ρ^* in the cases of (a) $T_{\mathrm{L}}/T_{\mathrm{c}} = 0.60$, (b) $T_{\mathrm{L}}/T_{\mathrm{c}} = 0.62$, (c) $T_{\mathrm{L}}/T_{\mathrm{c}} = 0.64$, (d) $T_{\mathrm{L}}/T_{\mathrm{c}} = 0.66$, (e) $T_{\mathrm{L}}/T_{\mathrm{c}} = 0.68$, (f) $T_{\mathrm{L}}/T_{\mathrm{c}} = 0.70$, and (g) $T_{\mathrm{L}}/T_{\mathrm{c}} = 0.72$.

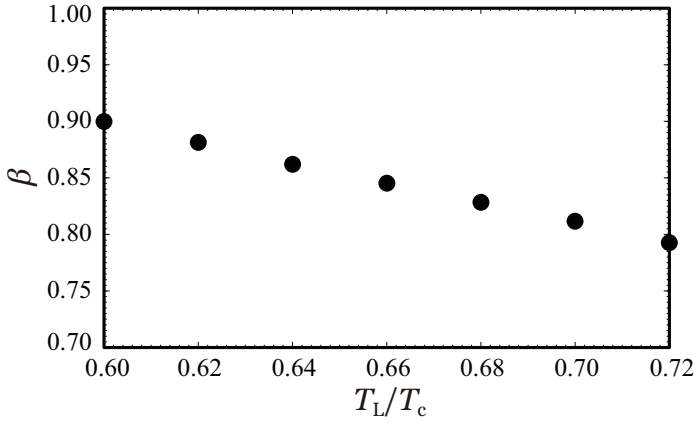

Figure 3.8: Liquid temperature dependence of β; the abscissa is normalized by critical temperature T_c.

for net evaporation and β_{nc} for net condensation. The values of β_{ne} and β_{nc} are summarized in Tables 3.1–3.7. In all cases of the reference liquid temperature, β_{ne} and β_{nc} are slightly different. For example, $\beta_{ne} = 0.871$ and $\beta_{nc} = 0.927$ in the case of $T_L/T_c = 0.60$. Also, the difference between β_{ne} and β_{nc} becomes smaller with the higher reference liquid temperature.

Unfortunately, the cause of the difference between β_{ne} and β_{nc} is unclear. It may be due that the mass flux relation is formulated at each liquid temperature despite the temperatures in the KBC change with σ/ρ^* as shown in Fig. 3.5. At least, the generalized KBC (Eq. (2.1)), which is considered in this thesis, does not permit such formulation according to σ. It may be possible to perform the molecular gas dynamics analysis by defining the nonlinear scattering kernel, but such an analysis is mathematically complex and has never been precisely investigated. Furthermore, the difference between β_{ne} and β_{nc} shows the existence of the asymmetry in net evaporation and condensation near vapor–liquid equilibrium. As shown in Tables 3.1–3.7, although the difference between β_{ne} and β_{nc} is small, the vapor–liquid equilibrium may not achieve asymptotically stable because of this asymmetry.

For these reasons, we modify the slope of the mass flux relation at each reference

liquid temperature as

$$\beta = \frac{\beta_{\mathrm{ne}} + \beta_{\mathrm{nc}}}{2}. \tag{3.13}$$

The solid lines in Fig. 3.7 denote the linear function with the slope β. As shown in Fig. 3.7, the solid lines slightly differ from the data as compared with the dashed lines, but we confirm that this is a reasonable approximation in which R^2 calculated according to its definition is more than 0.999. The values of β at the reference liquid temperatures are summarized in Tables 3.1–3.7. Furthermore, the liquid temperature dependence of β is shown in Fig. 3.8. As can be seen in Fig. 3.8, β is a decreasing function of the liquid temperature. From the above discussion, we formulate the mass flux relation as

$$\frac{\rho v_z}{J^*_{\mathrm{out}}} = \beta \left(1 - \frac{\sigma}{\rho^*}\right), \tag{3.14}$$

where $J^*_{\mathrm{out}} = \rho^* \sqrt{RT_{\mathrm{L}}/(2\pi)}$.

3.2.4 Examination of evaporation/condensation coefficients

We then discuss the evaporation coefficient α_{e} and the condensation coefficient α_{c} defined by Eq. (1.42) by comparing the formulated mass flux relation (Eq. (3.14)) with Eq. (1.44). In this way, we can find a pair of α_{e} and α_{c} without explicitly defining the molecular processes illustrated in Fig. 1.1.

We transform Eq. (2.3) as

$$\rho v_z \sqrt{\frac{2\pi}{RT_{\mathrm{L}}}} = \mathcal{A} - \sigma. \tag{3.15}$$

Also, we transform the formulated mass flux relation (Eq. (3.14)) as

$$\rho v_z \sqrt{\frac{2\pi}{RT_{\mathrm{L}}}} = \beta(\rho^* - \sigma). \tag{3.16}$$

From the result of the former section (Figs. 3.7 and 3.8), we find that β depends only on the liquid temperature and is independent of σ. Hereafter, we express such β as $\beta(T_{\mathrm{L}})$. Equalizing the right-hand side of Eq. (3.15) and that of Eq. (3.16), we get

$$\frac{\mathcal{B}(T_{\mathrm{L}})}{\rho^*} = 1 - \frac{\mathcal{A} - \mathcal{B}(T_{\mathrm{L}})}{\sigma}, \tag{3.17}$$

where $\mathcal{B}$ is defined as

$$\mathcal{B} = \rho^* \beta(T_{\mathrm{L}}). \tag{3.18}$$

Since ρ^* is the saturated vapor density at T_{L}, $\mathcal{B}$ is only the function of the liquid temperature. We also express such $\mathcal{B}$ as $\mathcal{B}(T_{\mathrm{L}})$. As explained in Chapter 1 (Section 1.3.1), α_{e} and α_{c} are defined by

$$\alpha_{\mathrm{e}} = \frac{\mathcal{A}_0(T_{\mathrm{L}})}{\rho^*}, \qquad \alpha_{\mathrm{c}} = 1 - \frac{\mathcal{A} - \mathcal{A}_0(T_{\mathrm{L}})}{\sigma}. \tag{1.42}$$

In Eqs. (3.17) and (1.42), $\mathcal{A}_0(T_{\mathrm{L}})$ is equivalent to $\mathcal{B}(T_{\mathrm{L}})$, and thus we get the relation $\alpha_{\mathrm{e}} = \alpha_{\mathrm{c}} = \beta(T_{\mathrm{L}})$. In other words, α_{e} and α_{c} depend only on the liquid temperature and are independent of σ.

3.3 Summary

In this chapter, we examined the mass flux relation (Eq. (2.3)) to find a pair of α_{e} and α_{c} defined by Eq. (1.42) by the EV-DSMC simulation explained in Chapter 2. We preliminarily performed the EV-DSMC simulation for the two-surface problem in 160 cases of the temperature differences between two liquids.

First, we confirmed whether the normalized velocity distribution function of the KBC obeys the normalized Maxwellian distribution, which is the basis of the definitions of α_{e} and α_{c} (Eq. (1.42)). From the result, we found that the tempera-

tures in the KBC gradually change with strong net evaporation/condensation, and the normalized velocity distribution function of the KBC becomes the anisotropic Maxwellian distribution (Fig. 3.5). We then investigated how such an anisotropic Maxwellian distribution affects the macroscopic variables and the fluxes in vapor by comparing the results obtained from the EV-DSMC simulation and the numerical simulation of the ES-BGK equation. From this comparison, we determined the range to which the normalized Maxwellian distribution can be applied as the normalized velocity distribution function of the KBC. From the result, we found that the applicable range of the normalized Maxwellian distribution is $0.5 \lesssim \sigma/\rho^* \lesssim 2.3$ for all reference liquid temperatures.

Next, we formulated the mass flux at each reference liquid temperature relation by using ρv_z obtained by the molecular simulation and corresponding σ (Eq. (2.4)). From the result, we found that ρv_z is the linear function of σ (Fig. 3.7). We formulated the mass flux relation by applying the linear regression analysis to the relation between ρv_z and σ at each reference liquid temperature. The slope of the linear function β_{ne} for net evaporation and that of β_{nc} for net condensation are slightly different. For example, $\beta_{\mathrm{ne}} = 0.871$ and $\beta_{\mathrm{nc}} = 0.927$ in the case of $T_{\mathrm{L}}/T_{\mathrm{c}} = 0.60$. Also, the difference between β_{ne} and β_{nc} becomes smaller with the higher reference liquid temperature. Unfortunately, the cause of the difference between β_{ne} and β_{nc} is unclear. At least, the generalized KBC (Eq. (2.1)), which is considered in this thesis, does not permit such formulation according to σ. Hence, we modified the slope of the mass flux relation as $\beta = (\beta_{\mathrm{ne}} + \beta_{\mathrm{nc}})/2$. We then discussed α_{e} and α_{c} defined by Eq. (1.42) by comparing the formulated mass flux relation (Eq. (3.14)) with Eq. (2.3). From the result, we found the relation $\alpha_{\mathrm{e}} = \alpha_{\mathrm{c}} = \beta(T_{\mathrm{L}})$ without explicitly defining the molecular processes illustrated in Fig. 1.1.

Let us summarize the significance of the results so far. An important result is that we can find the relation $\alpha_{\mathrm{e}} = \alpha_{\mathrm{c}} = \beta(T_{\mathrm{L}})$ by formulating the mass flux relation at the vapor–liquid interface with high accuracy. On the basis of this result, the

following KBC at the vapor–liquid interface can be obtained.

$$f_{\mathrm{out}} = [\beta(T_{\mathrm{L}})\rho^* + (1 - \beta(T_{\mathrm{L}}))\sigma]\hat{f}^*. \tag{3.19}$$

This KBC is essentially equivalent to what we set $\mathcal{A} = \alpha_{\mathrm{e}}\rho^* + (1 - \alpha_{\mathrm{c}})\sigma$ in the generalized KBC (Eq. (2.1)) because of the relation $\alpha_{\mathrm{e}} = \alpha_{\mathrm{c}} = \beta(T_{\mathrm{L}})$. However, the results in this chapter have only found a pair of α_{e} and α_{c} defined by Eq. (1.42) at each liquid temperature, and the relation between these coefficients and the molecular processes shown in Fig. 1.1 is not clear. In the next chapter, to investigate the physical meaning of obtained α_{e} and α_{c}, we discuss these coefficients under the assumption proposed by Ishiyama *et al.* [33].

Table 3.1: Results of the EV-DSMC simulation at $T_{\mathrm{L}}/T_{\mathrm{c}} = 0.60$.

#	$T_{\mathrm{L1}}/T_{\mathrm{c}}$	$T_{\mathrm{L2}}/T_{\mathrm{c}}$	L_{V}/a	$\rho v_z/J^*_{\mathrm{out}}$	σ/ρ^*	β_{ne}	β_{nc}	β
1	0.60	0.56	21.2	0.3607	0.5849		—	
2	0.60	0.57	21.0	0.2821	0.6773		—	
3	0.60	0.58	20.8	0.1934	0.7782	0.871	—	
4	0.60	0.59	20.8	0.1014	0.8848		—	
5	0.61	0.60	20.4	-0.1086	1.1265	—		
6	0.62	0.60	20.4	-0.2376	1.2561	—		
7	0.63	0.60	20.2	-0.3696	1.4021	—		0.900
8	0.64	0.60	20.0	-0.5069	1.5526	—		
9	0.65	0.60	19.8	-0.6595	1.7157	—	0.928	
10	0.66	0.60	19.8	-0.8262	1.8909	—		
11	0.67	0.60	19.6	-0.9988	2.0747	—		
12	0.68	0.60	19.4	-1.1863	2.2715	—		
13	0.69	0.60	19.2	-1.3910	2.4828	—	—	—
14	0.70	0.60	19.0	-1.5897	2.6969	—	—	—
15	0.71	0.60	18.8	-1.8177	2.9321	—	—	—
16	0.72	0.60	18.6	-2.0326	3.1667	—	—	—
17	0.73	0.60	18.4	-2.2806	3.4248	—	—	—
18	0.74	0.60	18.2	-2.5354	3.6930	—	—	—
19	0.75	0.60	18.0	-2.8078	3.9771	—	—	—
20	0.76	0.60	17.8	-3.0871	4.2714	—	—	—

Table 3.2: Results of the EV-DSMC simulation at $T_{\mathrm{L}}/T_{\mathrm{c}} = 0.62$.

#	$T_{\mathrm{L1}}/T_{\mathrm{c}}$	$T_{\mathrm{L2}}/T_{\mathrm{c}}$	L_{V}/a	$\rho v_z/J^*_{\mathrm{out}}$	σ/ρ^*	β_{ne}	β_{nc}	β
21	0.62	0.56	21.0	0.4530	0.4616	—	—	—
22	0.62	0.57	20.8	0.3969	0.5342		—	
23	0.62	0.58	20.6	0.3313	0.6141		—	
24	0.62	0.59	20.6	0.2567	0.7015	0.857	—	
25	0.62	0.60	20.4	0.1770	0.7946		—	
26	0.62	0.61	20.2	0.0955	0.8922		—	
27	0.63	0.62	20.0	-0.0990	1.1129	—		
28	0.64	0.62	19.8	-0.2068	1.2340	—		
29	0.65	0.62	19.8	-0.3282	1.3656	—		0.881
30	0.66	0.62	19.6	-0.4490	1.5013	—		
31	0.67	0.62	19.4	-0.5800	1.6464	—	0.906	
32	0.68	0.62	19.2	-0.7273	1.8039	—		
33	0.69	0.62	19.0	-0.8780	1.9678	—		
34	0.70	0.62	18.8	-1.0339	2.1391	—		
35	0.71	0.62	18.6	-1.2006	2.3207	—		
36	0.72	0.62	18.4	-1.3852	2.5164	—	—	—
37	0.73	0.62	18.2	-1.5613	2.7127	—	—	—
38	0.74	0.62	18.0	-1.7614	2.9267	—	—	—
39	0.75	0.62	17.8	-1.9713	3.1510	—	—	—
40	0.76	0.62	17.6	-2.1833	3.3819	—	—	—

Table 3.3: Results of the EV-DSMC simulation at $T_{\mathrm{L}}/T_{\mathrm{c}} = 0.64$.

#	$T_{\mathrm{L1}}/T_{\mathrm{c}}$	$T_{\mathrm{L2}}/T_{\mathrm{c}}$	L_{V}/a	$\rho v_z/J^*_{\mathrm{out}}$	σ/ρ^*	β_{ne}	β_{nc}	β
41	0.64	0.56	20.6	0.5147	0.3707	—	—	—
42	0.64	0.57	20.4	0.4716	0.4300	—	—	—
43	0.64	0.58	20.2	0.4183	0.4963		—	
44	0.64	0.59	20.2	0.3613	0.5670		—	
45	0.64	0.60	20.0	0.3021	0.6416	0.838	—	
46	0.64	0.61	19.8	0.2378	0.7214		—	
47	0.64	0.62	19.8	0.1611	0.8098		—	
48	0.64	0.63	19.6	0.0860	0.9008		—	
49	0.65	0.64	19.4	-0.0903	1.1043	—		
50	0.66	0.64	19.2	-0.1872	1.2153	—		0.862
51	0.67	0.64	19.0	-0.2875	1.3314	—		
52	0.68	0.64	18.8	-0.4024	1.4583	—		
53	0.69	0.64	18.6	-0.5257	1.5930	—	0.886	
54	0.70	0.64	18.4	-0.6492	1.7318	—		
55	0.71	0.64	18.2	-0.7771	1.8768	—		
56	0.72	0.64	18.0	-0.9069	2.0268	—		
57	0.73	0.64	17.8	-1.0556	2.1903	—		
58	0.74	0.64	17.6	-1.2116	2.3618	—		
59	0.75	0.64	17.4	-1.3700	2.5389	—	—	—
60	0.76	0.64	17.2	-1.5420	2.7273	—	—	—
61	0.77	0.64	17.0	-1.7076	2.9158	—	—	—
62	0.78	0.64	16.8	-1.8916	3.1216	—	—	—
63	0.79	0.64	16.6	-2.0797	3.3328	—	—	—
64	0.80	0.64	16.4	-2.2865	3.5559	—	—	—

Table 3.4: Results of the EV-DSMC simulation at $T_{\mathrm{L}}/T_{\mathrm{c}} = 0.66$.

#	$T_{\mathrm{L1}}/T_{\mathrm{c}}$	$T_{\mathrm{L2}}/T_{\mathrm{c}}$	L_{V}/a	$\rho v_z/J^*_{\mathrm{out}}$	σ/ρ^*	β_{ne}	β_{nc}	β
65	0.66	0.56	20.4	0.5587	0.3021	—	—	—
66	0.66	0.57	20.2	0.5219	0.3525	—	—	—
67	0.66	0.58	20.0	0.4822	0.4064	—	—	—
68	0.66	0.59	20.0	0.4343	0.4661	—	—	—
69	0.66	0.60	19.8	0.3889	0.5271		—	
70	0.66	0.61	19.6	0.3348	0.5944		—	
71	0.66	0.62	19.6	0.2765	0.6661	0.827	—	
72	0.66	0.63	19.4	0.2181	0.7406		—	
73	0.66	0.64	19.2	0.1480	0.8229		—	
74	0.66	0.65	19.0	0.0757	0.9092		—	
75	0.67	0.66	18.8	-0.0799	1.0955	—		
76	0.68	0.66	18.6	-0.1687	1.1982	—		0.845
77	0.69	0.66	18.4	-0.2632	1.3067	—		
78	0.70	0.66	18.2	-0.3588	1.4191	—		
79	0.71	0.66	18.0	-0.4603	1.5375	—	0.863	
80	0.72	0.66	17.8	-0.5728	1.6647	—		
81	0.73	0.66	17.6	-0.6879	1.7966	—		
82	0.74	0.66	17.4	-0.8071	1.9341	—		
83	0.75	0.66	17.2	-0.9313	2.0776	—		
84	0.76	0.66	17.0	-1.0640	2.2290	—		
85	0.77	0.66	16.8	-1.2030	2.3873	—	—	—
86	0.78	0.66	16.6	-1.3473	2.5521	—	—	—
87	0.79	0.66	16.4	-1.5018	2.7259	—	—	—
88	0.80	0.66	16.2	-1.6550	2.9029	—	—	—

Table 3.5: Results of the EV-DSMC simulation at $T_{\mathrm{L}}/T_{\mathrm{c}} = 0.68$.

#	$T_{\mathrm{L1}}/T_{\mathrm{c}}$	$T_{\mathrm{L2}}/T_{\mathrm{c}}$	L_{V}/a	$\rho v_z/J^*_{\mathrm{out}}$	σ/ρ^*	β_{ne}	β_{nc}	β
89	0.68	0.56	20.0	0.5854	0.2513	—	—	—
90	0.68	0.57	19.8	0.5558	0.2938	—	—	—
91	0.68	0.58	19.6	0.5234	0.3393	—	—	—
92	0.68	0.59	19.6	0.4887	0.3878	—	—	—
93	0.68	0.60	19.4	0.4486	0.4405	—	—	—
94	0.68	0.61	19.4	0.4038	0.4974		—	
95	0.68	0.62	19.2	0.3593	0.5563		—	
96	0.68	0.63	19.0	0.3094	0.6198		—	
97	0.68	0.64	18.8	0.2553	0.6874	0.811	—	
98	0.68	0.65	18.6	0.1996	0.7581		—	
99	0.68	0.66	18.6	0.1354	0.8352		—	
100	0.68	0.67	18.4	0.0715	0.9146		—	
101	0.69	0.68	18.0	-0.0745	1.0893	—		
102	0.70	0.68	17.8	-0.1535	1.1834	—		0.828
103	0.71	0.68	17.6	-0.2360	1.2820	—		
104	0.72	0.68	17.4	-0.3254	1.3867	—		
105	0.73	0.68	17.2	-0.4166	1.4951	—		
106	0.74	0.68	17.0	-0.5126	1.6088	—	0.845	
107	0.75	0.68	16.8	-0.6156	1.7289	—		
108	0.76	0.68	16.6	-0.7177	1.8516	—		
109	0.77	0.68	16.4	-0.8337	1.9842	—		
110	0.78	0.68	16.2	-0.9470	2.1187	—		
111	0.79	0.68	16.0	-1.0699	2.2612	—		
112	0.80	0.68	15.8	-1.1912	2.4062	—	—	—

Table 3.6: Results of the EV-DSMC simulation at $T_{\mathrm{L}}/T_{\mathrm{c}} = 0.70$.

#	$T_{\mathrm{L1}}/T_{\mathrm{c}}$	$T_{\mathrm{L2}}/T_{\mathrm{c}}$	L_{V}/a	$\rho v_z/J^*_{\mathrm{out}}$	σ/ρ^*	β_{ne}	β_{nc}	β
113	0.70	0.56	19.6	0.5985	0.2142	—	—	—
114	0.70	0.57	19.4	0.5746	0.2503	—	—	—
115	0.70	0.58	19.2	0.5465	0.2897	—	—	—
116	0.70	0.59	19.0	0.5172	0.3313	—	—	—
117	0.70	0.60	19.0	0.4886	0.3746	—	—	—
118	0.70	0.61	18.8	0.4523	0.4225	—	—	—
119	0.70	0.62	18.8	0.4152	0.4729	—	—	—
120	0.70	0.63	18.6	0.3770	0.5255		—	
121	0.70	0.64	18.4	0.3348	0.5818		—	
122	0.70	0.65	18.2	0.2861	0.6429		—	
123	0.70	0.66	18.2	0.2340	0.7076	0.800	—	
124	0.70	0.67	18.2	0.1820	0.7745		—	
125	0.70	0.68	17.8	0.1247	0.8458		—	
126	0.70	0.69	17.6	0.0654	0.9204		—	
127	0.71	0.70	17.2	-0.0656	1.0820	—		
128	0.72	0.70	17.0	-0.1386	1.1696	—		0.812
129	0.73	0.70	16.8	-0.2134	1.2607	—		
130	0.74	0.70	16.6	-0.2928	1.3564	—		
131	0.75	0.70	16.4	-0.3752	1.4561	—	0.823	
132	0.76	0.70	16.2	-0.4600	1.5595	—		
133	0.77	0.70	16.0	-0.5496	1.6679	—		
134	0.78	0.70	15.8	-0.6406	1.7796	—		
135	0.79	0.70	15.6	-0.7422	1.8992	—		
136	0.80	0.70	15.4	-0.8414	2.0203	—		

Table 3.7: Results of the EV-DSMC simulation at $T_{\mathrm{L}}/T_{\mathrm{c}} = 0.72$.

#	$T_{\mathrm{L1}}/T_{\mathrm{c}}$	$T_{\mathrm{L2}}/T_{\mathrm{c}}$	L_{V}/a	$\rho v_z/J^*_{\mathrm{out}}$	σ/ρ^*	β_{ne}	β_{nc}	β
137	0.72	0.56	19.2	0.6066	0.1855	—	—	—
138	0.72	0.57	19.0	0.5872	0.2165	—	—	—
139	0.72	0.58	18.8	0.5654	0.2499	—	—	—
140	0.72	0.59	18.6	0.5428	0.2850	—	—	—
141	0.72	0.60	18.6	0.5151	0.3237	—	—	—
142	0.72	0.61	18.4	0.4872	0.3640	—	—	—
143	0.72	0.62	18.4	0.4575	0.4068	—	—	—
144	0.72	0.63	18.2	0.4228	0.4531	—	—	—
145	0.72	0.64	18.0	0.3847	0.5025		—	
146	0.72	0.65	17.8	0.3472	0.5535		—	
147	0.72	0.66	17.8	0.3063	0.6078		—	
148	0.72	0.67	17.6	0.2647	0.6642	0.780	—	
149	0.72	0.68	17.4	0.2175	0.7248		—	
150	0.72	0.69	17.2	0.1648	0.7898		—	
151	0.72	0.70	17.0	0.1140	0.8560		—	
152	0.72	0.71	16.8	0.0566	0.9271		—	0.793
153	0.73	0.72	16.4	-0.0613	1.0769	—		
154	0.74	0.72	16.2	-0.1261	1.1577	—		
155	0.75	0.72	16.0	-0.1914	1.2408	—		
156	0.76	0.72	15.8	-0.2631	1.3291	—	0.805	
157	0.77	0.72	15.6	-0.3392	1.4217	—		
158	0.78	0.72	15.4	-0.4167	1.5173	—		
159	0.79	0.72	15.2	-0.4966	1.6163	—		
160	0.80	0.72	15.0	-0.5816	1.7201	—		

Chapter

4

Physical consideration of kinetic boundary condition

In Chapter 3, we found a pair of α_e and α_c defined by Eq. (1.42) at each liquid temperature. In this chapter, we consider the physical meaning of these coefficients obtained in Chapter 3. To determine α_e and α_c uniquely, we have to clarify the definitions of the molecular processes illustrated in Fig. 1.1. Although this definition has not been clarified, if we assume a certain condition, these molecular processes can be distinguished. We here consider a hypothesis of the spontaneous evaporation [33,44]. According to this hypothesis, α_e and α_c are defined by the mass fluxes related to the molecular processes. α_e and α_c according to this hypothesis can be obtained from the virtual vacuum simulation [26,33] and the net evaporation and condensation simulation [34]. However, the virtual vacuum simulation is inappropriate when the liquid temperature becomes relatively high; hence, we apply a new method, which is called the two-boundary method, proposed by Kobayashi et al. [30] to estimate α_e and α_c according to the hypothesis of the spontaneous evaporation. First, we confirm whether the normalized velocity distribution function of the evaporation molecules obeys the normalized Maxwellian distribution (Eq. (1.32)), which is the premise of the hypothesis of the spontaneous evaporation. Next, we discuss the correspondence of the hypothesis of the spontaneous evaporation with α_e and α_c obtained in Chapter 3 by examining the mass fluxes of evaporation and condensation molecules in both the vapor–liquid equilibrium and net evaporation/condensation cases. In this way, we can find the relation among α_e, α_c obtained in Chapter 3, and the molecular processes illustrated in Fig. 1.1.

4.1 Spontaneous evaporation

We preliminarily explain a hypothesis of the spontaneous evaporation proposed by Ishiyama *et al.* [33, 44]. The hypothesis of the spontaneous evaporation is an assumption that the evaporation molecules have only the information of liquid. We call such molecules the spontaneous evaporation molecules. Ishiyama *et al.* [33, 44] applied this assumption to the single component monatomic molecules (argon) and polyatomic molecules (water and methanol). We here consider only this assumption on the monatomic molecules. We examine the following KBC in which we set to $\mathcal{A} = \alpha_{\rm e}\rho^* + (1-\alpha_{\rm c})\sigma$ in the generalized KBC (Eq. (2.1)).

$$f_{\rm out} = [\alpha_{\rm e}\rho^* + (1-\alpha_{\rm c})\sigma]\hat{f}^*, \tag{4.1}$$

where $\hat{f}^*$ is assumed the normalized Maxwellian distribution (Eq. (2.2)). According to Ishiyama *et al.* [33], $\alpha_{\rm e}\rho^*\hat{f}^*$ in Eq. (4.1) is defined as the velocity distribution function of the spontaneous evaporation molecules, $f^*_{\rm evap}$, and $(1-\alpha_{\rm c})\sigma\hat{f}^*$ in Eq. (4.1) is defined as the velocity distribution function of the reflection molecules, $f_{\rm ref}$. These definitions are not obvious because the division of $\hat{f}^*$ is arbitrary in Eq. (4.1). The velocity distribution functions of the spontaneous evaporation and reflection molecules support the molecular processes illustrated in Fig. 1.1.

By considering the molecular processes, the mass fluxes composed of molecules having $\xi_z > 0$ at the vapor–liquid interface satisfy the following relation.

$$J_{\rm out} = J^*_{\rm evap} + J_{\rm ref}, \tag{4.2}$$

where $J_{\rm out} = \int_{\xi_z>0}\xi_z f_{\rm out}{\rm d}\boldsymbol{\xi}$, $J^*_{\rm evap}$ indicates the spontaneous evaporation mass flux obtained as $J^*_{\rm evap} = \int_{\xi_z>0}\xi_z f^*_{\rm evap}{\rm d}\boldsymbol{\xi}$, and $J_{\rm ref}$ indicates the reflection mass flux obtained as $J_{\rm ref} = \int_{\xi_z>0}\xi_z f_{\rm ref}{\rm d}\boldsymbol{\xi}$. In the same way, the mass fluxes composed of

molecules having $\xi_z < 0$ at the vapor–liquid interface satisfy the following relation.

$$J_{\mathrm{coll}} = J_{\mathrm{cond}} + J_{\mathrm{ref}}, \tag{4.3}$$

where $J_{\mathrm{coll}} = \int_{\xi_z<0} \xi_z f_{\mathrm{coll}} \mathrm{d}\boldsymbol{\xi}$, and J_{cond} indicates the condensation mass flux obtained from the velocity distribution function of condensation molecules, f_{cond}, as $J_{\mathrm{cond}} = \int_{\xi_z<0} \xi_z f_{\mathrm{cond}} \mathrm{d}\boldsymbol{\xi}$. α_{e} and α_{c} according to the hypothesis of the spontaneous evaporation are defined based on these molecular mass fluxes.

As explained above, since the normalized velocity distribution function of f^*_{evap} has to be the normalized Maxwellian distribution (Eq. (2.2)), J^*_{evap} can be obtained as

$$J^*_{\mathrm{evap}} = \int_{\xi_z>0} \xi_z f^*_{\mathrm{evap}} \mathrm{d}\boldsymbol{\xi} = \alpha_{\mathrm{e}} \rho^* \sqrt{\frac{RT_{\mathrm{L}}}{2\pi}}. \tag{4.4}$$

With the use of J^*_{evap}, the definition of α_{e} can be given as

$$\alpha_{\mathrm{e}} = \frac{J^*_{\mathrm{evap}}}{\rho^* \sqrt{RT_{\mathrm{L}}/(2\pi)}} = \frac{J^*_{\mathrm{evap}}}{J^*_{\mathrm{out}}}. \tag{4.5}$$

In this definition of α_{e}, J^*_{evap} depends only on the liquid temperature. This definition is synonymous with specifying $\mathcal{A}_0(T_{\mathrm{L}}) = J^*_{\mathrm{evap}}/\sqrt{RT_{\mathrm{L}}/(2\pi)}$ in Eq. (1.42).

If the normalized velocity distribution function of f^*_{evap} is the normalized Maxwellian distribution, that of f_{ref} is also the same, and J_{ref} can be obtained as

$$J_{\mathrm{ref}} = \int_{\xi_z>0} \xi_z f_{\mathrm{ref}} \mathrm{d}\boldsymbol{\xi} = (1-\alpha_{\mathrm{c}}) \sigma \sqrt{\frac{RT_{\mathrm{L}}}{2\pi}}. \tag{4.6}$$

Substituting Eq. (4.6) into Eq. (4.3), we get the definition of α_{c} as follows:

$$\alpha_{\mathrm{c}} = \frac{J_{\mathrm{cond}}}{\sigma \sqrt{RT_{\mathrm{L}}/(2\pi)}} = \frac{J_{\mathrm{cond}}}{J_{\mathrm{coll}}}. \tag{4.7}$$

In vapor–liquid equilibrium, $\sigma = \rho^*$ and $J_{\mathrm{cond}} = J^*_{\mathrm{evap}}$, and thus α_{c} is identical to α_{e}

and is defined as $J^*_{\mathrm{evap}}/J^*_{\mathrm{out}}$.

As is clear from Eqs. (4.2) and (4.3), the mass fluxes related to the molecular processes (J^*_{evap}, J_{ref}, and J_{cond}) can be determined if one of them is uniquely determined, and then α_{e} and α_{c} can be estimated from Eqs. (4.5) and (4.7). An idea to distinguish these mass fluxes is a virtual vacuum simulation [26, 33], which realizes a situation that all vapor molecules near the vapor–liquid interface have outgoing velocities from liquid ($\xi_z > 0$) by eliminating the molecules colliding with the vapor–liquid interface. By this simulation, we can obtain the spontaneous evaporation flux J^*_{evap}, which depends only on the liquid temperature. Ishiyama *et al.* [33] estimated J^*_{evap} by the virtual vacuum simulation to obtain α_{e}. They also obtained f^*_{evap} from this simulation. Then, Ishiyama *et al.* [34] estimated J_{coll} by the net evaporation and condensation simulation to obtain α_{c}.

The results of the virtual vacuum simulation [33] indicated that the normalized velocity distribution function of f^*_{evap} obeys the normalized Maxwellian distribution function only at the low liquid temperature near the triple point. Zhakhovskii and Anisimov [26] also proposed the virtual vacuum simulation, and they pointed out that the normalized Maxwellian distribution can be adopted for the KBC only in the case of lower vapor density with the relatively low liquid temperature. Also, the density profile during the virtual vacuum simulation differs markedly from that of vapor–liquid equilibrium when the liquid temperature becomes relatively high [26, 33]. These results implied that the virtual vacuum simulation is inappropriate in the case of the relatively high liquid temperature.

In this thesis, we utilize a new method to estimate f^*_{evap} and J^*_{evap}. In this method, we set the two boundaries between liquid and vapor, which are the control surfaces, and count the number of molecules which pass through these two boundaries. Hereafter, we call this method the *two-boundary method*. The original two-boundary method is proposed by Meland *et al.* [27]. This method has a problem that the boundary on the liquid side can not be uniquely determined. In contrast,

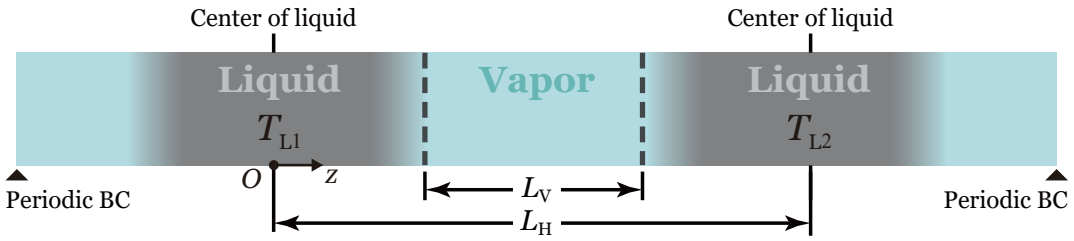

Figure 4.1: Schematic of the simulation system; T_{L1} and T_{L2} indicate the temperatures of two liquids ($T_{L1} > T_{L2}$), L_H indicates the half-length of the simulation system, and L_V indicates the length of the vapor phase.

Kobayashi *et al.* [30, 91] proposed a procedure to determine the liquid boundary according to the hypothesis of the spontaneous evaporation. We call this method the improved two-boundary method by contrast with the original one. Kobayashi *et al.* [30, 91] applied the improved two-boundary method only at the low liquid temperature. However, since the improved two-boundary method has fewer artificial operations than the virtual vacuum simulation, we expect that this method can be applied to the high liquid temperature. We detail the improved two-boundary method in the next section.

4.2 Simulation settings

As explained in Chapter 2 (Section 2.1.2), we simulate the system composed of vapor between two parallel liquid slabs (two-surface problem) in the one-dimensional space and the three-dimensional molecular velocity space. The schematic of the simulation system is shown in Fig. 4.1; T_{L1} and T_{L2} indicate the temperatures of two liquids ($T_{L1} > T_{L2}$), L_H indicates the half-length of the simulation system, and L_V indicates the length of the vapor phase. As a consequence of the temperature difference between two liquids, net evaporation occurs at the vapor–liquid interface on the high-temperature side, and net condensation occurs at the vapor–liquid interface on the low-temperature side.

We simulate various cases of net evaporation and condensation by varying the

temperature difference between two liquids; one of liquid temperature is fixed as a reference, and the other is varied. Three cases of reference liquid temperature, $T_{\mathrm{L}}/T_{\mathrm{c}}$, are set to 0.60, 0.64, and 0.68. In the manner explained in Chapter 3 (3.1), we perform the simulations under 21 cases of the temperature differences. All cases of the temperature differences and the reference values of the mean free path ℓ_0 at the mean temperature of two liquids are summarized in Table 4.1. Since the degree of net evaporation/condensation under each temperature difference is in the applicable range of the normalized Maxwellian distribution obtained in Chapter 3 ($0.5 \lesssim \sigma/\rho^* \lesssim 2.3$), we assume that the normalized velocity distribution function of the KBC is the normalized Maxwellian distribution. The cell size Δz is set to $0.2a$, the time step Δt is set to $0.001(\sqrt{2RT_{\mathrm{c}}}/a) \approx 0.2\bar{\mu}_{\mathrm{L}}^{-1}$, and the half-length of the simulation system L_{H} is set to $40a$.

4.2.1 Improved two-boundary method

Let us explain the improved two-boundary method. In this method, we set the two boundaries between liquid and vapor, which are the control surfaces, and count the number of molecules which pass through these two boundaries. Hereafter, we refer to these two boundaries as the *liquid boundary* and the *vapor boundary*. The schematic of the two boundaries in this simulation system is shown in Fig. 4.2; the dashed lines denote the liquid and vapor boundaries. The positions of the liquid and vapor boundaries are defined in the latter part of this section. As illustrated in Fig. 4.2, the evaporation molecules are identified as molecules passing through

Table 4.1: The temperature differences between two liquids and the reference values of the mean free path at the mean temperature of two liquids.

#	$T_{\mathrm{L1}}/T_{\mathrm{c}}$	$T_{\mathrm{L2}}/T_{\mathrm{c}}$	ℓ_0/a	#	$T_{\mathrm{L1}}/T_{\mathrm{c}}$	$T_{\mathrm{L2}}/T_{\mathrm{c}}$	ℓ_0/a	#	$T_{\mathrm{L1}}/T_{\mathrm{c}}$	$T_{\mathrm{L2}}/T_{\mathrm{c}}$	ℓ_0/a
1	0.56	0.60	58.7	8	0.62	0.66	27.4	15	0.64	0.68	22.0
2	0.58	0.60	51.1	9	0.64	0.66	24.5	16	0.66	0.68	19.8
3	0.60	0.60	44.7	10	0.66	0.66	22.0	17	0.68	0.68	17.8
4	0.60	0.62	39.3	11	0.66	0.68	19.8	18	0.68	0.70	16.1
5	0.60	0.64	34.7	12	0.66	0.70	17.8	19	0.68	0.72	14.7
6	0.60	0.66	30.8	13	0.66	0.72	16.1	20	0.68	0.74	13.3
7	0.60	0.68	27.4	14	0.66	0.74	14.7	21	0.68	0.76	12.2

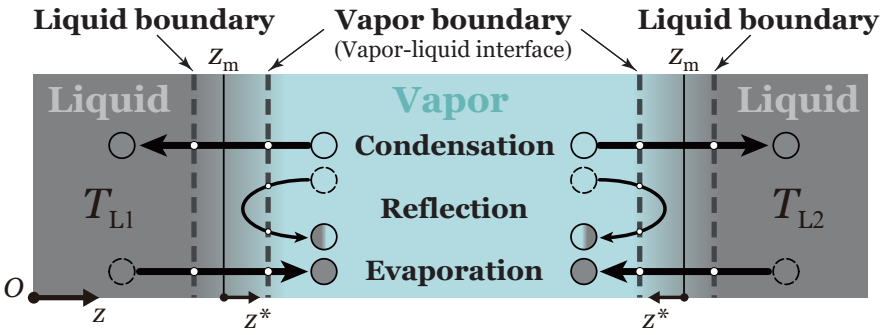

Figure 4.2: Schematic of the two boundaries in the present simulation system; the dashed lines denote the liquid and vapor boundaries.

the liquid boundary to the vapor boundary, the reflection molecules are identified as molecules passing through the vapor boundary twice without passing through the liquid boundary, and the condensation molecules are identified as molecules passing through the vapor boundary to the liquid boundary. The molecular mass fluxes related to these molecular processes obviously satisfy the relation Eqs. (4.2) and (4.3) if we regard the evaporation molecules as the spontaneous evaporation molecules.

In this simulation, we label all molecules in the simulation system and count the number of the evaporation, reflection, or condensation molecules at each time step. We hereby can estimate each molecular mass fluxes as

$$\frac{J}{\rho_c\sqrt{2RT_c}} = \frac{1}{N_s}\sum_{N_s}\frac{\Delta z \Delta N}{\Delta t N_0}, \tag{4.8}$$

where N_s indicates the number of counting molecules, ΔN indicates the number of the evaporation, reflection, or condensation molecules during Δt, N_0 indicates the number of molecules in Δz at the critical point. In the present simulation, N_s and N_0 are set to 500000 and 3000, respectively.

Then, we explain the positions of the liquid and vapor boundaries. We set the center of the density transition layer z_m and the thickness of the density transition layer δ obtained from Eq. (2.71) in vapor–liquid equilibrium as the reference to determine the liquid and vapor boundaries. For convenience, we utilize a new spatial

coordinate z^*:

$$z^* = \frac{z - z_{\mathrm{m}}}{\delta}. \tag{4.9}$$

The vapor boundary is equivalent to the vapor–liquid interface as illustrated in Fig. 4.2. According to the positions of the vapor–liquid interface as explained in Chapter 3 (Section 3.1), we determine the ideal gas region where the density of vapor–liquid equilibrium obeys the Clausius–Clapeyron equation and define the end of the ideal gas region as the vapor–liquid interface. In this simulation, the position of the vapor–liquid interface is set to $z^* = 2.5$. This definition of the vapor boundary is similar to that proposed by Meland *et al.* [27] in the original two-boundary method. Alternatively, Ishiyama *et al.* [33] proposed that the position of the vapor–liquid interface has to be located in $2.0 \lesssim z^*$ where the vapor phase is well developed. Kobayashi *et al.* [30, 91] set the position of the vapor boundary to $z^* = 3.0$ in accordance with Ishiyama *et al.* [33] in the improved two-boundary method. The methods for determining the vapor boundary have some differences between studies, but the positions can be regarded as almost the same.

In contrast with the vapor boundary, the liquid boundary has no condition that should satisfy. In the original two-boundary method, Meland *et al.* [27] stated that "Lacking any better criterion, the liquid boundary is here defined from a similar construction" and defined the position of the liquid boundary by the analogy to the definition of shock wave thickness. Kobayashi *et al.* [30, 91] pointed out that the mass fluxed calculated by the original two-boundary method changes with the position of the liquid boundary, but they took advantage of this ambiguity in the improved two-boundary method.

To determine the position of the liquid boundary, Kobayashi *et al.* [91] applied the two-boundary method in both the vapor–liquid equilibrium and the virtual vacuum simulations for argon at 85K. The temperature 85K is near the triple point of argon, in which case the virtual vacuum simulation is appropriate. The schematics of both

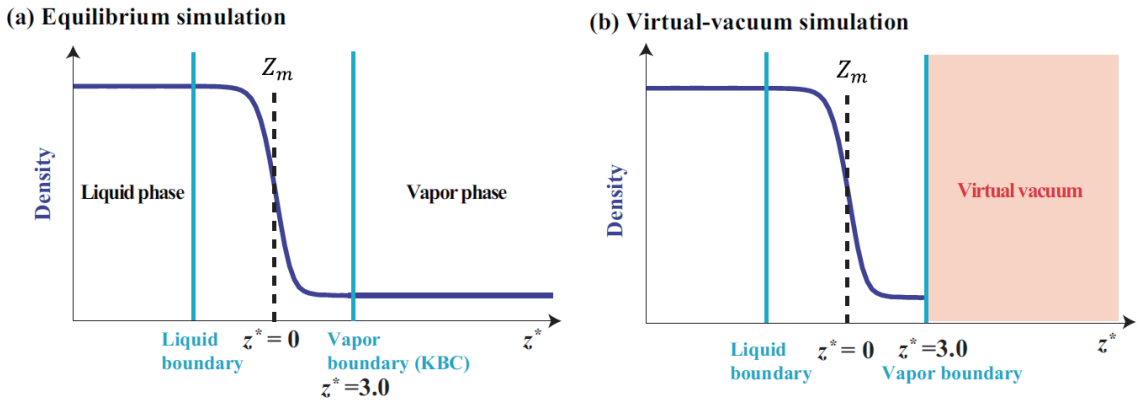

Figure 4.3: Schematic of (a) the vapor–liquid equilibrium simulation and (b) the virtual vacuum simulation with the liquid and vapor boundaries proposed by Kobayashi *et al.* [91].

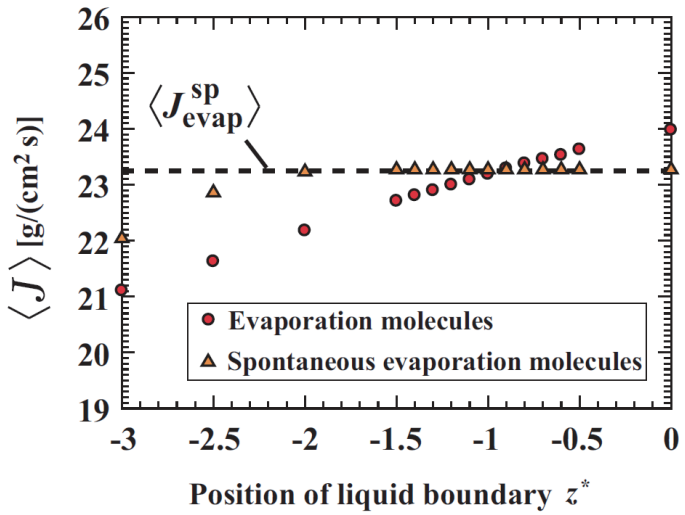

Figure 4.4: Evaporation and spontaneous evaporation molecular mass fluxes at the vapor boundary proposed by Kobayashi *et al.* [91]; the abscissa represents the spatial coordinate defined by $z^* = (z - z_m)/\delta$, and the ordinate represents the time averaged molecular mass flux.

simulations with the liquid and vapor boundaries are shown in Fig. 4.3. In both two simulations, the position of the vapor boundary is set to $z^* = 3.0$, and that of the liquid boundary is varied within the range $-3.0 \leq z^* \leq 0$.

Figure 4.4 shows the results of the vapor–liquid equilibrium and the virtual vacuum simulations; the abscissa represents the spatial coordinate defined by Eq. (4.9), and the ordinate represents the time-averaged molecular mass flux. In Fig. 4.4, the triangles denote the spontaneous evaporation mass flux obtained from the virtual vacuum simulation with the liquid and vapor boundaries, and the circles denote the mass flux obtained from the vapor–liquid equilibrium simulation with the liquid and vapor boundaries. As can be seen in Fig. 4.4, the results of these two simulations are crossed at $z^* \approx -1.0$. On the basis of this result, Kobayashi *et al.* [30] suggested that the spontaneous evaporation mass flux J^*_{evap} can be obtained from the vapor–liquid equilibrium simulation by setting the position of the liquid boundary to $z^* \approx -1.0$. According to this result, we also set to this position as the liquid boundary.

4.2.2 Initial condition

In this simulation, for the initial condition, we set to the positions and the velocities of molecules when the simulation, which started from the settings explained in Chapter 3 (Section 3.1), reaches the steady state. In the initial condition, we set the liquid and vapor boundaries and label all molecules in the system. To track all molecules, we perform an idling simulation until the molecules that in the region between the liquid and vapor boundary at the initial condition passing through either boundary. After this idling simulation, we start to count the number of molecules and calculate the velocity distribution function and the mass flux.

4.2.3 Boundary condition

We give the boundary condition in the same way as in Chapter 2 (Section 2.4.1). As illustrated in Fig. 4.1, we impose the periodic boundary condition at both ends of the

system; the molecules that flow out from one boundary after advection are inserted from the other boundary. By imposing this boundary condition, the simulation system as shown in Fig. 4.1 can be regarded as symmetric with respect to each center of liquid. In the following, we show the results only in half the simulation system.

4.2.4 Other settings

Velocity scaling method

We impose the thermostat in the same way as in Chapter 2 (Section 2.4.1). We apply the velocity scaling method [76] to keep the constant temperature. The temperature modification factor Φ in Eq. (2.70) is estimated in each cell at each time step. The region where the thermostat is imposed is defined as $3.0a$ from each z_{m} toward each liquid, where z_{m} indicates the position of the center of the 10–90 thickness density transition layer in vapor–liquid equilibrium (Eq. (2.71)); the length of the thermostat region is approximately $\pm 3.0a$ from the center of liquid. Note that since the position of z_{m} depends on the temperature, the length of the thermostat region slightly varies with the temperature.

Two boundaries tracking method

In this simulation, we label all molecules and track these molecules at each time step. Hence, it is hard to realize the steady net evaporation/condensation system by the shifting method, which modifies the positions of molecules at each time step, as explained in Chapter 3 (Section 3.1). We realize a quasi-steady system by changing the positions of the liquid and vapor boundaries at each time step. Since the liquid slab diminishes/grows with time due to net evaporation/condensation, we subtracted the offset amount from each z_{m} at each simulation time step, where the

offset amount Δz_{m} is estimated by

$$\Delta z_{\mathrm{m}} = \frac{J_{\mathrm{out}} - J_{\mathrm{coll}}}{\rho_{\mathrm{L}}} \Delta t, \tag{4.10}$$

where $J_{\mathrm{out}} > J_{\mathrm{coll}}$ at the vapor–liquid interface with net evaporation, whereas $J_{\mathrm{out}} < J_{\mathrm{coll}}$ at the vapor–liquid interface with net condensation; hence, the positions of z_{m} in both cases move toward the negative z-direction. Since the positions of the liquid and vapor boundaries are based on z_{m}, we can determine the position of these two boundaries at each time step.

4.3 Results and discussion

4.3.1 Modification of formulated mass flux relation

As a preparation, we modify the formulated mass flux relation (Eq. (3.14)) as preparation for comparing α_{e} and α_{c} defined by Eqs. (4.5) and (4.7) with those obtained in Chapter 3. According to the hypothesis of the spontaneous evaporation, the spontaneous evaporation mass flux J^*_{evap} depends only on the liquid temperature, regardless of the value of J_{coll}. To obtain the expression of J^*_{evap} from the formulated mass flux relation (Eq. (3.14)), we consider a situation that J_{coll} is set to zero at the vapor–liquid interface. This situation is equivalent to that in the virtual vacuum simulation. When $J_{\mathrm{coll}} = 0$, Eq. (3.14) becomes

$$\frac{\rho v_z}{J^*_{\mathrm{out}}} = \beta(T_{\mathrm{L}}). \tag{4.11}$$

From Eqs. (4.2) and (4.3), we can obtain the relation $\rho v_z = J_{\mathrm{out}} - J_{\mathrm{coll}} = J^*_{\mathrm{evap}} - J_{\mathrm{cond}}$. Furthermore, since J_{ref} obviously becomes zero when J_{coll} is set to zero,

Eq. (3.14) becomes

$$\frac{J^*_{\mathrm{evap}}}{J^*_{\mathrm{out}}} = \beta(T_{\mathrm{L}}). \tag{4.12}$$

The left-hand side of Eq. (4.12) is equivalent to the definition of α_{e} according to the hypothesis of the spontaneous evaporation (Eq. (4.5)). From the result in Chapter 3, we obtain the relation $\alpha_{\mathrm{e}} = \alpha_{\mathrm{c}} = \beta(T_{\mathrm{L}})$; thus, the following relation can be obtained with the use of the definition of α_{c} according to the spontaneous evaporation (Eq. (4.7)).

$$\frac{J_{\mathrm{cond}}}{J_{\mathrm{coll}}} = \beta(T_{\mathrm{L}}). \tag{4.13}$$

On the basis of Eqs. (4.12) and (4.13), we can estimate J^*_{evap} and J_{cond} according to Eq. (3.14) as

$$J^*_{\mathrm{evap}} = J^*_{\mathrm{out}}\beta(T_{\mathrm{L}}), \qquad J_{\mathrm{cond}} = J_{\mathrm{coll}}\beta(T_{\mathrm{L}}). \tag{4.14}$$

We hereafter discuss J^*_{evap} and J_{cond} obtained from Eq. (4.14) and those calculated by the improved two-boundary method. Note that since J^*_{out} and J_{coll} in Eqs. (4.5) and (4.7) are given values, we can examine α_{e} and α_{c} by discussing J^*_{evap} and J_{cond}.

4.3.2 Velocity distribution function of evaporation molecules

In the following, we show the main results of this chapter. First, we confirm the normalized velocity distribution function of the evaporation molecules obtained from the improved two-boundary method. According to the hypothesis of the spontaneous evaporation, the normalized velocity distribution function of the evaporation molecules has to be the normalized Maxwellian distribution (Eq. (2.2)). However, the previous studies [26, 33] showed that the normalized velocity distribution function of the evaporation molecules obtained from the virtual vacuum simulation obeys

the normalized Maxwellian distribution only at the low liquid temperature near the triple point. Furthermore, the density profile during the virtual vacuum simulation differs markedly from that of vapor–liquid equilibrium when the liquid temperature becomes relatively high. In the improved two-boundary method, we do not have to mind the extraordinary density profile because we do not realize an artificial situation like the virtual vacuum simulation. In contrast, the normalized velocity distribution function of the evaporation molecules has to be examined, especially in the cases of net evaporation/condensation and the high liquid temperature.

The calculation procedure of the normalized velocity distribution function of the evaporation molecules by the improved two-boundary method is shown below. We set the upper and lower limits of the velocity space to $\zeta_i = -4$ and $\zeta_i = 4$, respectively, and divide this velocity space into 40 cells, where $\zeta_i = \xi_i/\sqrt{2RT_{\mathrm{L1}}}$ or $\zeta_i = \xi_i/\sqrt{2RT_{\mathrm{L2}}}$. We can obtain the velocity distribution function of the evaporation molecules by determining which cells the velocities of the evaporation molecules belongs to and counting the number of molecules.

Figure 4.5 shows the normalized velocity distribution function of the evaporation molecules in the case of the reference liquid temperature $T_{\mathrm{L}}/T_{\mathrm{c}} = 0.68$; the closed circles denote the normalized velocity distribution function of the evaporation molecules in vapor–liquid equilibrium, the open circles denote those in net evaporation and condensation, and the dashed lines denote the normalized Maxwellian distribution (Eq. (2.77)) in the tangential direction and that times ζ_i in the normal direction. In Fig. 4.5, we show only cases of vapor–liquid equilibrium, strongest net evaporation, and strongest net condensation at the highest reference liquid temperature in this simulation.

As can be seen in Fig. 4.5, the normalized velocity distribution function of the evaporation molecules in vapor–liquid equilibrium seems to agree with the normalized Maxwellian distribution, and those in net evaporation and condensation also seem to agree with the normalized Maxwellian. These results show that the premise

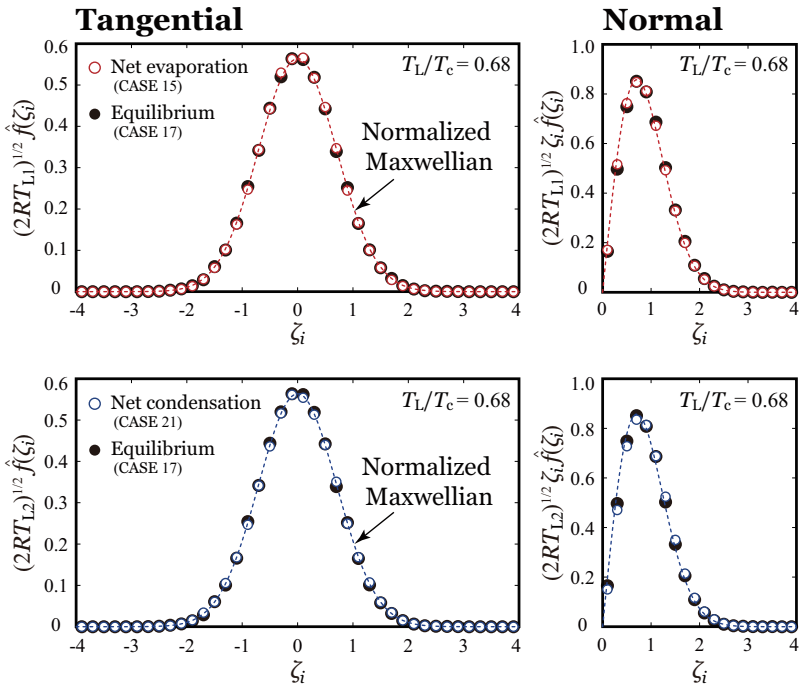

Figure 4.5: Normalized velocity distribution functions of the evaporation molecules in the cases of $T_{L1}/T_c = T_{L2}/T_c = 0.68$ (vapor–liquid equilibrium), $T_{L1}/T_c = 0.68$ and $T_{L2}/T_c = 0.64$ (net evaporation), and $T_{L1}/T_c = 0.76$ and $T_{L2}/T_c = 0.68$ (net condensation).

of the hypothesis of the spontaneous evaporation holds even in the case of the highest liquid temperature accompanied with net evaporation/condensation. On the basis of this result, we find that the velocity distribution function of the evaporation molecules calculated by the improved two-boundary method can be regarded as that of the spontaneous evaporation molecules $\hat{f}^*_{\mathrm{evap}}$. Consequently, the evaporation mass flux calculated by this method can also be regarded as that of the spontaneous evaporation molecules J^*_{evap}. In other words, these results indicate that the improved two-boundary method can be applied in the cases of the high liquid temperature.

4.3.3 Spontaneous evaporation and condensation mass fluxes

Vapor–liquid equilibrium

Next, we compare J^*_{evap} and J_{cond} obtained from Eq. (4.14) and those calculated by the improved two-boundary method in the vapor–liquid evaporation cases. Note

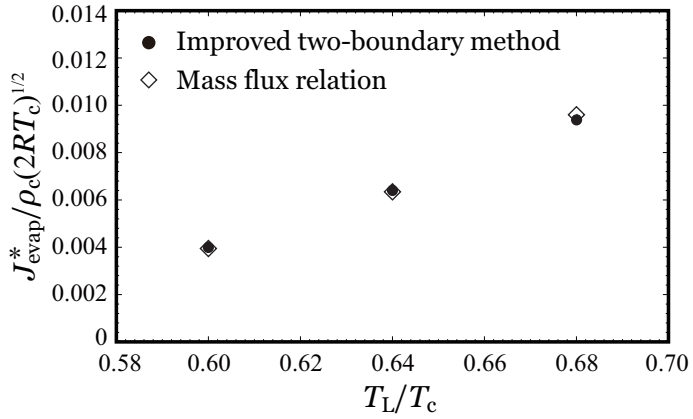

Figure 4.6: Spontaneous evaporation mass flux J^*_{evap} obtained from Eq. (4.14) and those calculated by the improved two-boundary method in vapor–liquid equilibrium; the abscissa and ordinate are normalized by the critical values.

that since $J_{\mathrm{cond}} = J^*_{\mathrm{evap}}$ in vapor–liquid equilibrium, we show only the result of J^*_{evap}. In Table 4.1, $T_{\mathrm{L1}}/T_{\mathrm{c}} = T_{\mathrm{L2}}/T_{\mathrm{c}} = 0.60$, $T_{\mathrm{L1}}/T_{\mathrm{c}} = T_{\mathrm{L2}}/T_{\mathrm{c}} = 0.64$, and $T_{\mathrm{L1}}/T_{\mathrm{c}} = T_{\mathrm{L2}}/T_{\mathrm{c}} = 0.68$ are the vapor–liqud equilibrium cases.

Figure 4.6 shows the spontaneous evaporation mass flux J^*_{evap}; the closed circles denote J^*_{evap} calculated by the improved two-boundary method in vapor–liquid equilibrium, and the open diamonds denote those obtained from Eq. (4.14). As can be seen in Fig. 4.6, J^*_{evap} increases with the increase in the liquid temperature. Also, we can find that J^*_{evap} obtained from two different methods show an excellent agreement, in which case the maximum deviation is approximately 2%. From this result, in vapor–liquid equilibrium, we conclude that $\beta(T_{\mathrm{L}})$ follows the definition of α_{e} according to the hypothesis of the spontaneous evaporation: $\alpha_{\mathrm{e}} = \alpha_{\mathrm{c}} = J^*_{\mathrm{evap}}/J^*_{\mathrm{out}}$.

Net evaporation and condensation

Next, we compare J^*_{evap} and J_{cond} obtained from Eq. (4.14) and those calculated by the improved two-boundary method in the net evaporation/condensation cases. Figure 4.7 shows the spontaneous evaporation mass flux J^*_{evap} and the condensation mass flux J_{cond}; the closed circles denote J^*_{evap} and J_{cond} calculated by the improved two-boundary method in net evaporation and condensation, and the dashed lines

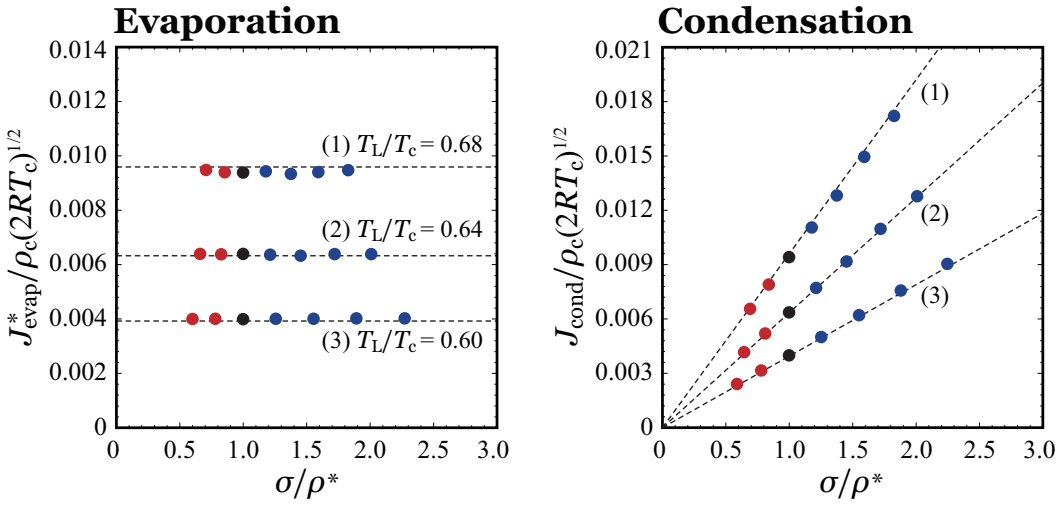

Figure 4.7: Spontaneous evaporation mass flux J^*_{evap} and the condensation mass flux J_{cond} obtained from Eq. (4.14) and those calculated by the improved two-boundary method in net evaporation and condensation; the abscissas represent the degree of net evaporation/condensation, and the ordinates are normalized by the critical values.

denote those obtained from Eq. (4.14).

As can be seen in Fig. 4.7, J^*_{evap} is constant at each reference liquid temperature, while J_{cond} increases with the increase in σ/ρ^* at each reference liquid temperature. It is most striking finding that J^*_{evap} and J_{cond} obtained from two different methods show good agreement even in the cases of net evaporation and condensation. From these results, we conclude that $\beta(T_{\mathrm{L}})$ follows the definitions of α_{e} and α_{c} according to the hypothesis of the spontaneous evaporation: $\alpha_{\mathrm{e}} = J^*_{\mathrm{evap}}/J^*_{\mathrm{out}}$ and $\alpha_{\mathrm{c}} = J_{\mathrm{cond}}/J_{\mathrm{coll}}$.

4.3.4 Comment on original two-boundary method

As a supplement, we comment on the result obtained from the original two-boundary method. Meland *et al.* [27] implied that α_{e} and α_{c} in net evaporation and condensation obtained from the original two-boundary method varies with the Mach number of the vapor flow. This result overtly contradicts the result shown in Fig. 4.7. This contradiction is due to the difference in the position of the liquid boundary between the original and improved two-boundary methods. Meland *et al.* [27] calculated the temperature at the liquid boundary as the liquid temperature and obtained α_{e}

and α_c by using this liquid temperature. The liquid boundary of the original two-boundary method is inside the density transition layer by approximately a compared to the improved one. It seems that this difference is very small, but the influence is considered to be large because the characteristics length scale at this position is a.

As shown in Fig.3.3, the temperature in the vicinity of the density transition layer has a spatial distribution, and this distribution varies with the degree of net evaporation/condensation even if we impose the thermostat under the same condition. Meland *et al.* [27] showed that the deviation between the temperature of bulk liquid, which is a region where the thermostat is imposed, and the temperature at the liquid boundary becomes approximately 8%. In contrast, we find that the deviation between the temperature of the thermostat region and temperature at the liquid boundary is reduced less than 2% by utilizing the improved two-boundary method. We conclude that it is one of the reasons why we can obtain such clear results shown in Fig. 4.7.

4.4 Summary

In Chapter 3, we found a pair of α_e and α_c defined by Eq. (1.42) at each liquid temperature. In this chapter, we considered the physical meaning of α_e and α_c obtained in Chapter 3. To determine α_e and α_c uniquely, we have to clarify the definitions of the molecular processes illustrated in Fig. 1.1. Although this definition has not been clarified, if we assume a certain condition, these molecular processes can be distinguished. We here consider a hypothesis of the spontaneous evaporation [33, 44]. According to this hypothesis, α_e and α_c are defined by the mass fluxes related to the molecular processes, such as J^*_{evap} and J_{cond}. We calculated J^*_{evap} and J_{cond} by the improved two-boundary method proposed by Kobayashi et al. [30,91] to examine α_e and α_c according to the hypothesis of the spontaneous evaporation. As a preparation, we modified the formulated mass flux relation (Eq. (3.14)) to obtain the expressions of J^*_{evap} and J_{cond} by using $\beta(T_L)$ (Eq. (4.14)).

First, we confirmed whether the normalized velocity distribution function of the evaporation molecules obeys the normalized Maxwellian distribution (Eq. (2.2)), which is the premise of the hypothesis of the spontaneous evaporation. From the result, we found that the normalized velocity distribution function of the evaporation molecules in vapor–liquid equilibrium seems to agree with the normalized Maxwellian distribution, and those in net evaporation and condensation also seem to agree with the normalized Maxwellian (Fig. 4.5). These results showed that the premise of the hypothesis of the spontaneous evaporation holds even in the case of the highest liquid temperature accompanied with net evaporation/condensation.

Next, we discussed the correspondence of the hypothesis of the spontaneous evaporation with α_{e} and α_{c} obtained in Chapter 3 by comparing J^*_{evap} and J_{cond} obtained from Eq. (4.14) and those calculated by the improved two-boundary method. From the result, we found that J^*_{evap} and J_{cond} obtained from two different methods show an excellent agreement in both vapor–liquid equilibrium and net evaporation/condensation (Figs. 4.6 and 4.7). We concluded that $\beta(T_{\mathrm{L}})$ follows the definitions of α_{e} and α_{c} according to the hypothesis of the spontaneous evaporation: $\alpha_{\mathrm{e}} = \alpha_{\mathrm{c}} = J^*_{\mathrm{evap}}/J^*_{\mathrm{out}}$ in vapor–liquid equilibrium, while $\alpha_{\mathrm{e}} = J^*_{\mathrm{evap}}/J^*_{\mathrm{out}}$ and $\alpha_{\mathrm{c}} = J_{\mathrm{cond}}/J_{\mathrm{coll}}$ in net evaporation/condensation.

Let us summarize the significance of the results so far. In Chapter 3, we found that $\mathcal{A}_0(T_{\mathrm{L}})$ in Eq. (1.42) is identified as $\mathcal{B}(T_{\mathrm{L}}) = \rho^*\beta(T_{\mathrm{L}})$. In this chapter, we found that $\beta(T_{\mathrm{L}})$ follows the definitions of α_{e} and α_{c} according to the hypothesis of the spontaneous evaporation. On the basis of this result, the following definition of $\mathcal{A}_0(T_{\mathrm{L}})$ can be obtained.

$$\mathcal{A}_0(T_{\mathrm{L}}) = \mathcal{B}(T_{\mathrm{L}}) \equiv \frac{J^*_{\mathrm{evap}}}{\sqrt{RT_{\mathrm{L}}/(2\pi)}}. \tag{4.15}$$

Although this result includes some assumptions, we succeeded to clarify the relation between $\beta(T_{\mathrm{L}})$ and the molecular processes illustrated in Fig. 1.1 by specifying $\mathcal{A}_0(T_{\mathrm{L}})$.

Chapter

5

Validation of kinetic boundary condition

In this chapter, we verify the accuracy of α_{e} and α_{c} obtained in Chapter 3 and Chapter 4. We perform the EV-DSMC simulation for the different two vapor–liquid two-phase systems, which are distinct from that considered in the preceding chapters. First, in these two systems, we confirm whether the normalized velocity distribution function of the KBC obeys the normalized Maxwellian distribution (Eq. (2.2)). Next, we compare the macroscopic variables in vapor, namely, the velocity and the temperature, in these two systems obtained from the numerical simulation of the Boltzmann equation with the KBC (Eq. (3.19)), which is specified by $\alpha_{\mathrm{e}} = \alpha_{\mathrm{c}} = \beta(T_{\mathrm{L}})$, and those obtained from the EV-DSMC simulation. Since it has been pointed out that the KBC significantly affects the macroscopic variables in the numerical simulation of the Boltzmann equation [45–47], the proper specification of the KBC is critical. In other words, the KBC at the vapor–liquid interface with net evaporation/condensation is validated if and only if the macroscopic variables in vapor obtained from these two simulations accurately agree with each other. This simple validation method has often been performed in the molecular dynamics simulation [45, 46]. Finally, we compare the liquid temperature dependence of α_{e} and α_{c} in these two systems with those obtained in Chapter 3. In this way, we can verify whether α_{e} and α_{c} obtained in the preceding chapters depend on the simulation systems.

5.1 ES-BGK model Boltzmann equation

In this validation, we carry out the numerical simulation of the ES-BGK model Boltzmann equation (ES-BGK equation) [89] that is one of the models of the Boltzmann equation, which can fit an arbitrary Prandtl number; the Prandtl number of the hard-sphere molecules is Pr = 0.6607 [12]. This model is proven to hold the H-theorem [89]. The ES-BGK equation is written as

$$\frac{\partial f}{\partial t} + \boldsymbol{\xi} \cdot \frac{\partial f}{\partial \boldsymbol{x}} = \frac{p}{\kappa(1-\psi)}[G(f) - f], \tag{5.1}$$

where κ is the viscosity coefficient and ψ is the constant value used to fit the Prandtl number Pr:

$$\mathrm{Pr} = \frac{1}{1-\psi}. \tag{5.2}$$

The value of ψ is set as 1/2 in this simulation. $G(f)$ is written as

$$G(f) = \frac{\rho}{\sqrt{\det(2\pi\Upsilon_{ij})}} \exp\left(-\frac{1}{2}(\xi_i - v_i)\Upsilon_{ij}^{-1}(\xi_j - v_j)\right), \tag{5.3}$$

where Υ_{ij} is defined as

$$\Upsilon_{ij} = (1-\psi)RT\delta_{ij} + \psi\Theta_{ij}, \tag{5.4}$$

where δ_{ij} is the Kronecker's delta, and $\rho\Theta_{ij}$ is the stress tensor.

The mean collision frequency of the ES-BGK equation is obtained as

$$\bar{\mu} = \frac{p}{\kappa} = \frac{\rho RT}{\kappa}. \tag{5.5}$$

The substitution of this mean collision frequency (Eq. (5.5)) and the average molec-

ular speed (Eq. (1.27) into the definition of the mean free path (Eq. (1.26)) yields

$$\ell = \sqrt{\frac{8}{\pi RT}}\frac{\kappa}{\rho}. \tag{5.6}$$

Equation (5.6) is the mean free path of the ES-BGK equation. Also, the mean free time of the ES-BGK equation is obtained as $\bar{\mu}^{-1}$.

In this numerical simulation, we discretize the time, the physical space, and the molecular velocity space and solve the ES-BGK equation by the finite difference method. The reference values for the nondimensionalization are the mean temperature of two liquids $T_0 = (T_{\mathrm{L1}} + T_{\mathrm{L2}})/2$, the mean free path ℓ_0 at T_0, and the mean free time $\bar{\mu}_0^{-1}$ at T_0. In the spatially one-dimensional problem, we can eliminate the molecular velocity components ξ_x and ξ_y by multiplying the velocity distribution function f by 1 or $\xi_x^2 + \xi_y^2$ and integrating over the whole space of ξ_x and ξ_y [92]:

$$\begin{cases} f_z(z, \xi_z, t) = \iint_{-\infty}^{\infty} f(z, \boldsymbol{\xi}, t)\mathrm{d}\xi_x\mathrm{d}\xi_y, \\ h_z(z, \xi_z, t) = \iint_{-\infty}^{\infty} (\xi_x^2 + \xi_y^2) f(z, \boldsymbol{\xi}, t)\mathrm{d}\xi_x\mathrm{d}\xi_y. \end{cases} \tag{5.7}$$

The numerical simulation is performed for the distribution functions f_z and h_z, and the macroscopic variables are given by

- Velocity v_z

$$v_z = \frac{1}{\rho}\int_{-\infty}^{\infty} \xi_z f_z \mathrm{d}\xi_z. \tag{5.8}$$

- Temperature T

$$T = \frac{1}{3\rho R}\Big(\int_{-\infty}^{\infty} (\xi_z - v_z)^2 f_z \mathrm{d}\xi_z + \int_{-\infty}^{\infty} h_z \mathrm{d}\xi_z\Big). \tag{5.9}$$

In the numerical simulation of the ES-BGK equation, 500 and 2000 cells are utilized for the velocity space and physical space, respectively (a total of one million

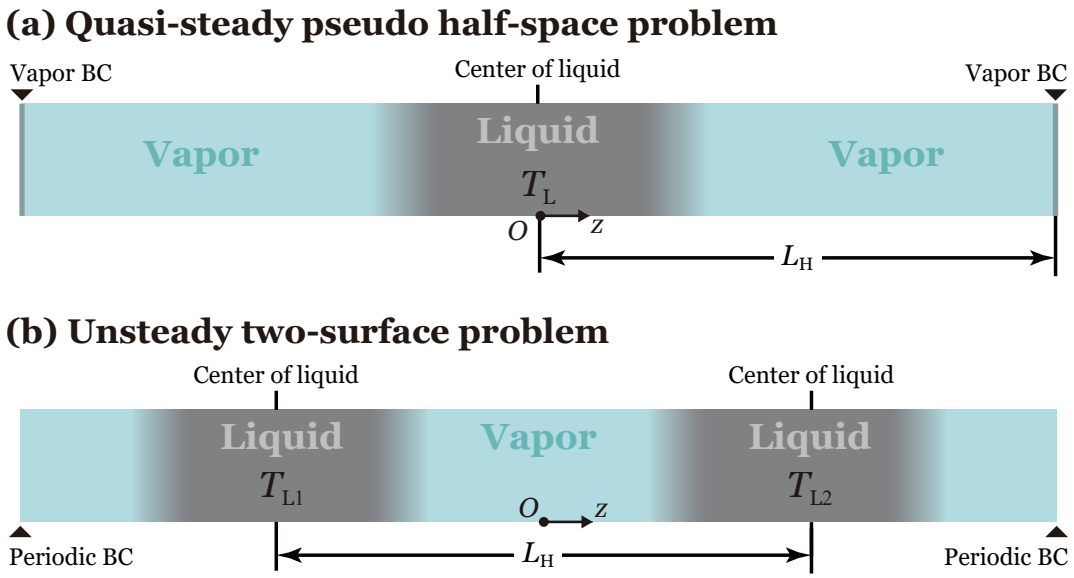

Figure 5.1: Schematic of the simulation system in the cases of (a) the quasi-steady pseudo half-space problem and (b) the unsteady two-surface problem; T_L indicates liquid temperature, $T_{\mathrm{L}1}$ and $T_{\mathrm{L}2}$ indicate the temperatures of two liquids ($T_{\mathrm{L}1} > T_{\mathrm{L}2}$ at initial condition), and L_H indicates the half-length of the simulation system.

cells). The cell size in the physical space Δz is set to $1.0 \times 10^{-4}\ell_0$, that in the molecular velocity space $\Delta\xi_z$ is set to $1.0 \times 10^{-2}\sqrt{2RT_0}$ near $\xi_z = 0$ and $1.0 \times 10^{-4}\sqrt{2RT_0}$ far from $\xi_z = 0$, and the time step Δt is set to $0.01\bar{\mu}_0^{-1}$. For the KBC at the vapor–liquid interface, we impose that proposed in Chapter 3 (Eq. (3.19)):

$$f_\mathrm{out} = [\beta(T_\mathrm{L})\rho^* + (1 - \beta(T_\mathrm{L}))\sigma]\hat{f}^*, \tag{3.19}$$

where $\alpha_\mathrm{e} = \alpha_\mathrm{c} = \beta(T_\mathrm{L})$ and the values of $\beta(T_\mathrm{L})$ are summarized in Tables 3.1–3.7.

5.2 Simulation settings

We simulate the two different systems composed of vapor and liquid in the one-dimensional space and the three-dimensional molecular velocity space, which are distinct from that considered in the preceding chapters. The schematics of one of the simulation system is shown in Fig. 5.1(a); T_L indicates the liquid temperature and L_H indicates the half-length of the simulation system. This system is imitated

the half-space problem which is well examined in molecular gas dynamics. In the half-space problem, we consider the infinite vapor region, but since it is impossible to realize this situation in the molecular simulation, we impose an arbitrary velocity distribution function at the end of vapor. We can realize the quasi-steady net evaporation or condensation system depending on the vapor boundary condition. Since we here consider the quasi-steady net evaporation/condensation, we call this problem the quasi-steady pseudo half-space problem. We simulate such a system in two cases of liquid temperature, $T_{\mathrm{L}}/T_{\mathrm{c}}$, 0.60 and 0.68. The cell size Δz is set to $0.2a$, the time step Δt is set to $0.001(\sqrt{2RT_{\mathrm{c}}}/a) \approx 0.2\bar{\mu}_{\mathrm{L}}^{-1}$, and the half-length of the simulation system L_{H} is set to $30a$. We calculate the macroscopic variables and the fluxes by taking 408 samples for each condition and averaging them over time.

The schematics of the other simulation system is shown in Fig. 5.1(b); T_{L1} and T_{L2} indicate the temperatures of two liquids ($T_{\mathrm{L1}} > T_{\mathrm{L2}}$), L_{H} indicates the half-length of the simulation system. This system is excluded the velocity scaling and the particle shifting in the system considered in Chapter 3. In this system, unsteady net evaporation/condensation accompanied by the temporal evolution of the liquid temperature occurs, and after a sufficient time, the system reaches vapor–liquid equilibrium at $T_{\mathrm{L1}} = T_{\mathrm{L2}}$. We call this problem the unsteady two-surface problem. We set the temperatures of two liquids to $T_{\mathrm{L1}}/T_{\mathrm{c}} = 0.72$ and $T_{\mathrm{L2}}/T_{\mathrm{c}} = 0.60$ at the initial state. The cell size Δz is set to $0.2a$, the time step Δt is set to $0.001(\sqrt{2RT_{\mathrm{c}}}/a) \approx 0.2\bar{\mu}_{\mathrm{L}}^{-1}$, and the half-length of the simulation system L_{H} is set to $40a$. We estimate the macroscopic variables by taking the ensemble average of 200 scenes which start from the different initial conditions. To obtain each initial condition having different microstates, we simulate the steady two-surface problem considered in Chapter 3.

5.2.1 Initial condition

Quasi-steady pseudo half-space problem

We give the initial condition in the same way as in Chapter 2 (Section 2.4.1). In this simulation, 1,200,000 molecules are arranged only around the center of each liquid where the liquid slab is to be formed. The total number of molecules decreases/increases with time according to the mass flux related to the vapor boundary condition. The velocities of molecules are determined by using the random sampling as

$$\xi_{z(i)} = \sqrt{-2RT_{\mathrm{L}} \ln r_{\mathrm{u}1}} \cos(2\pi r_{\mathrm{u}2}), \tag{5.10}$$

$$\xi_{x(i)} = \sqrt{-2RT_{\mathrm{L}} \ln r_{\mathrm{u}1}} \sin(2\pi r_{\mathrm{u}2}), \tag{5.11}$$

$$\xi_{y(i)} = \sqrt{-2RT_{\mathrm{L}} \ln r_{\mathrm{u}3}} \sin(2\pi r_{\mathrm{u}4}), \tag{5.12}$$

where $r_{\mathrm{u}1}$–$r_{\mathrm{u}4}$ indicate the different uniform random numbers.

Unsteady two-surface problem

As already explained, the unsteady simulation requires the initial conditions which have the different microstates. In this simulation, for the initial condition, we set to the positions and velocities of molecules when the simulation, which started from the settings explained in Chapter 3 (Section 3.1), reaches the steady state. After this simulation reaches the steady state, we extract the initial conditions for 200 scenes. Note that since the initial condition is required to have the different microstates, we extract these scenes with a sufficient time interval.

5.2.2 Boundary condition

Quasi-steady pseudo half-space problem

In this problem, we impose an arbitrary velocity distribution function at the end of vapor (Fig. 5.1(a)) to realize the quasi-steady net evaporation/condensation system. This method is based on that proposed by Ishiyama *et al.* [34] for the molecular dynamics simulation. We impose the following vapor boundary condition, f_{V}, at the end of vapor.

$$f_{\mathrm{V}} = \frac{\nu\rho^*}{(\sqrt{2\pi R\nu T_{\mathrm{L}}})^3} \exp\left(-\frac{\xi_i^2}{2R\nu T_{\mathrm{L}}}\right) \quad \text{for } \xi_z < 0, \tag{5.13}$$

where ν is a constant parameter ($\nu > 0$) and is set to 0.5 or 1.5; net evaporation occurs at the vapor–liquid interface in the case of $\nu = 0.5$, while net condensation occurs at the vapor–liquid interface in the case of $\nu = 1.5$. By imposing this boundary condition, the simulation system as shown in Fig. 5.1(a) can be regarded as symmetric with respect to the center of liquid. In the following, we show the results only in half the simulation system. Furthermore, the number of outgoing/incoming molecules are determined according to the following mass flux at the end of vapor.

$$J_{\mathrm{V}} = \nu\rho^* \sqrt{\frac{R\nu T_{\mathrm{L}}}{2\pi}}. \tag{5.14}$$

Unsteady two-surface problem

In this problem, we give the boundary condition in the same way as in Chapter 2 (Section 2.4.1). As illustrated in Fig. 5.1(b), we impose the periodic boundary condition at both ends of the system; the molecules that flow out from one boundary after advection are inserted from the other boundary. By imposing this boundary condition, the simulation system as shown in Fig. 5.1(a) can be regarded as symmetric with respect to each center of liquid. In the following, we show the results only in half the simulation system.

5.2.3 Other settings

Velocity scaling method

In the quasi-steady pseudo half-space problem, we impose the thermostat in the same way as in Chapter 2 (Section 2.4.1). We apply the velocity scaling method [76] to keep the constant temperature. The temperature modification factor Φ in Eq. (2.70) is estimated in each cell at each time step. The region where the thermostat is imposed is defined as $3.0a$ from each z_{m} toward each liquid, where z_{m} indicates the position of the center of the 10–90 thickness density transition layer in vapor–liquid equilibrium (Eq. (2.71)); the length of the thermostat region is approximately $\pm 3.0a$ from the center of liquid. Note that since the position of z_{m} depends on the temperature, the length of the thermostat region slightly varies with the temperature.

5.3 Results and discussion

5.3.1 Quasi-steady pseudo half-space problem

Macroscopic variables

We preliminarily show the results of the macroscopic variables obtained from the EV-DSMC simulation in the quasi-steady pseudo half-space problem. Figure 5.2 shows the density, velocity, and temperature fields obtained from the EV-DSMC simulation for the quasi-steady pseudo half-space problem; the thin solid lines denote the density fields, the bold solid lines denote the temperature fields, and dashed lines denote the velocity fields. In Fig. 5.2, the abscissas represent the spatial coordinate ($z' = (z - z_{\mathrm{m}})/a$). These macroscopic variables are obtained in the *sampling window* illustrated in Fig. 5.2. Also, the bold dashed lines denote the vapor–liquid interface. We determine the position of the vapor–liquid interface in the same way as in the preceding chapters and set to the position distanced 2.5δ from z_{m} to vapor. Since the liquid slab diminishes/grows with time due to net evaporation/condensation,

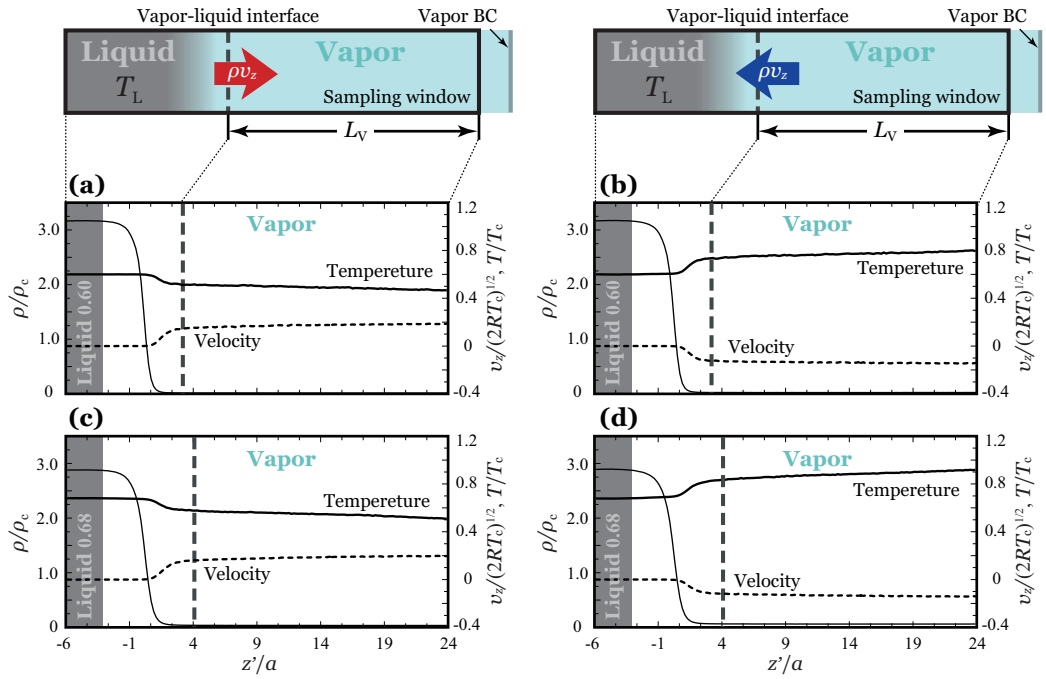

Figure 5.2: Spatial distributions of the density ρ, the velocity v_z, and the temperature T obtained from the EV-DSMC simulation for the quasi-steady pseudo half-space problem in the cases of (a) $T_L/T_c = 0.60$ and $\nu = 0.5$ (net evaporation), (b) $T_L/T_c = 0.60$ and $\nu = 1.5$ (net condensation), (c) $T_L/T_c = 0.68$ and $\nu = 0.5$ (net evaporation), and (d) $T_L/T_c = 0.68$ and $\nu = 1.5$ (net condensation); the abscissas represent the spatial coordinate ($z' = (z - z_m)/a$), and the ordinates are normalized by the critical values.

we subtracted the offset amount from z_m at each simulation time step according to Eq. (4.10). Note that the length between the right-side end of the sampling window and the end of vapor is smaller than the mean free path. Thus, we regard that the velocity distribution function at the right-side end of the sampling window is to be the same as the vapor boundary condition (Eq. (5.13)).

As can be seen in Fig. 5.2, a positive vapor velocity in the z-direction is induced by net evaporation (Figs. 5.2(a) and (c)), while a negative vapor velocity in the z-direction is induced by net condensation (Figs. 5.2(b) and (d)). Furthermore, we can see a drop in the temperature near the vapor–liquid interface due to net evaporation (Figs. 5.2(a) and (c)) and a rise in the temperature near the vapor–liquid interface due to net condensation (Figs. 5.2(b) and (d)). From these results, we confirm that net evaporation/condensation occurs according to the value ν in this simulation

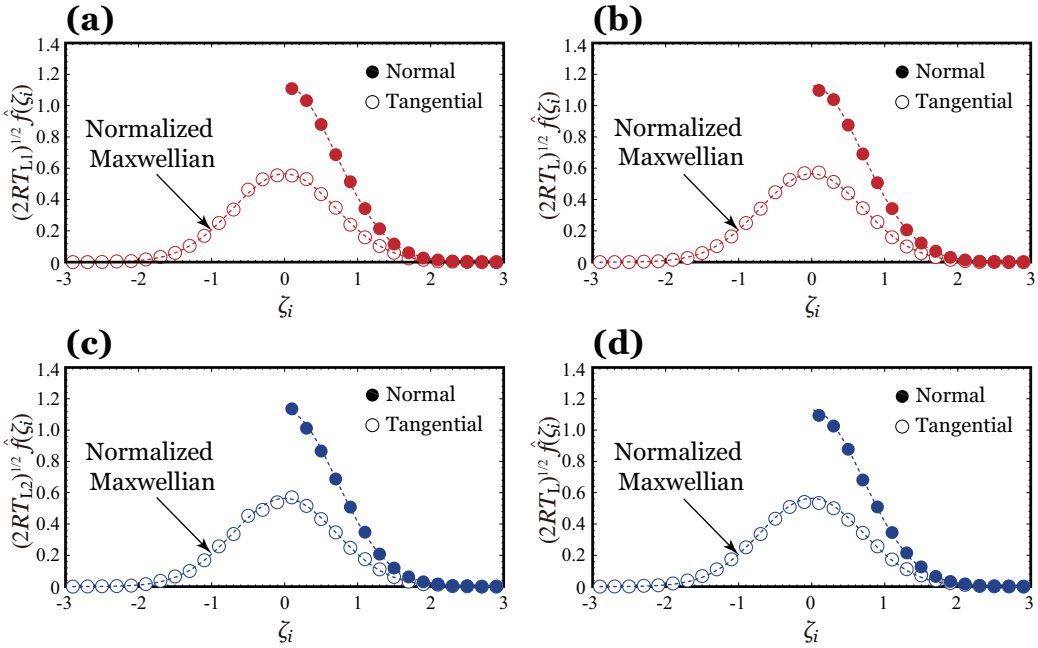

Figure 5.3: Normalized velocity distribution function of the KBC at the vapor–liquid interface obtained from the EV-DSMC simulation for the quasi-steady pseudo half-space problem in the cases of (a) $T_L/T_c = 0.60$ and $\nu = 0.5$ (net evaporation), (b) $T_L/T_c = 0.68$ and $\nu = 0.5$ (net evaporation), (c) $T_L/T_c = 0.60$ and $\nu = 1.5$ (net condensation), and (d) $T_L/T_c = 0.68$ and $\nu = 1.5$ (net condensation).

system.

Normalized velocity distribution function of kinetic boundary condition

In the following, we show the main results on the quasi-steady pseudo half-space problem. First, we examine the normalized velocity distribution function at the vapor–liquid interface composed of the outgoing molecules from there, that is, the normalized velocity distribution function of the KBC, in the quasi-steady pseudo half-space problem. The calculation procedure of the normalized velocity distribution function is the same as in Chapter 2 (Section 2.4.2). We set the upper and lower limits of the velocity space to $\zeta_i = -3$ and $\zeta_i = 3$, respectively, and divide this velocity space into 30 cells, where $\zeta_i = \xi_i/\sqrt{2RT_L}$. Figure 5.3 shows the normalized velocity distribution function of the KBC at the vapor–liquid interface. The closed circles denote the normalized velocity distribution function in the direction

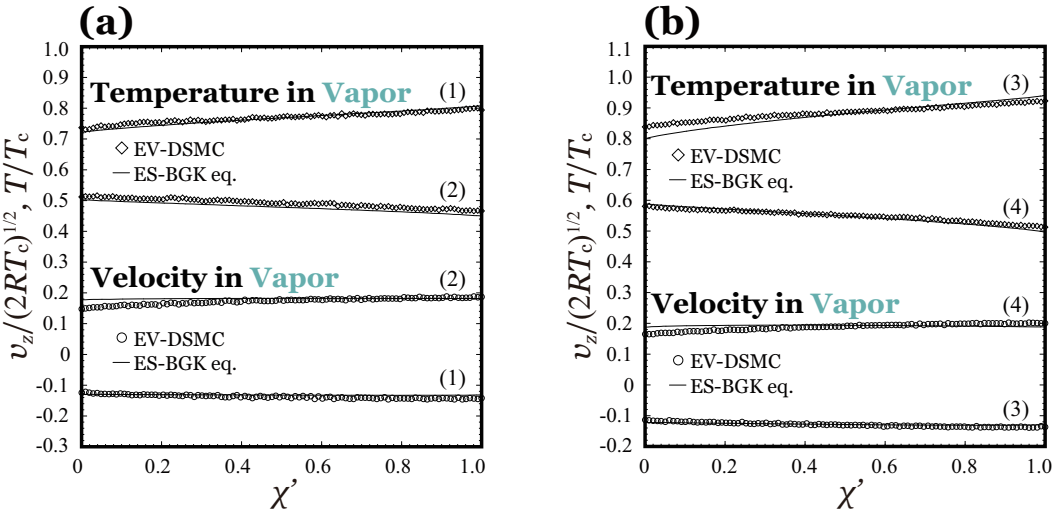

Figure 5.4: Comparison of the velocity v_z and the temperature T in vapor obtained from the EV-DSMC simulation and the numerical simulation of the ES-BGK equation for the quasi-steady pseudo half-space problem in the cases of (a) $T_\mathrm{L}/T_\mathrm{c} = 0.60$ ((1) $\nu = 1.5$ and (2) $\nu = 0.5$) and (b) $T_\mathrm{L}/T_\mathrm{c} = 0.68$ ((3) $\nu = 1.5$ and (4) $\nu = 0.5$); χ' is the spatial coordinate ($\chi' = 0$ indicates the vapor–liquid interface, and $\chi' = 1$ indicates the right-side end of the sampling window in Fig. 5.1), and the ordinates are normalized by the critical values.

normal to the vapor–liquid interface ($i = \mathrm{n}$), the open circles denote that in the tangential direction ($i = \mathrm{t}$), and the dashed lines denote the normalized Maxwellian distribution (Eq. (2.77)).

As can be seen in Fig. 5.3, the normalized velocity distribution function of the KBC more or less agrees with the normalized Maxwellian distribution (Eq. (2.77)) in all cases, especially in the direction normal to the vapor–liquid interface. For the tangential direction, especially in the case of $T_\mathrm{L}/T_\mathrm{c} = 0.68$, we can see that the temperature is slightly lower than T_L under net evaporation, while that is slightly higher than T_L under net condensation. This tendency has also been observed in Fig. 3.5. However, since these deviations are sufficiently small, we conclude that the normalized velocity distribution function of KBC can be assumed to be the normalized Maxwellian distribution in the quasi-steady pseudo half-space problem.

Comparison of velocity and temperature fields

Next, we compare the macroscopic variables in vapor, namely, the velocity and the temperature, in the quasi-steady pseudo half-space problem obtained from the numerical simulation of the ES-BGK equation and those obtained from the EV-DSMC simulation. In the numerical simulation of the ES-BGK equation, we consider a system composed of vapor between two boundaries; one of the boundaries is the vapor–liquid interface, and the other is the end of vapor. At the vapor–liquid interface, we imposed the KBC (Eq. (3.19)), which is specified by $\beta(T_{\mathrm{L}} = \alpha_{\mathrm{e}} = \alpha_{\mathrm{c}})$, while at the end of vapor, we imposed the vapor boundary condition f_{V} (Eq. (5.13)). The reference temperature in the numerical simulation of the ES-BGK equation is set to $T_0 = T_{\mathrm{L}}$. After the velocity distribution function f in vapor is obtained from the numerical simulation of the ES-BGK equation, the velocity and the temperature in vapor are estimated by Eqs. (5.8) and (5.9), respectively. Figure 5.4 shows the comparison between the velocity and the temperature in vapor obtained from the EV-DSMC simulation and the numerical simulation of the ES-BGK equation; the solid lines denote the results of the ES-BGK equation, and the open diamonds and circles denote those of the EV-DSMC simulation.

We can see that the velocity and temperature fields in vapor obtained from two different simulations are in almost agreement except for a region near the vapor–liquid interface in some cases. As shown in the former section, the normalized velocity distribution function of the KBC obeys almost the normalized Maxwellian distribution; hence, this is not the cause of the deviation of the macroscopic variables. There are two possible causes. The one is that the value of $\beta(T_{\mathrm{L}})$, which is set in the KBC in the numerical simulation of the ES-BGK equation, is inappropriate, in which case the KBC proposed in Chapter 3 is also inappropriate. As referred to the result in the latter section, the values of $\beta(T_{\mathrm{L}})$ in this simulation is almost identical with those obtained in Chapter 3, and thus that is unlikely the cause of the deviation of the macroscopic variables. The other is that the difference of the simulation system

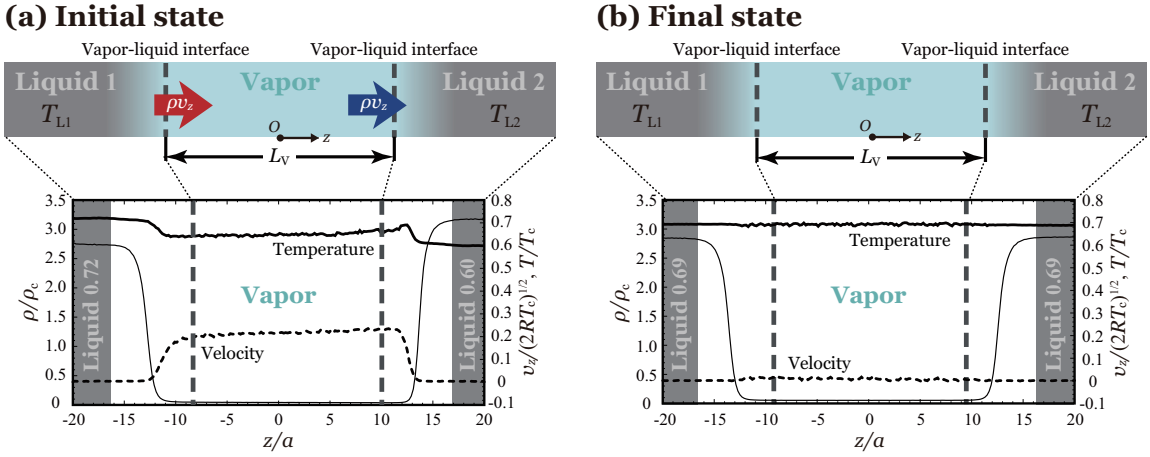

Figure 5.5: Spatial distributions of the density ρ, the velocity v_z, and the temperature T obtained from the EV-DSMC simulation for the unsteady two-surface problem at (a) the initial state and (b) the final state; the abscissa is normalized by the molecular diameter a, and the ordinates are normalized by the critical values.

between the EV-DSMC simulation and the numerical simulation of the ES-BGK equation. The quasi-steady simulation is carried out in the EV-DSMC simulation, whereas in the numerical simulation of the ES-BGK equation, the complete steady simulation is carried out. To realize the steady system by the molecular simulation, we have to perform some artificial operations, which makes it difficult to realize a complete steady system except in the case of vapor–liquid equilibrium. However, the deviation of the macroscopic variables obtained from these two simulations is sufficiently small except for a region near the vapor–liquid interface. From these results, we conclude that the KBC (Eq. (3.19)) is guaranteed to be applicable even in the quasi-steady pseudo half-space problem.

5.3.2 Unsteady two-surface problem

Macroscopic variables and mass flux

We preliminarily show the results of the macroscopic variables and the mass flux obtained from the EV-DSMC simulation in the unsteady two-surface problem. Figure 5.5 shows the density, velocity, and temperature fields obtained from the EV-

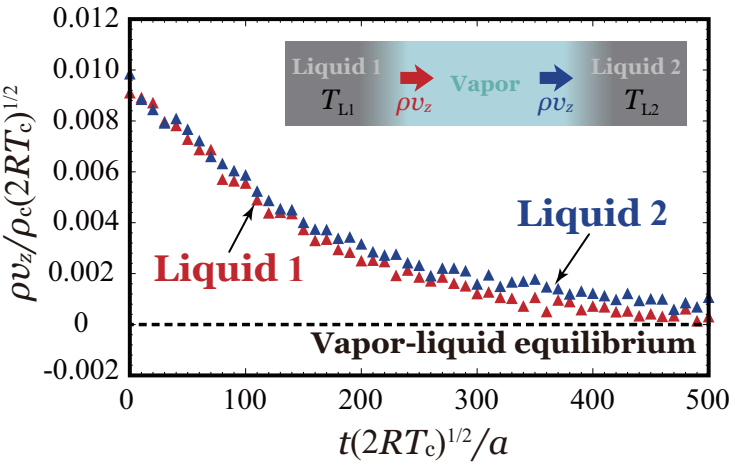

Figure 5.6: Temporal evolution of the mass flux at the vapor–liquid interface.

DSMC simulation for the unsteady two-surface problem at $t^* = t(a/\sqrt{2RT_c}) = 0$ (initial state) and $t^* = 500$ (final state). In Fig. 5.5, the thin solid lines denote the density fields, the bold solid lines denote the temperature fields, and the dashed lines denote the velocity fields. Also, the bold dashed lines denote the vapor–liquid interface. We determine the position of the vapor–liquid interface in the same way as in the preceding chapters and set to the position distanced 2.5δ from z_m to vapor. Hereafter, we refer to the left liquid slab at T_{L1} as *liquid 1* and the right liquid slab at T_{L2} as *liquid 2*.

As can be seen in Fig. 5.5(a), the velocity field in the z-direction takes a positive value, which is induced by net evaporation/condensation. Furthermore, we can see a drop in the temperature near the left vapor–liquid interface due to net evaporation, while a rise in the temperature near the right vapor–liquid interface due to net condensation. Also, in Fig. 5.5(b), the velocity field in the z-direction becomes zero in the whole simulation system, and the temperature field becomes uniform and constant ($T_{L1}/T_c = T_{L2}/T_c \approx 0.69$) as a consequence of the drop and rise in the temperatures accompanied with net evaporation and condensation.

Figure 5.6 shows the temporal evolution of the mass flux ρv_z at each vapor–liquid interface, where ρv_z is obtained as the difference between J_{out} and J_{coll}. As can be seen, ρv_z at each vapor–liquid interface decreases drastically until $t^* = 200$; after

that time, ρv_z at each vapor–liquid interface decreases gently and converges to zero eventually. These results indicate that the vapor–liquid two-phase system achieves vapor–liquid equilibrium at $t^* = 500$.

Normalized velocity distribution function of kinetic boundary condition

In the following, we show the main results on the unsteady two-surface problem. First, we examine the normalized velocity distribution function at the vapor–liquid interface composed of the outgoing molecules from there, that is, the normalized velocity distribution function of the KBC in the unsteady two-surface problem. As a preparation, we estimate a delay time caused by molecules traveling in the interface layer. As shown in Fig. 1.1, the interface layer has a finite thickness; hence, a delay time arises from molecules traveling in this finite interface layer in unsteady net evaporation/condensation. It is hereby not obvious that the normalized velocity distribution function of the KBC is the same as that in steady net evaporation and condensation. We determine the position of the boundary between the liquid and interface layer to specify the thickness of the interface layer, and then we estimate the delay time.

Figure 5.7 shows the temperature fields at the initial state ($t^* = 0$); the solid line denotes the temperature defined by Eq. (1.9), the dotted line is the temperature in the direction tangential to the vapor–liquid interface (x-direction) estimated as $T_x = \frac{1}{\rho R}\int \xi_x^2 f \mathrm{d}\boldsymbol{\xi}$, and the dashed line denotes that in the direction normal to the vapor–liquid interface (z-direction) estimated as $T_z = \frac{1}{\rho R}\int (\xi_z - v_z)^2 f \mathrm{d}\boldsymbol{\xi}$. It should be emphasized that the tendencies of these temperatures (T, T_x and T_z) are in good agreement with those obtained from the molecular dynamics simulation for the two-surface problem [45, 46]. These are important result showing the validity of the EV-DSMC simulation.

In Fig. 5.7, B_{L1} and B_{L2} denote the positions of the boundaries between each liquid and each interface layer. Their positions are defined distanced $3.0a$ from each

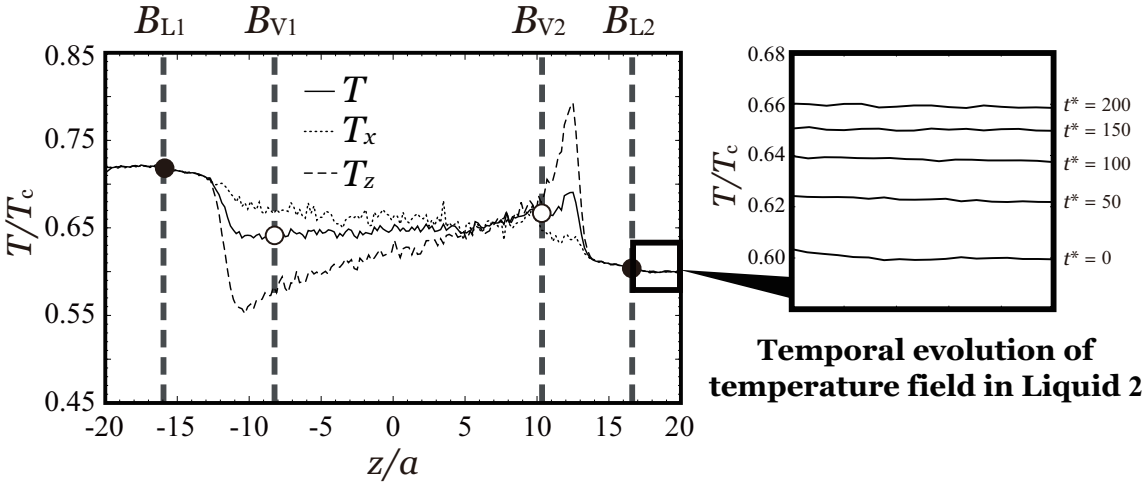

Figure 5.7: Spatial distributions of the various temperatures at $t^* = 0$; the abscissa is normalized by the molecular diameter a, and the ordinate is normalized by the critical temperature T_c. (enlarged view) Temporal evolution of the temperature field in liquid 2.

z_m to each liquid. As can be seen in Fig. 5.7, T_x and T_z agree with T, indicating that the temperature of each liquid is isotropic. In addition, B_{V1} and B_{V2} denote the positions of each vapor–liquid interface. The distance between B_{L1} and B_{V1} or B_{L2} and B_{V2} represents the thickness of the interface layer illustrated in Fig. 1.1. The delay time, t_I, caused by molecules traveling in the interface layer can be expressed from the characteristic velocity, $\sqrt{2RT_0}$, at the mean temperature of two liquids $T_0 = (T_{L1} + T_{L2})/2 = 0.66T_c$ and the thickness of the interface layer, L_I, as $t_I = L_I/\sqrt{2RT_0}$. Since L_I of each interface layer is approximately $6a$ or $8a$ at $t^* = 0$ found in Fig. 5.7, the delay time normalized by the molecular diameter and the critical temperature, $t_I^* = t_I\sqrt{2RT_0}/a$, becomes approximately 7.4 or 9.8; hence, we find that the normalized delay time is smaller than 10.

We here examine the normalized velocity distribution function at B_{V1}, B_{V2}, B_{L1}, and B_{L2}. The calculation procedure of the normalized velocity distribution function is the same as in Chapter 2 (Section 2.4.2). We set the upper and lower limits of the velocity space to $\zeta_i = -6$ and $\zeta_i = 6$, respectively, and divide this velocity space into 60 cells, where $\zeta_i = \xi_i/\sqrt{2RT_{ref}}$ and T_{ref} is set to $0.60T_c$, As with the estimation of the macroscopic variables, the normalized velocity distribution

function is estimated from the ensemble average of 200 simulations obtained from the different initial conditions.

Figure 5.8 shows the normalized velocity distribution function composed of molecules outgoing from $B_{\mathrm{L}1}$ or $B_{\mathrm{V}1}$ and having velocity $\xi_z > 0$ at $t^* = 0$, 100, 200 and 500. The closed circles denote the normalized velocity distribution function composed of the outgoing molecules from $B_{\mathrm{L}1}$ into the interface layer, and the open circles denote that composed of the outgoing molecules from $B_{\mathrm{V}1}$ into vapor, that is, the normalized velocity distribution function of the KBC because $B_{\mathrm{V}1}$ indicates the position of the vapor–liquid interface of liquid 1. In Fig. 5.8, the dashed lines denote the normalized Maxwellian distribution at $T_{\mathrm{L}1}$ obtained as

$$\sqrt{2RT_{\mathrm{ref}}}\hat{f}^*(\zeta_i) = \sqrt{\frac{T_{\mathrm{ref}}}{\pi T_{\mathrm{L}1}}}\exp\left(-\zeta_i^2\frac{T_{\mathrm{ref}}}{T_{\mathrm{L}1}}\right), \tag{5.15}$$

where i indicates the component in the direction normal or tangential to the vapor–liquid interface ($i = \mathrm{n}$ or t).

As can be seen in Fig. 5.8, the closed circles are in excellent agreement with the dashed lines at each normalized time. This result shows that the outgoing normalized velocity distribution function from $B_{\mathrm{L}1}$ into the interface layer are well described by the normalized Maxwellian distribution at $T_{\mathrm{L}1}$. As can be seen in Fig. 5.8, the closed circles are in excellent agreement with the dashed lines at each normalized time. This result shows that the outgoing normalized velocity distribution function from $B_{\mathrm{L}1}$ into the interface layer are well described by the normalized Maxwellian distribution at $T_{\mathrm{L}1}$. Also, the open circles are in excellent agreement with the dashed lines except for that at $t^* = 0$. In the initial state ($t^* = 0$), the degree of net evaporation/condensation is slightly larger than the applicable range of the normalized Maxwellian distribution given in Chapter 3. Consequently, this deviation is inevitable, but it decreases with time.

Figure 5.9 shows the normalized velocity distribution function composed of molecules outgoing from $B_{\mathrm{L}2}$ or $B_{\mathrm{V}2}$ and having velocity $\xi_z < 0$ at $t^* = 0$, 100, 200 and 500.

The closed circles denote the normalized velocity distribution function composed of the outgoing molecules from $B_{\mathrm{L}2}$ into the interface layer, and the open circles denote that composed of the outgoing molecules from $B_{\mathrm{V}2}$ into vapor, that is, the normalized velocity distribution function of the KBC because $B_{\mathrm{V}2}$ indicates the position of the vapor–liquid interface of liquid 2. In Fig. 5.9, the dashed lines denote the normalized Maxwellian distribution at $T_{\mathrm{L}2}$ obtained as

$$\sqrt{2RT_{\mathrm{ref}}}\hat{f}(\zeta_i) = \sqrt{\frac{T_{\mathrm{ref}}}{\pi T_{\mathrm{L}2}}} \exp\left(-\zeta_i^2 \frac{T_{\mathrm{ref}}}{T_{\mathrm{L}2}}\right). \tag{5.16}$$

As can be seen in Fig. 5.9, similar to Fig. 5.8, the closed circles are in excellent agreement with the dashed lines at each normalized time. This result shows that the outgoing normalized velocity distribution function from $B_{\mathrm{L}2}$ into the interface layer are well described by the normalized Maxwellian distribution at $T_{\mathrm{L}2}$. Also, the open circles are in excellent agreement with the dashed lines except for that at $t^* = 0$. Similar to Fig. 5.8, this deviation is inevitable, but it decreases with time.

On the basis of Figs. 5.8 and 5.9, the outgoing normalized velocity distribution functions from $B_{\mathrm{L}1}$ and $B_{\mathrm{L}2}$ into the interface layer are well described as the normalized Maxwellian distributions at $T_{\mathrm{L}1}$ and $T_{\mathrm{L}2}$, while the outgoing normalized velocity distribution functions from $B_{\mathrm{V}1}$ and $B_{\mathrm{V}2}$ into vapor slightly differ from the normalized Maxwellian distribution at $T_{\mathrm{L}1}$ and $T_{\mathrm{L}2}$ at $t^* = 0$. However, the outgoing normalized velocity distribution functions from $B_{\mathrm{V}1}$ and $B_{\mathrm{V}2}$ into vapor correspond to the normalized Maxwellian distributions at $T_{\mathrm{L}1}$ and $T_{\mathrm{L}2}$ with time. We conclude that the normalized velocity distribution function of the KBC can be assumed to be the normalized Maxwellian distribution in the unsteady two-surface problem even though the interface layer has a finite thickness and the delay time, $t_{\mathrm{I}}^* \lesssim 10$, arises from molecules traveling in this finite interface layer.

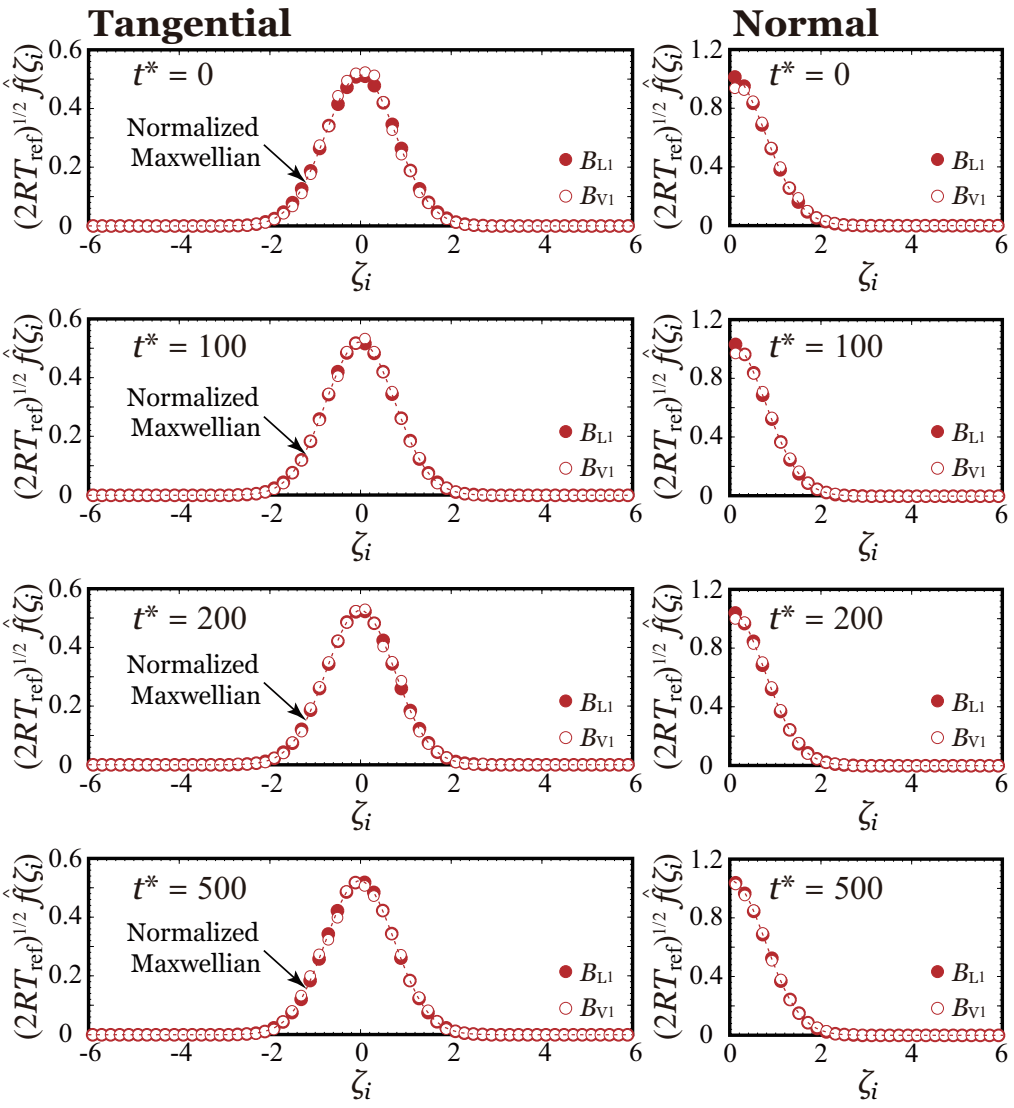

Figure 5.8: Normalized velocity distribution functions composed of the outgoing molecules from the liquid into vapor phase ($\xi_z > 0$) at B_{L1} and B_{V1}.

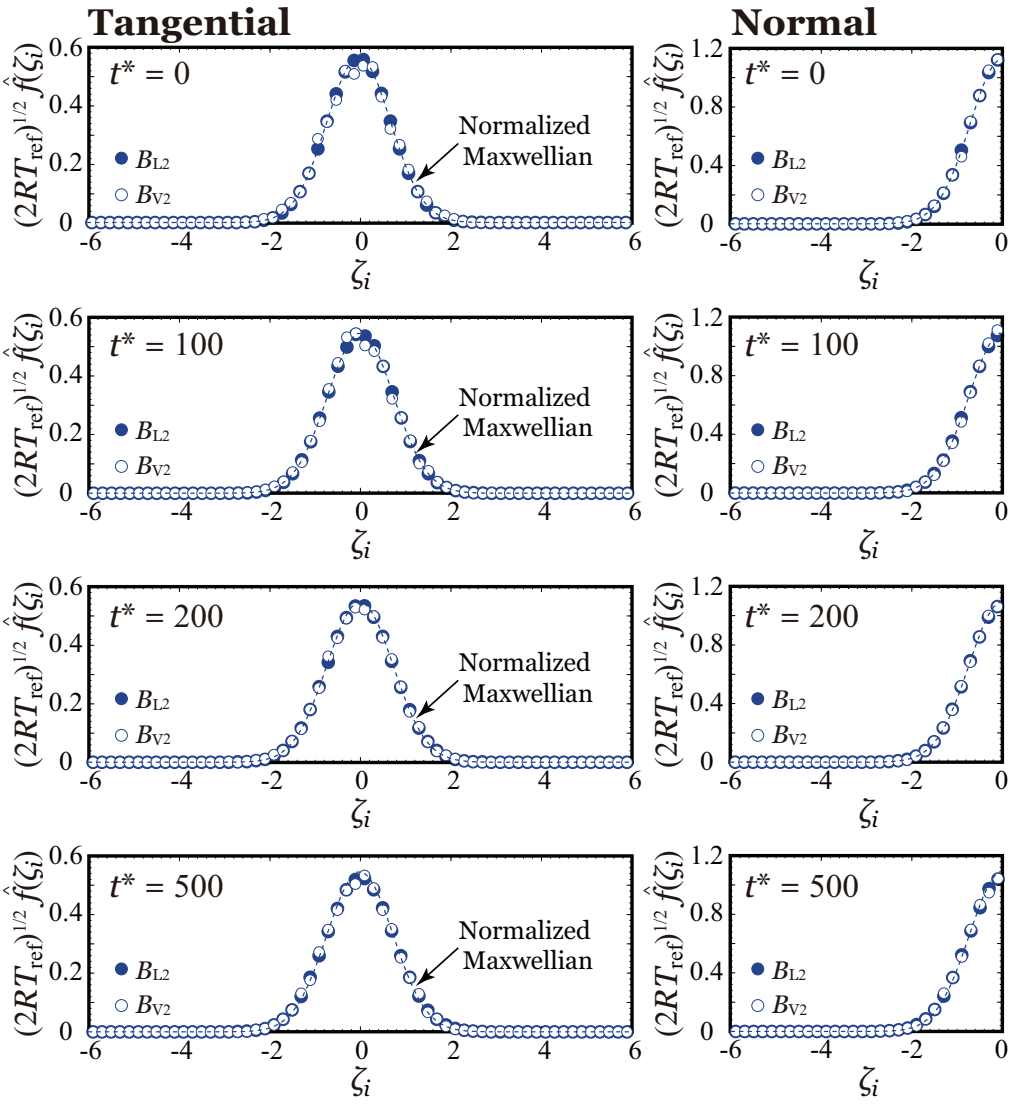

Figure 5.9: Normalized velocity distribution functions composed of the outgoing molecules from the liquid into vapor phase ($\xi_z < 0$) at B_{L2} and B_{V2}.

Estimation of liquid temperature

We here estimate the temporal evolution of the liquid temperature because $\beta(T_{\mathrm{L}})$ in Eq. (3.19) can be specified the liquid temperature. The enlarged view of Fig. 5.7 shows the temperature field in liquid 2 from $t^* = 0$ to 200; we focus only on liquid 2 because its temperature change is larger than that of liquid 1 (see Fig. 5.10: a detailed explanation is given in the next paragraph). In general, the liquid temperature changes spatiotemporally with time on the basis of a one-dimensional heat conduction equation; hence, we should estimate the liquid temperature at the position B_{L1} or B_{L2} to specify the KBC. In contrast, the liquid temperature of liquid 2 changes keeping a spatially almost uniform distribution with time as shown in the enlarged view of Fig. 5.7.

To examine the accuracy of this spatially uniform temperature distribution, we analytically solve the one-dimensional heat conduction equation with the temporal evolution of the temperature of liquid 2 fitted by the exponential function, and then we define the index of uniformity of the spatial temperature distribution. As a result, we confirm that the spatial temperature distribution is to be approximately spatially uniform because the characteristic time of thermal diffusion in liquid 2 ($t_{\mathrm{d}}^* = t_{\mathrm{d}}\sqrt{2RT_{\mathrm{c}}}/a = 2.00$ in this study) is much smaller; therefore, we can estimate each liquid temperature as the spatial average. A detailed explanation of thermal diffusion in liquid 2 is given in Appendix A.

Figure 5.10 shows the temporal evolution of each liquid temperature. Similar to the temporal evolution of net mass flux ρv_z shown in Fig. 5.6, each liquid temperature changes drastically until $t^* = 200$; after that time, each liquid temperature changes gently and eventually converges to approximately 0.69. In Fig. 5.10, we can observe that the temperature of liquid 1 slightly rises from around $t^* = 350$. In this simulation system, the thickness of the liquid slab is relatively thin (approximately $6a$), and the length of the vapor phase is small (approximately ℓ_0). We expect that the cause of this temperature rise is that the energy incident from liquid 2 exceeds

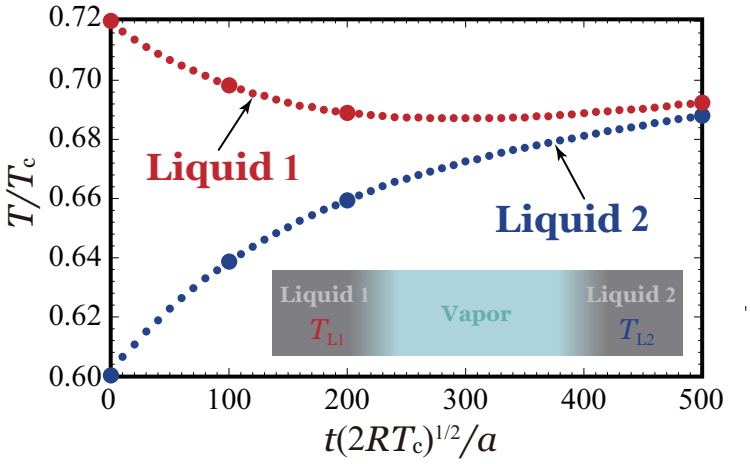

Figure 5.10: Temporal evolution of the temperatures of liquid 1 and liquid 2; the abscissa is normalized by the critical value and the molecular diameter $a/\sqrt{2RT_c}$, and the ordinates is normalized by the critical temperature T_c.

the temperature drop due to the energy release by net evaporation. It is also found that the temperature change of liquid 2 is larger than that of liquid 1. In this simulation, we observe the maximum local Mach number ($|\mathrm{Ma}| \approx 0.2$) at B_{V2} of the initial state ($t^* = 0$). We expect that this maximum Mach number causes the larger temperature change in liquid 2.

Comparison of velocity and temperature fields

Next, we compare the macroscopic variables in vapor, namely, the velocity and the temperature, in the unsteady two-surface problem obtained from the numerical simulation of the ES-BGK equation and those obtained from the EV-DSMC simulation. In the numerical simulation of the ES-BGK equation, we considered a system composed of vapor between two vapor–liquid interfaces. At the vapor–liquid interface, we imposed the KBC (Eq. (3.19)), which is specified by $\alpha_e = \alpha_c = \beta(T_L)$. The reference temperature in the numerical simulation of the ES-BGK equation is set to $T_0 = (T_{L1} + T_{L2})/2 = 0.66T_c$. After the velocity distribution function f in vapor is obtained from the numerical simulation of the ES-BGK equation the velocity and the temperature are estimated by Eqs. (5.8) and (5.9), respectively. The values of

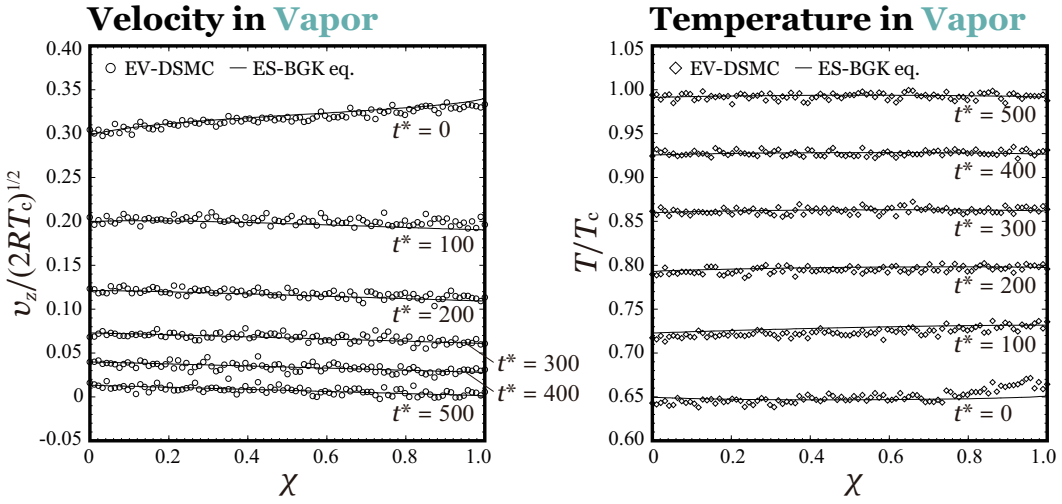

Figure 5.11: Comparison of the velocity v_z and the temperature T in vapor obtained from the EV-DSMC simulation and the numerical simulation of the ES-BGK equation for the unsteady two-surface problem at $t^* = 0$, 100, 200, 300, 400, and 500; χ is the spatial coordinate ($\chi = 0$ indicates the left vapor–liquid interface, and $\chi = 1$ indicates the right vapor–liquid interface in Fig. 5.5), and the ordinates are normalized by the critical values.

$\beta(T_L)$ in Eq. (3.19) vary with the temporal evolution of each liquid temperature as shown in Fig. 5.10; the liquid temperature dependence of $\beta(T_L)$ is explicitly clarified in Chapter 3 (Fig. 3.8).

Figure 5.12 shows the comparison between the velocity and the temperature in vapor obtained from the numerical simulation of the ES-BGK equation and the EV-DSMC simulation. The open diamonds and circles denote the results of the EV-DSMC simulation, and the solid lines denote those of the numerical simulation of the ES-BGK equation. Note that we added the proper offset to the data for legibility. As can be seen in Fig. 5.12, the velocity fields in vapor obtained from these two simulations are in excellent agreement at each time, while the slope of the temperature field at $t^* = 0$ obtained from the EV-DSMC simulation is slightly larger than that obtained from the numerical simulation of the ES-BGK equation. These results imply that the difference of the temperature fields between two different simulations is related to the normalized velocity distribution function of the KBC (see Figs. 5.8 and 5.9). The difference of the temperature field at $t^* = 0$, however, is

sufficiently small and decreases with time as shown in Fig. 5.12. From these results, we conclude that the macroscopic variables obtained from these two simulations are in good agreement even in the unsteady two-surface problem, and the KBC (Eq. (3.19)) is guaranteed to be accurate by considering the time evolution of liquid temperature.

Evaporation/condensation coefficients

Finally, we compare the liquid temperature dependence of α_{e} and α_{c} in the quasi-steady pseudo half-space and unsteady two-surface problems with those obtained in Chapter 3. We calculate these coefficients from the relation $\alpha_{\mathrm{e}} = \alpha_{\mathrm{c}} = \beta(T_{\mathrm{L}})$ based on the result in Chapter 3. We here assume that the mass flux relation is the linear function (Eq. (3.14)) in which $\beta(T_{\mathrm{L}})$ is obtained from the slope. In the quasi-steady pseudo half-space problem, we can obtain two sets of ρv_z and σ at each liquid temperature. Also, in the unsteady two-surface problem, we can obtain one set of ρv_z and σ at the liquid temperature at each time. We can estimate $\beta(T_{\mathrm{L}})$ by linear approximation passing through these points and the vapor–liquid equilibrium point ($\rho v_z = 0$ and $\sigma = \rho^*$). Note that in the unsteady two-surface problem, ρv_z decreases with time and the influence of the statistical error on ρv_z becomes large near vapor–liquid equilibrium. For that reason, we calculate $\beta(T_{\mathrm{L}})$ for the normalized time less than $t^* = 200$ in which the liquid temperature changes drastically.

Figure 5.12 shows the temperature dependence of $\beta(T_{\mathrm{L}})$ in the quasi-steady pseudo half-space and unsteady two-surface problems. In Fig. 5.12, the open circles denote $\alpha_{\mathrm{e}} = \alpha_{\mathrm{c}} = \beta(T_{\mathrm{L}})$ obtained in Chapter 3 (Fig. 3.8). As can be seen in Fig. 5.12, in the quasi-steady pseudo half-space problem, $\beta(T_{\mathrm{L}})$ agrees with that obtained in Chapter 3 at each liquid temperature. In contrast, we can observe that $\beta(T_{\mathrm{L}})$ has high variation in the unsteady two-surface problem. This is because the sample number in the unsteady two-surface problem is only one hundredth of that in the steady two-surface problem considered in Chapter 3. Although it is difficult

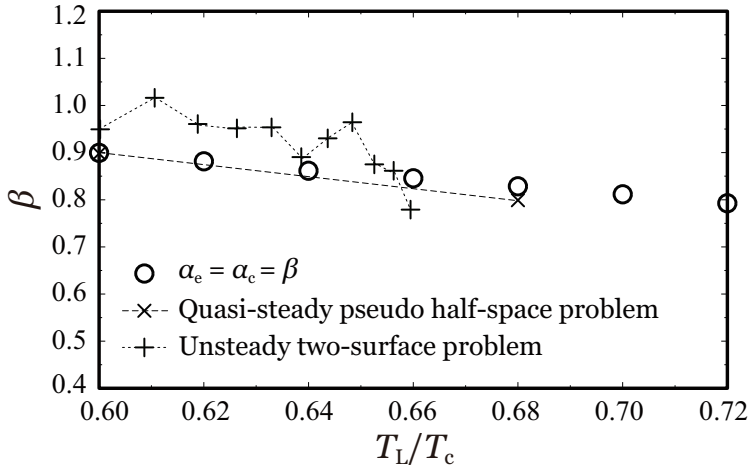

Figure 5.12: Liquid temperature dependence of $\beta(T_L)$ in the quasi-steady pseudo half-space problem and the unsteady two-surface problem; the abscissa is normalized by the critical temperature T_c.

to discuss from this result on the value of $\beta(T_L)$, we can see that the temperature dependencies are roughly in agreement.

5.4 Summary

In this chapter, we verified the accuracy of α_e and α_c obtained in Chapter 3 and Chapter 4. We preliminarily performed the EV-DSMC simulation for the different two vapor–liquid two-phase systems, which are distinct from that considered in the preceding chapters.

First, in these two systems, we confirmed whether the normalized velocity distribution function of the KBC obeys the normalized Maxwellian distribution (Eq. (2.2)). In the quasi-steady pseudo half-space problem, the normalized velocity distribution function of the KBC more or less agrees with the normalized Maxwellian distribution (Eq. (1.32)) in all four cases of net evaporation and condensation (Fig. 5.3). In the unsteady two-surface problem, the normalized velocity distribution function of the KBC agrees with the normalized Maxwellian distribution except for that at $t^* = 0$. However, this deviation at $t^* = 0$ decreases with time (Figs. 5.8 and 5.9). From these result, we concluded that the normalized velocity distribution functions

of the KBC can be assumed the normalized Maxwellian distribution in both the quasi-steady pseudo half-space and unsteady two-surface problems.

Next, we compared the macroscopic variables in vapor, namely, the velocity and the temperature, in these two systems obtained from the numerical simulation of the ES-BGK equation with the KBC (Eq. (3.19)), which is specified by $\alpha_{\mathrm{e}} = \alpha_{\mathrm{c}} = \beta(T_{\mathrm{L}})$, and those obtained from the EV-DSMC simulation. In the quasi-steady pseudo half-space problem, the velocity and temperature fields in vapor obtained from two different simulations are in almost agreement except for a region near the vapor–liquid interface in some cases (Fig. 5.4). A cause of this deviation of the macroscopic variables is not due to the inappropriate KBC but due to the difference of the simulation system between the EV-DSMC simulation and the numerical simulation of the ES-BGK equation. The quasi-steady simulation is carried out in the EV-DSMC simulation, whereas in the numerical simulation of the ES-BGK equation, the complete steady simulation is carried out. However, the deviation of the macroscopic variables obtained from these two simulations is sufficiently small except for a region near the vapor–liquid interface. In the unsteady two-surface problem, the velocity fields in vapor obtained from these two simulations are in excellent agreement at each time, while the slope of the temperature field at $t^* = 0$ obtained from the EV-DSMC simulation is slightly larger than that obtained from the numerical simulation of the ES-BGK equation (Fig. 5.12). The difference of the temperature field at $t^* = 0$, however, is sufficiently small and decreases with time as shown in Fig. 5.12. From these results, we concluded that the macroscopic variables obtained from the EV-DSMC simulation and the numerical simulation of the ES-BGK equation are in good agreement in both the quasi-steady pseudo half-space and unsteady two-surface problems; thus, the KBC (Eq. (3.19)) is guaranteed to be accurate.

Finally, we compared the liquid temperature dependence of α_{e} and α_{c} in these two systems with those obtained in Chapter 3. We calculated these coefficients as $\alpha_{\mathrm{e}} = \alpha_{\mathrm{c}} = \beta(T_{\mathrm{L}})$ based on the result in Chapter 3. In the quasi-steady pseudo

half-space problem, $\beta(T_\mathrm{L})$ agrees with that obtained in Chapter 3 at each liquid temperature. In contrast, $\beta(T_\mathrm{L})$ has high variation in the unsteady two-surface problem. This is because the sample number in the unsteady two-surface problem is only one hundredth of that in the steady two-surface problem considered in Chapter 3. Although it is difficult to discuss from this result on the value of $\beta(T_\mathrm{L})$, the liquid temperature dependencies are roughly in agreement.

Let us summarize the significance of the results so far. In this chapter, we suggested that the KBC (Eq. (3.19)), which is specified by $\alpha_\mathrm{e} = \alpha_\mathrm{c} = \beta(T_\mathrm{L})$, can be applied to not only a specific system but also other systems, namely, the quasi-steady pseudo half-space and unsteady two-surface problems. Needless to say, these results do not indicate that the KBC (Eq. (3.19)) can be applied to all net evaporation/condensation problems. For example, we set the length of the vapor phase to approximately the mean free path in all simulation systems. If we set this length as a variable, further investigation should be required. Furthermore, in the molecular gas dynamics analysis, the solution of the Boltzmann equation have been examined on exhaustively various net evaporation/condensation problems. It is almost impossible to verify the KBC in all the net evaporation/condensation problems by using the molecular simulation. Therefore, we examined only some of the typical problems and conditions here. However, we emphasize that if we consider the formulated mass flux relation (Eq. (3.14)) is a fundamental physical law, the KBC proposed in this thesis can be established regardless the systems.

Chapter

6

Conclusion

The target of this thesis is heat and mass transfer in a two-phase system composed of single-component monatomic vapor and its condensed phase (liquid). We especially examined heat and mass transfer associated with a mass flux in the direction normal to the vapor–liquid interface (net evaporation/condensation). The objective of this thesis is to propose a physically proper boundary condition at the vapor–liquid interface. What we have to do to propose the boundary condition are (i) to conduct the molecular simulation to construct the boundary condition for the Boltzmann equation (KBC) and (ii) to conduct the Knudsen layer analysis to derive the boundary condition for the fluid dynamic equations. As for (ii), it has been systematically investigated by Sone *et al.* [12, 23]; hence, as long as these results are available, the only thing we should study in this thesis is (i).

To construct the KBC, we have to specify the unknown parameters included in the KBC, namely, the evaporation coefficient α_{e} and condensation coefficient α_{c}. In this thesis, to specify these coefficients, we investigated a fundamental rule at the vapor–liquid interface by the molecular simulation based on the mean-field kinetic theory (the EV-DSMC simulation). This fundamental rule holds regardless of any condition, that is, the conservation law of the mass flux extended to the microscopic point of view (the mass flux relation). A feature of this thesis is to utilize the EV-DSMC simulation for the molecular simulation. The EV-DSMC simulation for

the spatially one-dimensional flow runs about 50–60 times faster than an equivalent molecular dynamics simulation, which is well-used simulation method for the vapor–liquid two-phase system, with the same number of molecules. In the following, we summarize the results of the main chapters and propose the boundary condition at the vapor–liquid interface based on these results.

Chapter 3

In Chapter 3, we examined the mass flux relation (Eq. (2.3)) to find a pair of α_{e} and α_{c} defined by Eq. (1.42) by the EV-DSMC simulation explained in Chapter 2. We preliminarily performed the EV-DSMC simulation for the two-surface problem in 160 cases of the temperature differences between two liquids.

First, we confirmed whether the normalized velocity distribution function of the KBC obeys the normalized Maxwellian distribution, which is the basis of the definitions of α_{e} and α_{c} (Eq. (1.42)). From the result, we found that the temperatures in the KBC gradually change with the strong net evaporation/condensation, and the normalized velocity distribution function of the KBC becomes an anisotropic Maxwellian distribution (Fig. 3.5). We then investigated how such an anisotropic Maxwellian distribution affects the macroscopic variables and the fluxes in vapor by comparing the results obtained from the EV-DSMC simulation and the numerical simulation of a model of the Boltzmann equation (the ES-BGK equation). From this comparison, we determined the range to which the normalized Maxwellian distribution can be applied as the normalized velocity distribution function of the KBC. From the result, we found that the applicable range of the normalized Maxwellian distribution is $0.5 \lesssim \sigma/\rho^* \lesssim 2.3$ for all reference liquid temperatures.

Next, we formulated the mass flux relation at each reference liquid temperature by using ρv_z obtained by the EV-DSMC simulation and corresponding σ (Eq. (2.4)). From the result, we found that ρv_z is the linear function of σ (Fig. 3.7). We formulated the mass flux relation by applying the linear regression analysis to the relation

between ρv_z and σ at each reference liquid temperature. The slope of the linear function β_{ne} for net evaporation and that of β_{nc} for net condensation are slightly different. For example, $\beta_{\mathrm{ne}} = 0.871$ and $\beta_{\mathrm{nc}} = 0.927$ in the case of $T_{\mathrm{L}}/T_{\mathrm{c}} = 0.60$. Also, the difference between β_{ne} and β_{nc} becomes smaller with the higher reference liquid temperature. Unfortunately, the cause of the difference between β_{ne} and β_{nc} is unclear. At least, the generalized KBC (Eq. (2.1)), which is considered in this thesis, does not permit such formulation according to σ. Hence, we modified the slope of the mass flux relation as $\beta = (\beta_{\mathrm{ne}} + \beta_{\mathrm{nc}})/2$. We then discussed α_{e} and α_{c} defined by Eq. (1.42) by comparing the formulated mass flux relation (Eq. (3.14)) with Eq. (2.3). From the result, we found the relation $\alpha_{\mathrm{e}} = \alpha_{\mathrm{c}} = \beta(T_{\mathrm{L}})$ without explicitly defining the molecular processes illustrated in Fig. 1.1.

On the basis of the results in Chapter 3, we proposed the following KBC at the vapor–liquid interface by using obtained α_{e} and α_{c}.

$$f_{\mathrm{out}} = [\beta(T_{\mathrm{L}})\rho^* + (1 - \beta(T_{\mathrm{L}}))\sigma]\hat{f}^*. \tag{3.19}$$

This KBC is essentially equivalent to what we set $\mathcal{A} = \alpha_{\mathrm{e}}\rho^* + (1 - \alpha_{\mathrm{c}})\sigma$ in the generalized KBC (Eq. (2.1)) because of the relation $\alpha_{\mathrm{e}} = \alpha_{\mathrm{c}} = \beta(T_{\mathrm{L}})$. An important result is that we can find the relation $\alpha_{\mathrm{e}} = \alpha_{\mathrm{c}} = \beta(T_{\mathrm{L}})$ by formulating the mass flux relation at the vapor–liquid interface with high accuracy. However, the results in this chapter have only found a pair of α_{e} and α_{c} defined by Eq. (1.42) at each liquid temperature, and the relation between these coefficients and the molecular processes illustrated in Fig. 1.1 is not clear.

Chapter 4

In Chapter 4, we considered the physical meaning of α_{e} and α_{c} obtained in Chapter 3. To determine α_{e} and α_{c} uniquely, we have to clarify the definitions of the molecular processes illustrated in Fig. 1.1. Although this definition has not been clarified, if

we assume a certain condition, these molecular processes can be distinguished. We here consider a hypothesis of the spontaneous evaporation [33, 44]. According to this hypothesis, α_{e} and α_{c} are defined by the mass fluxes related to the molecular processes, such as J^*_{evap} and J_{cond}. We calculated J^*_{evap} and J_{cond} by the improved two-boundary method proposed by Kobayashi et al. [30, 91] to examine α_{e} and α_{c} according to the hypothesis of the spontaneous evaporation. As a preparation, we modified the formulated mass flux relation (Eq. (3.14)) to obtain the expressions of J^*_{evap} and J_{cond} by using $\beta(T_{\mathrm{L}})$ (Eq. (4.14)).

First, we confirmed whether the normalized velocity distribution function of the evaporation molecules obeys the normalized Maxwellian distribution (Eq. (2.2)), which is the premise of the hypothesis of the spontaneous evaporation. From the result, we found that the normalized velocity distribution function of the evaporation molecules in vapor–liquid equilibrium seems to agree with the normalized Maxwellian distribution, and those in net evaporation and condensation also seem to agree with the normalized Maxwellian (Fig. 4.5). These results showed that the premise of the hypothesis of the spontaneous evaporation holds even in the case of the highest liquid temperature accompanied with net evaporation/condensation.

Next, we discussed the correspondence of the hypothesis of the spontaneous evaporation with α_{e} and α_{c} obtained in Chapter 3 by comparing J^*_{evap} and J_{cond} obtained from Eq. (4.14) and those calculated by the improved two-boundary method. From the result, we found that J^*_{evap} and J_{cond} obtained from two different methods show an excellent agreement in both vapor–liquid equilibrium and net evaporation/condensation (Figs. 4.6 and 4.7). We concluded that $\beta(T_{\mathrm{L}})$ follows the definitions of α_{e} and α_{c} according to the hypothesis of the spontaneous evaporation: $\alpha_{\mathrm{e}} = \alpha_{\mathrm{c}} = J^*_{\mathrm{evap}}/J^*_{\mathrm{out}}$ in vapor–liquid equilibrium, while $\alpha_{\mathrm{e}} = J^*_{\mathrm{evap}}/J^*_{\mathrm{out}}$ and $\alpha_{\mathrm{c}} = J_{\mathrm{cond}}/J_{\mathrm{coll}}$ in net evaporation/condensation.

On the basis of the results of Chapter 4, the following definition of $\mathcal{A}_0(T_{\mathrm{L}})$ in

Eq. (1.42) can be obtained.

$$\mathcal{A}_0(T_\mathrm{L}) = \mathcal{B}(T_\mathrm{L}) \equiv \frac{J^*_\mathrm{evap}}{\sqrt{RT_\mathrm{L}/(2\pi)}}. \tag{4.15}$$

Although this result includes some assumptions, we succeeded to clarify the relation between $\beta(T_\mathrm{L})$ and the molecular processes illustrated in Fig. 1.1 by specifying $\mathcal{A}_0(T_\mathrm{L})$.

Chapter 5

In Chapter 5, we verified the accuracy of α_e and α_c obtained in Chapter 3 and Chapter 4. We preliminarily performed the EV-DSMC simulation for the different two vapor–liquid two-phase systems, which are distinct from that considered in the preceding chapters (quasi-steady pseudo half-space problem and unsteady two-surface problem).

First, in these two systems, we confirmed whether the normalized velocity distribution function of the KBC obeys the normalized Maxwellian distribution (Eq. (2.2)). In the quasi-steady pseudo half-space problem, the normalized velocity distribution function of the KBC more or less agrees with the normalized Maxwellian distribution (Eq. (1.32)) in all four cases of net evaporation and condensation (Fig. 5.3). In the unsteady two-surface problem, the normalized velocity distribution function of the KBC agrees with the normalized Maxwellian distribution except for that at $t^* = 0$. However, this deviation at $t^* = 0$ decreases with time (Figs. 5.8 and 5.9). From these result, we concluded that the normalized velocity distribution functions of the KBC can be assumed the normalized Maxwellian distribution in both the quasi-steady pseudo half-space and unsteady two-surface problems.

Next, we compared the macroscopic variables in vapor, namely, the velocity and the temperature, in these two systems obtained from the numerical simulation of the ES-BGK equation with the KBC (Eq. (3.19)), which is specified by $\alpha_\mathrm{e} = \alpha_\mathrm{c} = \beta(T_\mathrm{L})$,

and those obtained from the EV-DSMC simulation. In the quasi-steady pseudo half-space problem, the velocity and temperature fields in vapor obtained from two different simulations are in almost agreement except for a region near the vapor–liquid interface in some cases (Fig. 5.4). A cause of this deviation of the macroscopic variables is not due to the inappropriate KBC but due to the difference of the simulation system between the EV-DSMC simulation and the numerical simulation of the ES-BGK equation. The quasi-steady simulation is carried out in the EV-DSMC simulation, whereas in the numerical simulation of the ES-BGK equation, the complete steady simulation is carried out. However, the deviation of the macroscopic variables obtained from these two simulations is sufficiently small except for a region near the vapor–liquid interface. In the unsteady two-surface problem, the velocity fields in vapor obtained from these two simulations are in excellent agreement at each time, while the slope of the temperature field at $t^* = 0$ obtained from the EV-DSMC simulation is slightly larger than that obtained from the numerical simulation of the ES-BGK equation (Fig. 5.12). The difference of the temperature field at $t^* = 0$, however, is sufficiently small and decreases with time as shown in Fig. 5.12. From these results, we concluded that the macroscopic variables obtained from the EV-DSMC simulation and the numerical simulation of the ES-BGK equation are in good agreement in both the quasi-steady pseudo half-space and unsteady two-surface problems; thus, the KBC (Eq. (3.19)) is guaranteed to be accurate.

Finally, we compared the liquid temperature dependence of α_e and α_c in these two systems with those obtained in Chapter 3. We calculated these coefficients as $\alpha_\mathrm{e} = \alpha_\mathrm{c} = \beta(T_\mathrm{L})$ based on the result in Chapter 3. In the quasi-steady pseudo half-space problem, $\beta(T_\mathrm{L})$ agrees with that obtained in Chapter 3 at each liquid temperature. In contrast, $\beta(T_\mathrm{L})$ has high variation in the unsteady two-surface problem. This is because the sample number in the unsteady two-surface problem is only one hundredth of that in the steady two-surface problem considered in Chapter 3. Although it is difficult to discuss from this result on the value of $\beta(T_\mathrm{L})$, the

liquid temperature dependencies are roughly in agreement.

On the basis of the results in Chapter 5, we suggested that the KBC (Eq. (3.19)), which is specified by $\alpha_{\mathrm{e}} = \alpha_{\mathrm{c}} = \beta(T_{\mathrm{L}})$, can be applied to not only a specific system but also other systems, namely, the quasi-steady pseudo half-space and unsteady two-surface problems. Needless to say, these results do not indicate that the KBC (Eq. (3.19)) can be applied to all net evaporation/condensation problems. For example, we set the length of the vapor phase to approximately the mean free path in all simulation systems. If we set this length as a variable, further investigation should be required. Furthermore, in the molecular gas dynamics analysis, the solution of the Boltzmann equation have been examined on exhaustively various net evaporation/condensation problems. It is almost impossible to verify the KBC in all the net evaporation/condensation problems by using the molecular simulation. Therefore, we examined only some of the typical problems and conditions in this thesis. However, we emphasize that if we consider the formulated mass flux relation (Eq. (3.14)) is a fundamental physical law, the KBC proposed in this thesis can be established regardless the systems.

Boundary condition at vapor–liquid interface

We succeeded to propose the KBC at the vapor–liquid interface based on the results in Chapter 3–5. The pressure p and the temperature T at the end of the Knudsen layer can eventually be obtained by the Knudsen layer analysis with the KBC proposed in this thesis,

$$\frac{p - p^*}{p^*} = \left(C_4^* - 2\sqrt{\pi} \frac{1 - \beta(T_{\mathrm{L}})}{\beta(T_{\mathrm{L}})} \right) \frac{(v_i - v_{\mathrm{w}i}) n_i}{\sqrt{2RT_{\mathrm{L}}}},$$
$$\frac{T - T_{\mathrm{L}}}{T_{\mathrm{L}}} = d_4^* \frac{(v_i - v_{\mathrm{w}i}) n_i}{\sqrt{2RT_{\mathrm{L}}}}.$$

Furthermore, the mass flux at the end of the Knudsen layer can also be obtained as

$$\mathcal{M}_{\mathrm{MGD}} = \frac{1}{2\sqrt{\pi}\frac{1-\beta(T_{\mathrm{L}})}{\beta(T_{\mathrm{L}})} - C_4^*} \sqrt{\frac{2}{R}} \left(\frac{p^*}{\sqrt{T_{\mathrm{L}}}} - \frac{p}{\sqrt{T_{\mathrm{L}}}} \right).$$

Although these expressions seem to be the same as Eqs. (1.37), (1.38), and (1.39), it is advantageous in that these expressions is derived by using the KBC that is constructed based on the precise investigation by the molecular simulation. With the use of this mass flux, or the pressure, and the temperature as the boundary conditions, the fluid dynamic equations can be closed and then the solution that takes into account the molecular interactions in the interface layer and the Knudsen layer can be obtained.

Chapter

A

Appendix

Thermal diffusion in medium bounded by two parallel planes

Note that some characters other than the liquid temperature T_{L} and the thermal conductivity λ_{E} are defined differently from the main chapters. Our proposed KBC: Eq.(3.19), requires the liquid temperature, T_{L}. It is widely accepted that the temperature field in liquid phase can be assumed to be uniform in the case of steady net evaporation or condensation [34, 39, 48–51]; hence, T_{L} can be defined without ambiguity. However, the uniformity of the temperature field is no longer necessarily guaranteed in the case of unsteady net evaporation or condensation; hence, we need to evaluate T_{L} with extra caution. In Chapter 5, we calculated the spatial averaged temperature over liquid; then, we define this averaged temperature: T_{A}, as the liquid temperature T_{L}. This definition can be accepted only if the temperature field is uniform enough. In this appendix, we discuss the legitimacy of this definition.

Under the assumption of no advection, the unsteady temperature field of bulk liquid is governed by the one-dimensional heat conduction equation:

$$\frac{\partial T}{\partial t} = \theta \frac{\partial^2 T}{\partial z^2}, \tag{A.1}$$

where θ is thermal diffusivity, which can be obtained with the use of the Chapman–Enskog approximation of the Enskog-Vlasov equation [72],

$$\theta = \frac{\lambda}{C\rho}, \tag{A.2}$$

where C is the specific heat and λ_{E} is thermal conductivity obtained from Eq. (2.24) (temperature characteristics of λ_{E} is given in Fig. 2.7). The liquid thermal diffusivity $\theta = 5.77a(2RT_{\mathrm{c}})^{\frac{1}{2}}$ is obtained at $T_{\mathrm{L}}/T_{\mathrm{c}} = 0.60$ from Eq. (A.2) The temporal bulk liquid temperature field obtained from Eq. (A.1) with appropriate boundary and initial conditions, in general, is spatially nonuniform; however, the temperature of liquid 2 obtained from the EV-DSMC simulation changes keeping spatially almost uniform distribution as shown in the enlarged view of Fig. 5.7. Note that we also observed that the temperature of liquid 1 changes keeping spatially almost uniform distribution. These results suggest that the use of T_{A} for T_{L} may be accepted in the range of the present calculation. We discuss the legitimacy the use of T_{A} for T_{L} further by considering the solution of Eq. (A.1).

We investigate the temporal change of the spatial temperature distribution in liquid. We consider the following problem following the textbook of Carslaw and Jaeger [93]. Liquid is bounded by two parallel planes: the region $-L < z < L$ with zero initial temperature. The surfaces temperature T_{S} changes with time. It should be noted here that the uniformity of the spatial temperature distribution is greatly dependent on the rate of change of T_{S}. In order to solve Eq. (A.1), we properly prepare the boundary condition T_{S}. We assume that T_{S} can be roughly approximated by T_{A}. The temporal change of T_{A} is shown in Fig. A.1. We found that the data can be well fitted by the exponential function:

$$T_{\mathrm{S}}(t:\omega) = T_0[1 - \exp(-\omega t)], \tag{A.3}$$

where t is time, T_0 is the temperature difference, and ω is the fitting parameter rang-

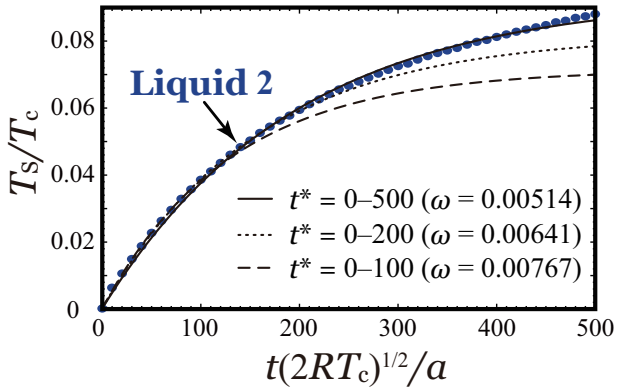

Figure A.1: Fitting results of the temporal evolution of the temperature of liquid 2.

ing $0.005 \leq \omega \leq 0.008$. The temperature distribution with the boundary condition (Eq. (A.3)) can be found in p.104 of the literature [93]:

$$\begin{aligned} T(t;\omega) =& T_0 - T_0 \exp(-\omega t)\frac{\cos(x\sqrt{\omega/\theta})}{\cos(L\sqrt{\omega/\theta})} \\ & - \frac{16T_0\omega L^2}{\pi}\sum_{n=0}^{\infty}\frac{(-1)^l \exp\left[-(2l+1)^2\pi^2\theta t/(4L^2)\right]}{(2l+1)\left[4\omega L^2-(2l+1)^2\pi^2\theta\right]}\cos\left[\frac{(2l+1)\pi x}{2L}\right]. \end{aligned} \tag{A.4}$$

We introduce the characteristic time t_d:

$$t_\mathrm{d} = \frac{L^2}{\theta}, \tag{A.5}$$

and the following nondimensional variables:

$$T^* = \frac{T}{T_0}, \quad T_\mathrm{S}^* = \frac{T_\mathrm{S}}{T_0}, \quad \tau = \frac{t}{t_\mathrm{d}}, \quad \zeta = \frac{z}{L}, \quad b = \omega t_\mathrm{d}, \tag{A.6}$$

then, Eqs. (A.3) and (A.4) can be rewritten:

$$T_{\rm S}^*(\tau;b) = 1-\exp(-b\tau), \tag{A.7}$$

$$T^*(\tau;b) = 1-\exp(-b\tau)\frac{\cos(\zeta\sqrt{b})}{\cos(\sqrt{b})} \tag{A.8}$$

$$+\frac{16b}{\pi}\sum_{n=0}^{\infty}\frac{(-1)^n\exp\left[-(2l+1)^2\pi^2\tau/4\right]}{(2l+1)\left[(2l+1)^2\pi^2-4b\right]}\cos\left[\frac{(2l+1)\pi\zeta}{2}\right]. \tag{A.9}$$

Integration of Eq. (A.10) on $0\leq\zeta\leq 1$ gives the averaged temperature $T_{\rm A}^*$:

$$T_{\rm A}^*(\tau;b) = 1-\exp(-b\tau)\frac{\sin(\sqrt{b})}{\sqrt{b}\cos(\sqrt{b})}+32b\sum_{n=0}^{\infty}\frac{\exp\left[-(2l+1)^2\pi^2\tau/4\right]}{(2l+1)^2\pi^2\left[(2l+1)^2\pi^2-4b\right]}. \tag{A.10}$$

It should be noted here that $t_{\rm d}=2.00$ in the present calculation; then, $0.01\leq b\leq 0.016$.

Now, we define the index of uniformity $\kappa(\tau,b)$:

$$\kappa(\tau,b) = 1-\frac{T_{\rm A}^*(\tau;b)}{T_{\rm S}^*(\tau;b)}. \tag{A.11}$$

$\kappa(\tau,b)$ provides the base to discuss the legitimacy of the use of $T_{\rm A}$ for $T_{\rm L}$. We can secure the legitimacy if $\kappa(\tau,b)$ is sufficiently small. Figure A.2 shows the temporal change of $\kappa(\tau,b)$ for various b. $\kappa(\tau,b)$ monotonously converges to zero with the increase in τ, regardless of the magnitude of b; hence for any given ν such that $0\leq\nu\leq 1$, there exists $\tau_\nu(b)$ that satisfies $\kappa(\tau_\nu,b)=\nu$. The smaller b is, the larger $\tau_\nu(b)$ is, i.e., the slower $\kappa(\tau,b)$ converges to zero.

The temporal change of $\kappa^0(\tau)=\kappa(\tau,b\to 0)$ that is written as

$$\kappa^0(\tau) = \lim_{b\to 0}\kappa(\tau,b) = 1-\frac{1}{\tau}\left[\frac{1}{3}-32\sum_{n=0}^{\infty}\frac{\exp\left[-(2l+1)^2\pi^2\tau/4\right]}{(2l+1)^4\pi^4}\right], \tag{A.12}$$

is also shown in Fig. A.2. τ_ν^0 that satisfies $\kappa^0(\tau_\nu^0)=\nu$ provides the upper limit

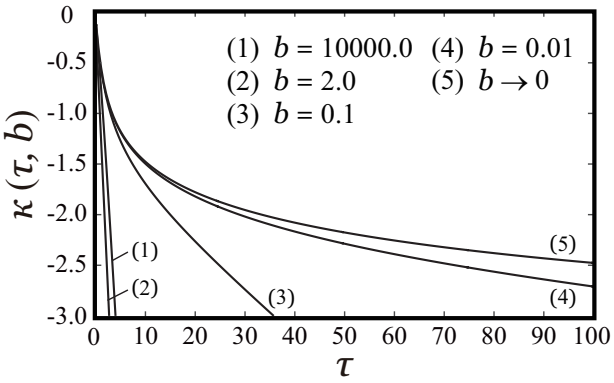

Figure A.2: Temporal change of the averaged temperature and required time.

of $\tau_\nu(b)$. It should be noted here that b obtained from the present calculation is small enough that $\tau_\nu(b)$ can be well approximated by τ_ν^0 as observed in Fig. A.2. The typical values of τ_ν^0 for $\nu = 0.05$ and 0.02 are $\tau_{0.05}^0 = 6.67$ and $\tau_{0.02}^0 = 16.67$, respectively. Therefore, as far as $t > 33.4$ ($t_\mathrm{d} = 2.00$), We can regard that the unsteady temperature field in the liquid 2 is approximately spatially uniform (see the enlarged view of Fig. 5.7) since $\kappa(\tau, b) < 0.02$ from the analytical solution of one-dimensional heat conduction equation. The above investigation ensures that the heat transfer defined in the present study can be described by one-dimensional heat conduction equation when there is no advection in liquid; that is, we can carry out the numerical simulation of vapor–liquid two-phase flow with unsteady net evaporation/condensation in large spatial scale by coupling the one-dimensional heat conduction equation (Eq. (A.1)) and the Boltzmann equation, without carrying out the molecular simulation of bulk liquid that contains enormously larger number of molecules than those in bulk vapor.

References

[1] S. Fujikawa, T. Akamatsu, Effects of the non-equilibrium condensation of vapour on the pressure wave produced by the collapse of a bubble in a liquid, Journal of Fluid Mechanics 97 (03) (1980) 481–512.

[2] I. Akhatov, O. Lindau, A. Topolnikov, R. Mettin, N. Vakhitova, W. Lauterborn, Collapse and rebound of a laser-induced cavitation bubble, Physics of Fluids 13 (10) (2001) 2805–2819.

[3] Y. Jinbo, T. Ogasawara, H. Takahira, Influence of the nonequilibrium phase transition on the collapse of inertia nonspherical bubbles in a compressible liquid, Experimental Thermal and Fluid Science 60 (2015) 374–384.

[4] J. G. Leidenfrost, On the fixation of water in diverse fire, International Journal of Heat and Mass Transfer 9 (11) (1966) 1153–1166.

[5] H. Linke, B. Alemán, L. Melling, M. Taormina, M. Francis, C. Dow-Hygelund, V. Narayanan, R. Taylor, A. Stout, Self-propelled leidenfrost droplets, Physical Review Letters 96 (15) (2006) 154502.

[6] D. Quéré, Leidenfrost dynamics, Annual Review of Fluid Mechanics 45 (2013) 197–215.

[7] S. Fujikawa, T. Yano, M. Watanabe, Vapor-liquid interfaces, bubbles and droplets: Fundamentals and applications, Springer Science & Business Media, 2011.

[8] K. Kobayashi, T. Kodama, H. Takahira, Shock wave–bubble interaction near soft and rigid boundaries during lithotripsy: numerical analysis by the improved ghost fluid method, Physics in Medicine and Biology 56 (19) (2011) 6421.

[9] C.-D. Ohl, M. Arora, R. Ikink, N. De Jong, M. Versluis, M. Delius, D. Lohse, Sonoporation from jetting cavitation bubbles, Biophysical Journal 91 (11) (2006) 4285–4295.

[10] H. K. Cammenga, Evaporation mechanisms of liquids, Current Topics in Materials Science 5 (1980) 335–446.

[11] A. H. Persad, C. A. Ward, Expressions for the evaporation and condensation coefficients in the hertz-knudsen relation, Chemical Reviews 116 (14) (2016) 7727–7767.

[12] Y. Sone, Molecular gas dynamics: theory, techniques, and applications, Springer Science & Business Media, 2007.

[13] M. Matsumoto, Y. Kataoka, Dynamic processes at a liquid surface of methanol, Physical Review Letters 69 (26) (1992) 3782.

[14] M. Matsumoto, Molecular dynamics simulation of interphase transport at liquid surfaces, Fluid Phase Equilibria 125 (1) (1996) 195–203.

[15] M. Matsumoto, Molecular dynamics of fluid phase change, Fluid Phase Equilibria 144 (1) (1998) 307–314.

[16] T. Yang, C. Pan, Molecular dynamics simulation of a thin water layer evaporation and evaporation coefficient, International Journal of Heat and Mass Transfer 48 (17) (2005) 3516–3526.

[17] J. Xu, S. Kjelstrup, D. Bedeaux, A. Røsjorde, L. Rekvig, Verification of onsager's reciprocal relations for evaporation and condensation using non-equilibrium molecular dynamics, Journal of colloid and interface science 299 (1) (2006) 452–463.

[18] B.-Y. Cao, J.-F. Xie, S. S. Sazhin, Molecular dynamics study on evaporation and condensation of n-dodecane at liquid–vapor phase equilibria, The Journal of Chemical Physics 134 (16) (2011) 164309.

[19] J.-F. Xie, S. S. Sazhin, B.-Y. Cao, Molecular dynamics study of the processes in the vicinity of the n-dodecane vapour/liquid interface, Physics of Fluids 23 (11) (2011) 112104.

[20] S. Cheng, J. B. Lechman, S. J. Plimpton, G. S. Grest, Evaporation of Lennard-Jones fluids, The Journal of Chemical Physics 134 (22) (2011) 224704.

[21] H. Grad, Principles of the kinetic theory of gases, in: Thermodynamik der Gase/Thermodynamics of Gases, Springer, 1958, pp. 205–294.

[22] H. Grad, On the kinetic theory of rarefied gases, Communications on pure and applied mathematics 2 (4) (1949) 331–407.

[23] Y. Sone, Y. Onishi, Kinetic theory of evaporation and condensation–Hydrodynamic equation and slip boundary condition–, Journal of the Physical Society of Japan 44 (6) (1978) 1981–1994.

[24] Y.-P. Pao, Application of kinetic theory to the problem of evaporation and condensation, Physics of Fluids 14 (2) (1971) 306–312.

[25] T. Soga, A kinetic theory analysis of unsteady evaporation from a liquid surface with temperature change, Journal of the Physical Society of Japan 55 (5) (1986) 1556–1567.

[26] V. Zhakhovskii, S. Anisimov, Molecular-dynamics simulation of evaporation of a liquid, Journal of Experimental and Theoretical Physics 84 (4) (1997) 734–745.

[27] R. Meland, A. Frezzotti, T. Ytrehus, B. Hafskjold, Nonequilibrium molecular-dynamics simulation of net evaporation and net condensation, and evaluation

of the gas-kinetic boundary condition at the interphase, Physics of Fluids 16 (2) (2004) 223–243.

[28] K. Gu, C. B. Watkins, J. Koplik, Molecular dynamics simulation of the equilibrium liquid–vapor interphase with solidification, Fluid Phase Equilibria 297 (1) (2010) 77–89.

[29] K. Gu, C. B. Watkins, J. Koplik, Multiscale molecular simulations of argon vapor condensation onto a cooled substrate with bulk flow, Physics of Fluids 22 (11) (2010) 112002.

[30] K. Kobayashi, K. Hori, M. Kon, K. Sasaki, M. Watanabe, Molecular dynamics study on evaporation and reflection of monatomic molecules to construct kinetic boundary condition in vapor–liquid equilibria, Heat and Mass Transfer (2015) 1–9.

[31] T. Tsuruta, H. Tanaka, T. Masuoka, Condensation/evaporation coefficient and velocity distributions at liquid–vapor interface, International Journal of Heat and Mass Transfer 42 (22) (1999) 4107–4116.

[32] G. Nagayama, T. Tsuruta, A general expression for the condensation coefficient based on transition state theory and molecular dynamics simulation, The Journal of Chemical Physics 118 (3) (2003) 1392–1399.

[33] T. Ishiyama, T. Yano, S. Fujikawa, Molecular dynamics study of kinetic boundary condition at an interface between argon vapor and its condensed phase, Physics of Fluids 16 (8) (2004) 2899–2906.

[34] T. Ishiyama, T. Yano, S. Fujikawa, Kinetic boundary condition at a vapor-liquid interface, Physical Review Letters 95 (8) (2005) 084504.

[35] T. Tsuruta, G. Nagayama, A microscopic formulation of condensation coefficient and interface transport phenomena, Energy 30 (6) (2005) 795–805.

[36] M. Bond, H. Struchtrup, Mean evaporation and condensation coefficients based on energy dependent condensation probability, Physical Review E 70 (6) (2004) 061605.

[37] A. Kryukov, V. Y. Levashov, About evaporation–condensation coefficients on the vapor–liquid interface of high thermal conductivity matters, International Journal of Heat and Mass Transfer 54 (13) (2011) 3042–3048.

[38] T. Ishiyama, S. Fujikawa, T. Kurz, W. Lauterborn, Nonequilibrium kinetic boundary condition at the vapor-liquid interface of argon, Physical Review E 88 (4) (2013) 042406.

[39] K. Kobayashi, K. Ohashi, M. Watanabe, Numerical analysis of vapor-liquid two-phase system based on the Enskog-Vlasov equation, in: AIP Conference Proceedings, Vol. 1501, AIP Publishing, 2012, pp. 1145–1151.

[40] T. Tsuruta, A. Tokunaga, G. Nagayama, D. A. Levin, I. J. Wysong, A. L. Garcia, Molecular boundary conditions and accommodation coefficient on a nonequilibrium liquid surface, in: AIP Conference Proceedings, Vol. 1333, 2011, p. 859.

[41] T. Yano, Molecular dynamics study of nonequilibrium processes of evaporation and condensation at a vapor–liquid interface, in: AIP Conference Proceedings, Vol. 1501, 2012, p. 926. doi:10.1063/1.4769641.

[42] T. Yano, Half-space problem for gas flows with evaporation or condensation on a planar interface with a general boundary condition, Fluid Dynamics Research 40 (7) (2008) 474–484.

[43] A. Frezzotti, L. Gibelli, S. Lorenzani, Mean field kinetic theory description of evaporation of a fluid into vacuum, Physics of Fluids 17 (1) (2005) 012102.

[44] T. Ishiyama, T. Yano, S. Fujikawa, Molecular dynamics study of kinetic boundary condition at an interface between a polyatomic vapor and its condensed phase, Physics of Fluids 16 (12) (2004) 4713–4726.

[45] A. Frezzotti, P. Grosfils, S. Toxvaerd, Evidence of an inverted temperature gradient during evaporation/condensation of a Lennard-Jones fluid, Physics of Fluids 15 (10) (2003) 2837–2842.

[46] R. Meland, Molecular dynamics simulation of the inverted temperature gradient phenomenon, Physics of Fluids 15 (10) (2003) 3244–3247.

[47] R. Meland, T. Ytrehus, Dependence of the inverted temperature gradient phenomenon on the condensation coefficient, Physics of Fluids 16 (3) (2004) 836–838.

[48] M. Kon, K. Kobayashi, M. Watanabe, Method of determining kinetic boundary conditions in net evaporation/condensation, Physics of Fluids 26 (7) (2014) 072003.

[49] M. Kon, K. Kobayashi, M. Watanabe, Numerical analysis of kinetic boundary conditions at net evaporation/condensation interfaces in various liquid temperatures based on mean-field kinetic theory, in: AIP Conference Proceedings, Vol. 1628, AIP Publishing, 2014, pp. 398–403.

[50] M. Kon, K. Kobayashi, K. Sasaki, M. Watanabe, Estimation of evaporation mass flux at vapor–liquid interface during nonequilibrium evaporation/condensation, Japanese Journal of Multiphase Flow (in Japanese) 29 (2015) 493–500.

[51] M. Kon, K. Kobayashi, M. Watanabe, Liquid temperature dependence of kinetic boundary condition at vapor–liquid interface, International Journal of Heat and Mass Transfer 99 (2016) 317–326.

[52] M. Kon, K. Kobayashi, M. Watanabe, Molecular simulation of evaporation mass flux during net evaporation/condensation, in: AIP Conference Proceedings, Vol. 1786, AIP Publishing, 2016, p. 110002.

[53] M. Kon, K. Kobayashi, M. Watanabe, Kinetic boundary condition in vapor-liquid two-phase system during unsteady net evaporation/condensation, European Journal of Mechanics B-Fluids (in press).

[54] L. Koffman, M. Plesset, L. Lees, Theory of evaporation and condensation, Physics of Fluids 27 (4) (1984) 876–880.

[55] C. Cercignani, W. Fiszdon, A. Frezzotti, The paradox of the inverted temperature profiles between an evaporating and a condensing surface, Physics of Fluids 28 (11) (1985) 3237–3240.

[56] L. Hermans, J. Beenakker, The temperature paradox in the kinetic theory of evaporation, Physics of Fluids 29 (12) (1986) 4231–4232.

[57] D. Bedeaux, L. Hermans, T. Ytrehus, Slow evaporation and condensation, Physica A 169 (2) (1990) 263–280.

[58] F. Sharipov, Onsager-casimir reciprocity relations for open gaseous systems at arbitrary rarefaction: I. general theory for single gas, Physica A 203 (3) (1994) 437–456.

[59] F. Sharipov, Onsager-casimir reciprocity relations for open gaseous systems at arbitrary rarefraction: Ii. application of the theory for single gas, Physica A 203 (3) (1994) 457–485.

[60] S. Kjelstrup, T. Tsuruta, D. Bedeaux, The inverted temperature profile across a vapor/liquid surface analyzed by molecular computer simulations, Journal of Colloid and Interface Science 256 (2) (2002) 451–461.

[61] C. T. Mills, L. F. Phillips, The gas–liquid interface and the paradox of inverted temperature profiles in the two-surface problem, Chemical Physics Letters 372 (5) (2003) 609–614.

[62] D. Enskog, Kinetic theory of heat conductivity, viscosity and diffusion in certain condensed gases and liquids, Kungl. Svenska Vetenskap. Handl 63 (1922) 1–44.

[63] P. M. Résibois, H-theorem for the (modified) nonlinear Enskog equation, Journal of Statistical Physics 19 (6) (1978) 593–609.

[64] L. d. Sobrino, On the kinetic theory of a Van der Waals gas, Canadian Journal of Physics 45 (2) (1967) 363–385.

[65] P. M. Résibois, M. De Leener, Classical kinetic theory of fluids, John Wiley & Sons, 1977.

[66] S. Chapman, T. G. Cowling, The mathematical theory of non-uniform gases: an account of the kinetic theory of viscosity, thermal conduction and diffusion in gases, Cambridge university press, 1970.

[67] J. M. Montanero, A. Santos, Monte Carlo simulation method for the Enskog equation, Physical Review E 54 (1) (1996) 438.

[68] M. Baus, Statistical mechanical theories of freezing: An overview, Journal of Statistical Physics 48 (5-6) (1987) 1129–1146.

[69] A. Frezzotti, A particle scheme for the numerical solution of the Enskog equation, Physics of Fluids 9 (5) (1997) 1329–1335.

[70] L. E. Reichl, I. Prigogine, A modern course in statistical physics, Vol. 71, University of Texas press Austin, 1980.

[71] J. Karkheck, G. Stell, Maximization of entropy, kinetic equations, and irreversible thermodynamics, Physical Review A 25 (6) (1982) 3302.

[72] J. Karkheck, G. Stell, Kinetic mean-field theories, The Journal of Chemical Physics 75 (3) (1981) 1475–1487.

[73] N. Van Kampen, Condensation of a classical gas with long-range attraction, Physical Review 135 (2A) (1964) A362.

[74] J. Dymond, B. Alder, Van der waals theory of transport in dense fluids, The Journal of Chemical Physics 45 (6) (1966) 2061–2068.

[75] N. F. Carnahan, K. E. Starling, Equation of state for nonattracting rigid spheres, The Journal of Chemical Physics 51 (2) (1969) 635–636.

[76] M. P. Allen, D. J. Tildesley, Computer simulation of liquids, Oxford university press, 1989.

[77] P. Barbante, A. Frezzotti, L. Gibelli, A kinetic theory description of liquid menisci at the microscale, Kinetic and Related Models 8 (2) (2015) 235–254.

[78] A. Frezzotti, M. Rossi, Slip effects at the vapor-liquid boundary, in: AIP Conference Proceedings, Vol. 1501, AIP Publishing, 2012, pp. 903–910.

[79] G. A. Bird, Molecular gas dynamics and the direct simulation of gas flows, Clarendon, 1994.

[80] K. Nanbu, Direct simulation scheme derived from the Boltzmann equation. I. Monocomponent gases, Journal of the Physical Society of Japan 49 (5) (1980) 2042–2049.

[81] K. Koura, Null-collision technique in the direct-simulation monte carlo method, Physics of Fluids (1958-1988) 29 (11) (1986) 3509–3511.

[82] G. E. Box, M. E. Muller, et al., A note on the generation of random normal deviates, The Annals of Mathematical Statistics 29 (2) (1958) 610–611.

[83] NIST Standard Reference Database Number 69, NIST Chemistry WebBook, June 2005 Release.
URL http://webbook.nist.gov/chemistry/

[84] G. Fang, C. Ward, Temperature measured close to the interface of an evaporating liquid, Physical Review E 59 (1) (1999) 417–428.

[85] R. Hołyst, M. Litniewski, Heat transfer at the nanoscale: evaporation of nanodroplets, Physical Review Letters 100 (5) (2008) 055701.

[86] Y. Onishi, On the negative mass flows in evaporation and condensation problems, Physics of Fluids 17 (12) (2005) 127106.

[87] H. Struchtrup, S. Kjelstrup, D. Bedeaux, Temperature-difference-driven mass transfer through the vapor from a cold to a warm liquid, Physical Review E 85 (6) (2012) 061201.

[88] H. Struchtrup, S. Kjelstrup, D. Bedeaux, Analysis of temperature difference driven heat and mass transfer in the Phillips–Onsager cell, International Journal of Heat and Mass Transfer 58 (1) (2013) 521–531.

[89] P. Andries, P. L. Tallec, J.-P. Perlat, B. Perthame, The Gaussian-BGK model of Boltzmann equation with small prandtl number, European Journal of Mechanics - B/Fluids 19 (6) (2000) 813–830.

[90] K. Kobayashi, S. Watanabe, D. Yamano, T. Yano, S. Fujikawa, Condensation coefficient of water in a weak condensation state, Fluid Dynamics Research 40 (7) (2008) 585–596.

[91] K. Kobayashi, K. Hori, H. Yaguchi, M. Watanabe, Molecular dynamics simulation on evaporation molecules in a vapor-liquid equilibrium state, in: AIP Conference Proceedings, Vol. 1628, AIP Publishing, 2014, pp. 404–410.

[92] C. Chu, Kinetic-theoretic description of shock wave formation. II., Physics of Fluids 8 (8) (1965) 1450–1455.

[93] H. S. Carslaw, J. C. Jaeger, Conduction of Heat in Solids, 2nd Edition, Oxford, 1959, pp. 92–104.